INVESTIGATION OF
TOURMALINE, APATITE AND MONAZITE

FROM A LOW-PRESSURE HIGH-TEMPERATURE REGIONAL AUREOLE

MOUNT STAFFORD, NORTHERN TERRITORY, AUSTRALIA

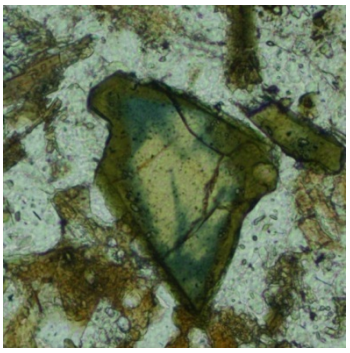

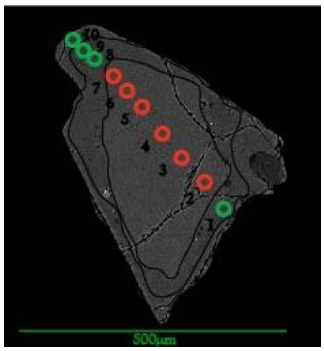

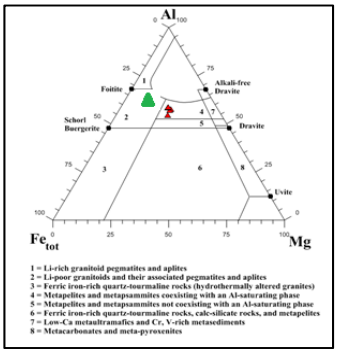

Kristina Gordon (41120620)

Presented to the Department of Earth and Planetary Sciences,
Division of Environmental and Life Sciences,
in Partial Fulfilment of the Requirements for the Degree of:

Honours, BSc
Macquarie University, Sydney
June 2013

MACQUARIE UNIVERSITY
SYDNEY ~ AUSTRALIA

GEMOC

STATEMENT OF ORIGINALITY

All the work submitted in this thesis is the original work of the author except where otherwise acknowledged. No part of this thesis has previously been submitted to any other university or institution.

…… ……..

Signed – Kristina Gordon ***Dated***

Student No: 41120620

ACKNOWLEDGEMENTS

First and foremost, thanks are given to my supervisor, Associate Professor Nathan Daczko, for all of his patience and support, and providing me with a unique opportunity to undertake further research as part of my Bachelor of Science.

I am very appreciative of the opportunity for research access to the equipment and facilities at the ARC National Key Centre for Geochemical Evolution and Metallogeny of Continents (GEMOC), based in the Department of Earth and Planetary Sciences at Macquarie University.

Special thanks are given to Associate Professor Norman Pearson and Dr Richard Flood, who were always kind enough to spare some time and provide advice. Thank you to Manal Bebbington, Steve Craven, Dr Kevin Grant, and Peter Wieland, and again to Norm Pearson, for help through every step of the preparation and analysis process - from letting me loose crushing rocks, showing me steps in making thin sections, getting hands-on pouring fused glass discs, pressing XRF pellets, and providing analytical and technical support whilst using the GEMOC lab equipment.

My participation in the 2011 Mount Stafford fieldwork was under the leadership of Professor Geoff Clarke and Associate Professor Nathan Daczko. Having the opportunity to investigate a fantastic metamorphic suite in a beautiful part of Australia, with Geoff and Nathan's keen enthusiasm and guidance, was a privilege in so many ways and an experience I'll never forget. The companionship of PhD candidates Eileen Dunkley (Macquarie University), Wei Wang (Sydney University) and Jess Matthews (Colorado School of Mines) along with helpful insights and discussions was greatly appreciated. Field photos from sample sites and of various stages of migmatite formation were collated, and it is with thanks to Geoff, Nathan, Eileen, Wei and Jess that these are hereby referenced.

Thank you to Eileen, and to former Honours student Kate Farrow, for kindly sharing resources and experiences regarding their own Mount Stafford research over many a coffee catch-up.

The support of my family has meant the world to me throughout this research project, and a big thank you goes to my parents, Ian and Anne Gordon, and my brothers Michael Gordon and Dr Robert Gordon. My work environment has been incredibly supportive of my part time research commitments both on professional and personal levels, for which I am very grateful. I am lucky enough to have a wonderful group of friends who have so often gracefully accepted my decline of social invitations with promises of "sometime soon". Thank you for being there for me.

ABSTRACT

The interbedded metapelites and metapsammites of the Mount Stafford Beds preserve a suite of metamorphic isograds and progressive evolution of migmatite morphology as a result of a steep lateral geothermal gradient of 75°C / km across a 10 km wide regional aureole. Migmatite banding at Mount Stafford is controlled by the interbedded turbidite protolith, with differentiation due to leucosome/melanosome segregation. The melting history at Mount Stafford has been found to be controlled by a series of biotite breakdown reactions, at different P/T conditions and contrasting whole rock. Melt mobilisation is limited across wide areas, which is confirmed by the constant bulk rock composition of metapelites and metapsammites across the area.

Textural observation from the in-situ relationships between apatite and micro-monazite ≈10um at low (greenschist) grades indicates the formation of metamorphic monazite at temperatures 25°C less than previously published for the Mount Stafford area, although this is in within temperature range of the observed new growth of monazite from a comparative the Cooma Complex. Within metapelites, monazite size and abundance increases with increasing metamorphic grade whilst an inverse decrease is observed with apatite mode and size. In metapsammites, apatite/monazite relationships are stable with monazite located as single grains in the matrix, and on rims of larger <250µm apatite and ilmenite grains, up to upper amphibolite grade. Xenotime is observed in samples from lower amphibolite to upper amphibolite, however mode decreases in the higher grades.

Tourmaline formation in the lower (greenschist) grades at Mount Stafford has been found to be a result of closed system behaviour of fluids due to the breakdown of B-host minerals (clay minerals, mica) and formation of metamorphic tourmaline rims on detrital cores. The formation of up to 3mm unzoned euhedral tourmaline grains in metapelite is considered to be related to the rapid consumption of muscovite. Mode and form of tourmaline reduces up-grade, as form changes to subhedral grains along mineral boundaries. At highest grade, tourmaline is absent from metapsammite, and evident as small grains within cordierite in metapelite which indicates B loss via fluid movement at higher metamorphic grades.

TABLE OF CONTENTS

LIST OF FIGURES

LIST OF TABLES

LIST OF ACRONYMS

Mpe	metapelite
Mps	metapsammite
SEM	scanning electron microscope
EMP	electron microprobe
EDS	energy dispersive system
BSE	backscattered electron
CL	cathodoluminescence

ABBEVIATIONS FOR NAMES OF ROCK FORMING MINERALS

From: Whitney and Evans (2010).

Andalusite	And	Biotite	Bt
Sillimanite	Sil	Muscovite	Ms
Aluminosilicate Al_2SiO_5	Als	Quartz	Qz
Monazite	Mnz	Tourmaline	Tur
Apatite	Ap	K-Feldspar	Kfs
Zircon	Zr	Microcline	Mc
Xenotime	Xtm	Plagioclase	Pl
Garnet	Grt	Orthopyroxene	Opx
Ilmenite	Ilm	Clinopyroxene	Cpx
Cordierite	Crd	Pinite	(not listed) “Pin”
Spinel	Spl	Hercynite	Hc
Epidote	Ep	Allanite	Aln
Chlorite	Chl	Fibrolite	Fi
Sericite	Ser		

LIST OF APPENDICIES

1. Introduction

Mount Stafford is located ≈170km north-west of Alice Springs, within the Anmatjira / Reynolds Ranges in the Aileron Province, Central Australia (Fig: 1.1). The geological package at Mount Stafford is primarily aluminous metapelite with regularly alternating beds of metapsammite and cordierite granofels on a centimetre to metre scale (Greenfield *et al.*, 1996; White *et al.*, 2003).

During 1810-1800 Ma the northern Arunta Region and Mount Stafford were exposed to a geotherm perturbation under low pressures (2.5 – 4 kbar) across a small area (260 km^2). At Mount Stafford, the interbedded metapelites and metapsammites preserve a suite of metamorphic isograds (from greenschist to granulite). A low-pressure high-temperature (LPHT) regional metamorphic aureole displays progressive evolution of migmatite morphology as a result of a steep lateral geothermal gradient of 75°C / km across 10 km wide region, forming (Vernon *et al.*, 1990).

Migmatites are high-grade metamorphic rocks which have developed a heterogeneous appearance due to alternating lenses or layers through the development of petrographically distinct domains due to processes of partial melting and differentiation of a melt fraction (Brown, 1973; Sawyer, 2008). The migmatite banding at Mount Stafford is controlled by the interbedded turbidite protolith, rather than differentiation due to leucosome/melanosome segregation (Rubatto *et al.*, 2006) (& this study). Heterogeneity of the layered beds on the decimetre scale results in the presence or absence of key metamorphic indicator minerals at the same grade (White *et al.*, 2003)(& this study).

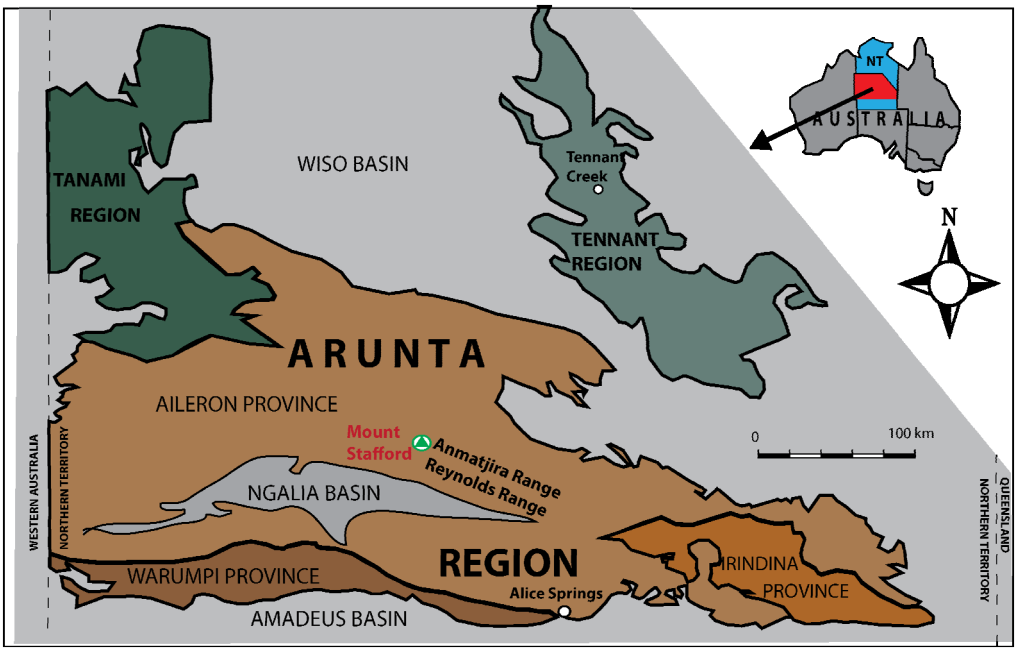

Figure 1.1: Schematic map of the Arunta, Tennant and Tanami Regions in central Australia showing the Reynolds and Anmatjira Ranges in the Aileron Province, Northern Arunta Region
Modified after: (Claoué-Long *et al.*, 2008a)

1.1 Study Site

This study covered a field area at Mount Stafford of approximately 120km^2, from the Lander River in the south-west (Lander Camp) to the granulite grade rocks close to the Eastern Granite. A schematic of the field site is provided in Figure 1.2, along with the location of sample points used in this study.

Fieldwork in 2011 resulted in 24 sample sites and 300kg of samples being collected, which when combined with the 21 sample sites and 250kg of samples collected in 2010, results in a comprehensive archive collection for the Mount Stafford area (Farrow, 2012). Further detail of regional geology is outlined in Chapter 2, and fieldwork methodology outlined in Chapter 3.

1.2 Research Objectives

This Honours research has two main objectives, both focusing on geochemical and petrologic changes in minerals due to bulk rock composition, increase in temperature, and influence of partial melt. Four sites were identified from the Spring Creek transect that were representative of greenschist to upper amphibolite grade. From each of these sites, a pair of samples were chosen for analysis that displayed contrasting bulk rock chemistry (ie: metapelite, sub-aluminous metapelite, metapsammite).

Aims of this study are to:

- Develop a field sampling strategy that, when combined with 2010 samples, would define complete metamorphic transects from lowest to highest grade metamorphism.
- Determine appropriate samples for this study, based on petrographic analysis of thin sections, and bulk rock chemistry.
- Investigate the textural and modal relationship between the accessory phosphates monazite and apatite with increasing metamorphic grade.
- Develop criteria for the assessment of tourmaline geochemistry.
- Categorise changes in the geochemistry of tourmaline between zones of increasing metamorphic grade.

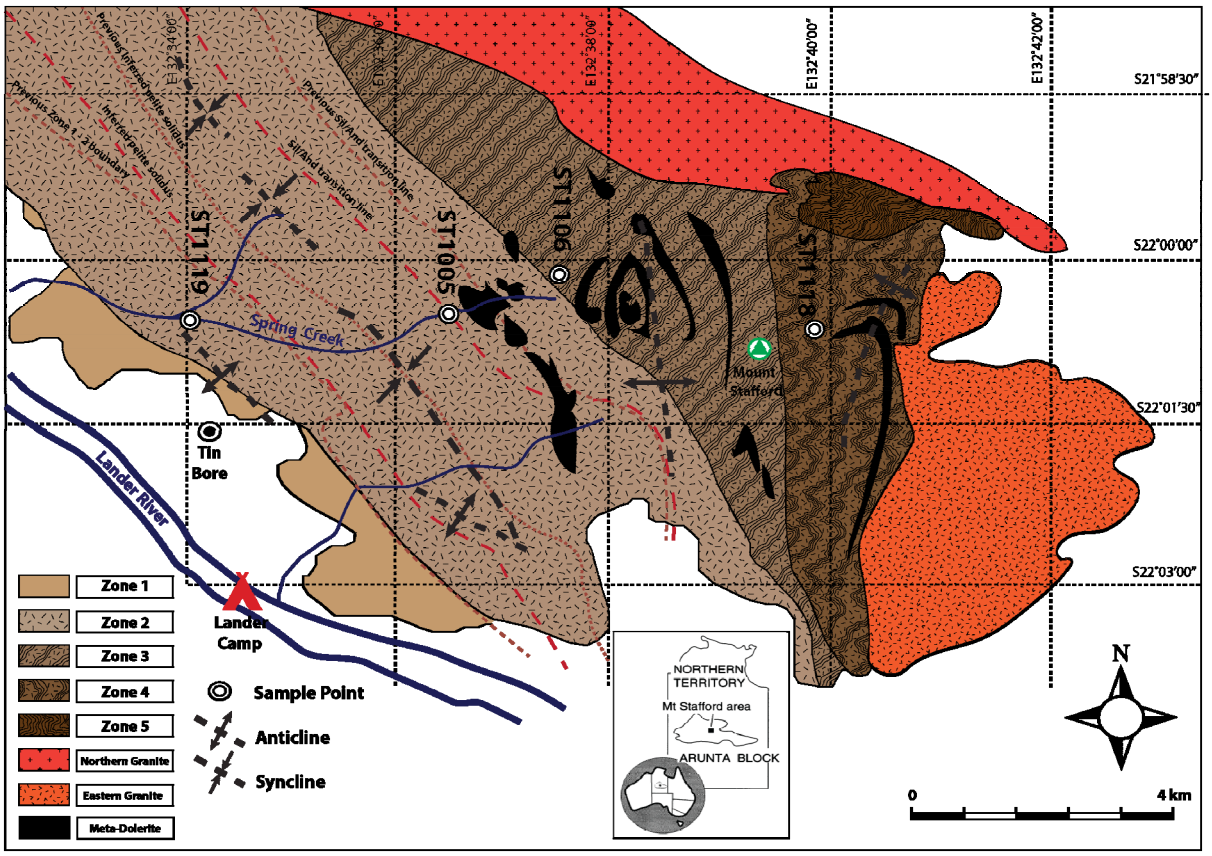

Figure 1.2: Schematic Map of Mount Stafford, Central Australia
Modified after: (Greenfield *et al.*, 1996; Stewart and Chan, 1982; Wang *et al.*, *pending submission*)

1.3 Overview: Tourmaline

Studies on tourmaline from igneous, hydrothermal, and metamorphic systems have shown it to be a valuable petrographic indicator mineral. Tourmaline is ubiquitous in a range of environments and is extremely chemically and mechanically stable once formed. Its sensitivity to system changes during formation results in the storage of a diverse range of chemical, textural and isotopic information during growth (Henry and Dutrow, 1996).

Tourmaline is only exceeded by zircon for its chemical and mechanical stability in sedimentary environments. Provenance has been investigated on the basis of different colours and rounding of tourmaline grains, and the presence of tourmaline has been used as a maturation index for clastic sediments (Henry and Dutrow, 1996).

Tourmaline development depends fundamentally on the availability of boron, which is incorporated in tourmaline at ≈10 wt% oxide (Deer *et al.*, 1992). During closed system behaviour of B during metamorphism, B is derived from minerals found locally within the rock system (Henry and Dutrow, 1996). For B to be retained in the rock, there must be a B-host (ie: muscovite, clay minerals) or a B stable mineral (ie: tourmaline), else B loss can occur. B released from the breakdown of B-host minerals can therefore become available for the formation of tourmaline Provided there are the appropriate mineral assemblages and fluid compositions, tourmaline formation can occur under diagenetic conditions >150°C (Henry and Dutrow, 1996).

1.4 Overview: Accessory Phosphates

Accessory mineral phases can be important indicators of the development of mineral assemblages in metamorphic environments (Wark and Miller, 1993). Accessory phases can host the majority of trace and radioactive elements used in isotopic and geochronological investigations, and due to some accessory mineral's mechanical and geochemical stability can be used as indicators of source materials and evolution of melt composition (Wark and Miller, 1993). The majority of a trace element budget (REE, P, Y, Zr, Hf) can be held in a rock's accessory minerals so the growth or consumption of accessory minerals present can be a primary control the distribution of trace elements throughout a rock (Pyle and Spear, 2003).

This investigation focuses on the behaviour of accessory phosphates, to determine whether phosphate accessory phases with comparative bulk rock chemistry (aluminous pelite / psammite) react in a predictable manner with increasing metamorphic grade. Common phosphate accessory minerals in the Mount Stafford metapelites and metapsammites are monazite, apatite and xenotime (Rubatto *et al.*, 2006) (& this study).

Apatite is a common accessory mineral in metamorphic rocks, and can be found in rocks with a diverse range of bulk compositions, and at various metamorphic grades from low-temperature alteration, migmatites, through to ultra high-pressure environments. The occurrence of apatite is dictated by the availability of key constituents, namely P, Ca and F which are found in greater than trace levels in most rocks, and it's stability is not considered to be controlled by other locally occurring phosphates (Spear and Pyle, 2002).

Both xenotime and monazite are accessory minerals in a wide range of rocks including granites, pegmatites, gneisses, carbonates, migmatites and quartz veins, along with having the mechanical and

chemical stability to survive weathering processes to be included in alluvial deposits (Hughes and Rakovan, 2002). They are abundant in metapelitic rocks but are less commonly found in rocks with more calcic and mafic bulk compositions (Spear and Pyle, 2002). Monazite has been reported in metamorphic systems from low pressure contact aureoles through to granulite facies and ultra high-pressure pelitic rocks. Monazite incorporates uranium and thorium, to the point where it is used as an ore for thorium and a secondary source of uranium (Spear and Pyle, 2002).

Xenotime has been found in rocks from the chlorite zone through to corderite+K-feldspar zones. In garnet zones, xenotime can be found in the rock matrix however if garnet is present, it may be consumed as garnet grows and incorporates Y and HREE. If garnet is absent, xenotime can be present in all metamorphic grades (Spear and Pyle, 2002).

2 Regional Geology

2.1 Introduction

This section provides a local geological context for Mount Stafford in the Northern Territory, Central Australia, outlining the regional geologic setting, and correlation between local and regional lithologic packages. Previous studies on the Proterozoic rocks of the Arunta Region and surrounds have been undertaken by numerous workers, including detailed analysis of the metamorphic low-pressure high-temperature (LPHT) regional aureole at Mount Stafford. A summary of their findings and constraints are provided in this chapter.

White *et al* (2003) have categorised the major sequence of metamorphic conditions and reactions due to the varying bulk rock composition at Mount Stafford into metamorphic zones, and a summary of these findings are provided in this chapter as a petrographic overview. Detailed petrographic investigation of minerals and textures for this study's sample sites are provided in Chapter 5. Field photographs are credited to the 2010 and 2011 fieldwork teams from Sydney University, Macquarie University and the Colorado School of Mines. Please refer to Acknowledgements, page (iii), and Appendix 1 for photo scales.

2.2 Arunta Region, Northern Territory

The Proterozoic Arunta Region is a 200,000km^2 inlier located in the Northern Territory, Central Australia. The Region is geologically complex, and records overprinting of several geological events from pre-1800 Ma through to the Palaeozoic (Claoué-Long and Hoatson, 2005). On the basis of variations in lithology, facies assemblages and isotopic age data, the Arunta Region has been further categorised into three major tectonic provinces, the Aileron Province to the north, Irindina Province to the east and Warumpi Province to the south (Fig: 1-1) (Claoué-Long *et al.*, 2008a).

The majority of Aileron Province comprises two metasedimentary sequences, the ≈1880 Ma Lander Package, and the ≈1800 Ma Reynolds Range Group (Buick *et al.*, 1999; Claoué-Long *et al.*, 2008a; Collins and Shaw, 1995).

2.3 The Lander Package

The Lander Package is recognised as the earliest geologic sequence in the Northern Arunta Region. The Package consists of widespread dominantly turbidic sediments with a detrital zircon population of 1880-1840 Ma and a minor presence of older Proterozoic and Archaean components (Claoué-Long *et al.*, 2008a; Claoué-Long *et al.*, 2008b). Interlayed within the Lander Package are basalt and dolerite lavas/sills, and granitic plutons of the 1810-1800 Ma Mount Stafford Event and 1795-1770 Ma Yamba event (Claoué-Long *et al.*, 2008a).

Regional geochronological studies on sedimentary zircons have correlated the deposition of the Lander Package with the Tennant Region Ooradidgee Group, and the Tanami Group of the Tanami Region, each containing zircon populations dating ≈1880–1830 Ma and an older population of zircons up to 2900 Ma. (Claoué-Long *et al.*, 2008a). The Ooradidgee Group overlies the earlier, deep water Warramunga Group, which has been dated at ≈1850 Ma (granites), and ≈1860 Ma (volcanic units).

No equivalent older basement has been identified for the Lander Package. (Claoué-Long *et al.*, 2008a; Claoué-Long *et al.*, 2008b).

2.4 Mount Stafford Beds

Mount Stafford is located ≈170km north-west of Alice Springs, within the Anmatjira / Reynolds Ranges in the Aileron Province (Fig: 1-2). The geologic package at Mount Stafford, referred to as the Mount Stafford Beds, has been identified as a separate facies transition of the Lander Formation (Buick *et al.*, 1999; Claoué-Long *et al.*, 2008a; Rubatto *et al.*, 2006). The Mount Stafford Beds are primarily aluminous metapelite with regularly alternating beds of metapsammite and cordierite granofels on a centimetre to metre scale. The sequences have preserved sedimentary structures such as cross bedding and ripples, and relict Bouma sequences (Greenfield *et al.*, 1996; White *et al.*, 2003). Zircon U/Pb dating of sandstones from the Mount Stafford Beds shown a depositional age range of 1866 ±3 Ma (Claoué-Long *et al.*, 2008a).

2.5 Mount Stafford Tectonic History

During 1810-1800 Ma the northern Arunta Region and Mount Stafford were exposed to a geotherm perturbation under low pressures (2.5 – 4 kbar) across a small area (260 km^2). Although the area was subject to three phases of syn-metamorphic folding, foliations at low metamorphic grades are generally weak and sedimentary features are still identifiable (Collins *et al.*, 1991)(& this study).

During D_1, F_{1a} close to tight metre scale asymmetric folds developed, with an S_{1a} foliation displayed only in high grade rocks. The asymmetry of the folds indicate westerly transport. F_{1b} is subhorizontal west-verging folding inferred to be due to high grade metamorphism, and is evident in the higher grade rocks of the north-east (Collins *et al.*, 1991).

F_{1c} is the primary folding event which is evident in the overall outcrop pattern of the area. The F_{1c} north-west axial trace with shallowly-plunging open folds in the lower grade south-west area changes to isoclinal north-trending folds which plunge 40-60°NE in the higher-grade north-east area (Fig: 2-2). S_{1c} is evident as a slaty cleavage in low grade greenschist, and as schistosity in higher grades rocks, although it is not developed in the granulite facies (Collins *et al.*, 1991).

The reorientation of F_{1c} folds in the eastern edges of the Mount Stafford Domain due to Westward thrusting of the neighbouring Weldon terrain during a D_2 event, resulting in some overturning of F_{1c} folds due to eastward tilting and tightening. This overprinting is inferred to be further identified through sillimanite assemblages imprinted over andalusite porphyrobasts indicate an increase in pressure during D_2 thrusting (Collins *et al.*, 1991).

The age of the D_1 cycle is constrained by the megacrystic granitoids, dated post S_{1b} and pre-S_{1c} at 1802 ±3 Ma for the Eastern Granite (Collins *et al.*, 1991; Rubatto *et al.*, 2006). Intrusive dolerite sills throughout the area are ascribed to have been emplaced synchronous with the start of D_1 and affected by the three phases of the deformation cycle (Collins and Vernon, 1991; Rubatto *et al.*, 2006). Evidence of D_{1a} shear bands preserved in schollen in an intermingling zone between the northern granite and bedded migmatites indicate that (Zone 5 hybrid diatexite) mixing occurred post-D_{1b} (Greenfield *et al.*, 1996). The source of the high geotherm at Mount Stafford has yet to be fully explained. As deformation across the northern Arunta Region during metamorphism was

compressional towards the areas of lower metamorphic grade, an extensional model for LPHT regional aureole is not applicable (Collins *et al.*, 1991).

2.5.1 Northern and Eastern Granites

One model supporting the LPHT metamorphism in such a localised area is the possibility of repeated intrusion of granite sills, as these intrusions induce metamorphism and melting reactions that produce fluids, thereby accelerating fluid pressure and enhancing melt deformation (Collins and Vernon, 1991; White *et al.*, 2003). Relationships between the granite intrusions at Mount Stafford and the high-grade metamorphism are complex, with the granites cutting mapped isograds, and evidence of intermingling of granitic material and migmatites (Farrow, 2012; Rubatto *et al.*, 2006). Geochronological studies on zircon and monazite from the northern and eastern granite and metamorphic zones at Mount Stafford have shown that the emplacement of the granites was coeval with metamorphism, which means that the granites are unlikely candidates as a heat source for peak metamorphism (Rubatto *et al.*, 2006).

A study undertaken by Farrow (2012) assessing the emplacement of the northern and eastern granites showed that the timing of metamorphism and the emplacement of granites were almost identical. Farrow (2012) calculated emplacement ages for the granites based on geochronological assessment of magmatic rim overgrowth on zircons. The eastern granite was dated at 1786 ±15Ma which was just outside reported zircon ages by Rubatto *et al* (2006) of 1805 ±3 Ma, and 1802 ±3 Ma from monazite dates. Zircon rim dates for the Northern Granite were 1842 ±26, which were considered not to be a magmatic age but part of an older inherited population (Farrow, 2012). This appears to be the only published date on the northern granite.

2.6 Mount Stafford Migmatite Petrography

Migmatites are defined as composite rocks which have alternating macroscopic lenses or layers due to the development of petrographically distinct domains through processes of partial melting and differentiation of a melt fraction (Brown, 1973; Sawyer, 2008). Segregation of the melt fraction results in the formation of a pale-coloured quartzofeldspathic leucosome and darker ferromagnesian melanosome bands, sometimes containing rafts of paleosome (parent rock). Melt proportion is variable and dependent on factors such as protolith and metamorphic conditions (Brown, 1973; Sawyer, 2008).

The LPHT conditions at Mount Stafford have been the basis for a study of migmatite formation as a function of temperature, without the complications which can occur due to deformation associated with intense pressure (Greenfield *et al.*, 1998). The interbedded metapelites and metapsammites of the Mount Stafford Beds preserve a suite of metamorphic isograds and progressive evolution of migmatite morphology as a result of a steep lateral geothermal gradient of 75°C / km across a 10 km wide regional aureole (Vernon *et al.*, 1990). P-T conditions have been constrained to temperatures ranging from ≈500°C at ≈2.7 kbar pressure for low-grade metamorphism to ≈810°C and 4 kbar pressure at high grades (Greenfield *et al.*, 1996; White *et al.*, 2003).

The migmatite banding at Mount Stafford is controlled by the interbedded turbidite protolith, rather than differentiation due to leucosome/melanosome segregation (Rubatto *et al.*, 2006) (& this study). Heterogeneity of the layered beds on the decimetre scale results in the presence or absence of key metamorphic indicator minerals at the same grade (White *et al.*, 2003)(& this study). The bulk composition of the metapelites and metapsammites has been found to be relatively constant across metamorphic isograds, which is an indication that melt mobilisation has been limited (Greenfield *et al.*, 1996)(& this study).

2.6.1 Classification of Mount Stafford Metamorphic Zones

A summary of documented metamorphic reactions and conditions given by Greenfield *et al* (1996) and White *et al* (2003) are listed below, and are referenced throughout this study.

2.6.1.1 Zone 1 - Muscovite-Chlorite-Quartz-Biotite Schist

Rocks in Zone 1 are poorly preserved outcrops of interbedded metapsammites and metapelites, which preserve ripples and relic upwards-younging Bouma sequences (Fig: 2.1) (Greenfield *et al.*, 1996)(& this study). The metapelites contain dominant muscovite, biotite and quartz, with minor ilmenite, tourmaline and chlorite. The metapsammite layers contain coarse-grained quartz and sericitized feldspar, with minor biotite, muscovite, tourmaline, ilmenite and apatite (Greenfield *et al.*, 1996; White *et al.*, 2003).

2.6.1.2 Subzone 2a – Andalusite-Cordierite-K-Feldspar-Biotite-Quartz granofels

Subzone 2a is marked by the appearance of <1 cm cordierite porphyroblasts which can be completely pseudomorphed by andalusite-biotite-quartz symplectites. Cordierite and K-feldspar poikiloblasts are found with inclusions of fine grained biotite and rounded quartz, within a <1.5cm granoblastic mosaic of quartz, K-feldspar, biotite and ilmenite. Andalusite can occur either as fine to medium grained idioblastic prisms that are either inclusion-free, or polikoblastic with quartz inclusions. Rarely, small (cm-scale) leucocratic segregations in extensional structures are found, containing quartz with minor biotite and K-feldspar, indicating incipient stages of melt production (Fig: 2.2) (Greenfield *et al.*, 1996).

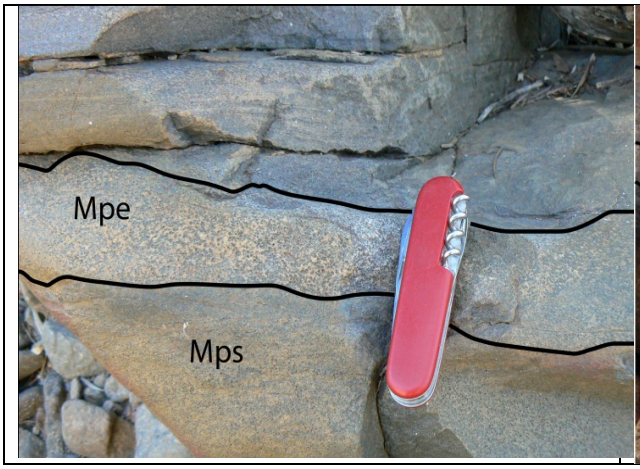

Figure 2.1: Zone 1 - Interbedded metapelite and metapsammite

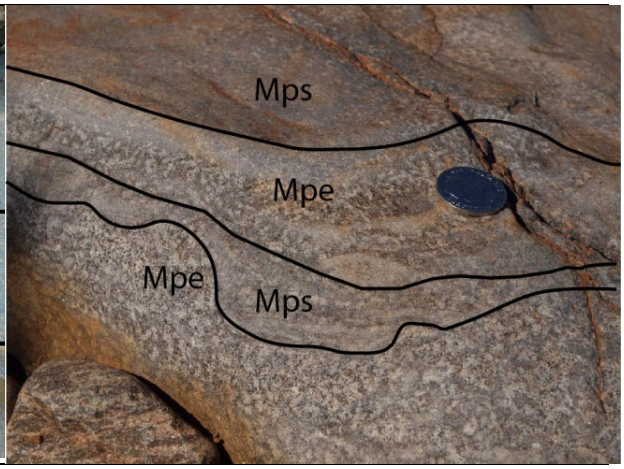

Figure 2.2: Subzone 2a - Displaying coarser grained metapelite and metapsammite

2.6.1.3 Subzone 2b – Andalusite-Cordierite-K-feldspar-Biotite-Quartz migmatite

The appearance of in-situ metatexite in metapelites mark the change from subsolidus to supersolidus between zones 2a and 2b (Greenfield *et al.*, 1996). The metatexite contains large 0.5-2 mm idioblastic andalusite, K-feldspar, cordierite and biotite with optically continuous quartz (up to 2 cm) between grains. The metapsammite in this zone remains fine grained in comparison to the metapelite, with a comparable mineral assemblage to the metapsammite at lower grades (Fig 2.3) (Greenfield *et al.*, 1996).

2.6.1.4 Subzone 2c – Andalusite-Sillimanite-Spinel-Cordierite-K-feldspar-Biotite-Quartz ±Garnet migmatite

Subzone 2c can be distinguished from 2b by the increase in grain size in the metapelites, and the appearance of sillimanite and spinel with a reduction in the abundance of quartz and biotite. Metapelite layers may contain up to 20% volume of leucosome, forming vein networks, and filling boudin necks (Fig: 2.4) (Greenfield *et al.*, 1996).

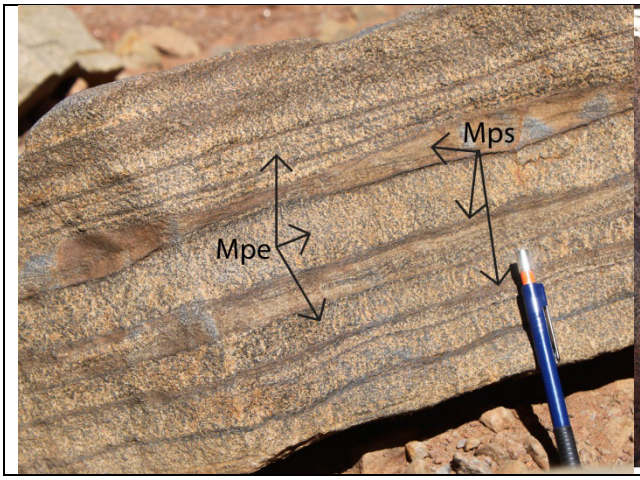

Figure 2.3: Subzone 2b - Stromatic (bedded) metatexite migmatite

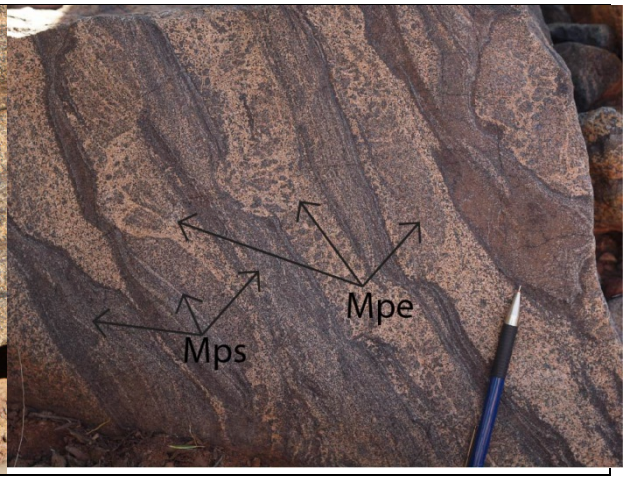

Figure 2.4: Subzone 2c - Stromatic metatexite migmatite transitional to schollen structure (diatexite)

2.6.1.5 Zone 3 – Sillimanite-Spinel-Cordierite-K-feldspar ±Biotite ±Quartz ±Garnet migmatite

The sharp increase in topography (of approx. 400m) in the Mount Stafford region has been noted and associated with an overall decrease in biotite content (Greenfield *et al.*, 1996)(& this study). Schlieren migmatites are observed in Zone 3, which may be in contact with layered migmatites. Schlieren migmatites retain a similar petrology to layered migmatites. However, the metapelite/metapsammite bands have been mobilized due to a reduction in layer competency through increased melt fraction (Figs: 2.5, 2.6, 2.7). Leucosomes in metapelites become more extensively connected, with suspended rafts of metapsammite. Metapelites contain granoblastic K-feldspar, sillimanite, cordierite, biotite and quartz, with minor spinel, plagioclase and ilmenite and rare garnet (Greenfield *et al.*, 1996).

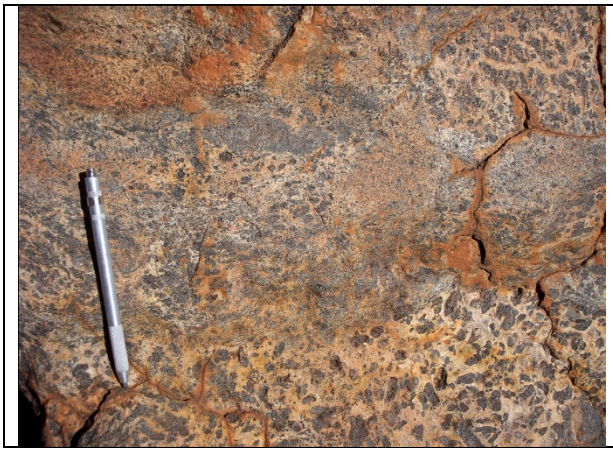

Figure 2.5: Zone 3 - Nebulitic diatexite

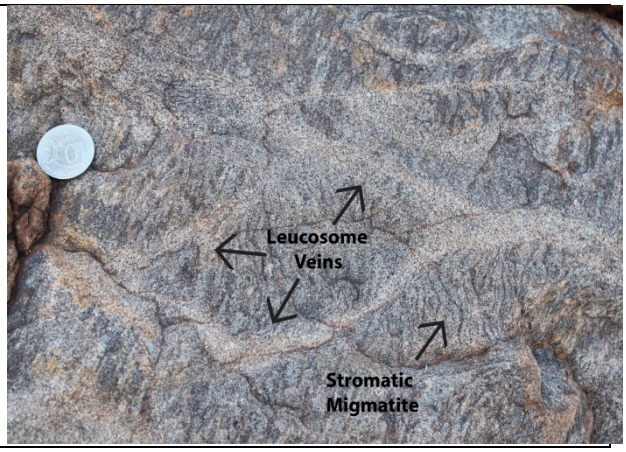

Figure 2.6: Zone 3 - Net structure of leucosomes cross-cutting stromatic migmatite

2.6.1.6 Zone 4 – Garnet-Orthopyroxene-Cordierite-K-feldspar bedded and schlieren migmatite

Garnet-orthopyroxene-cordierite assemblages are found at the lower limits of Zone 4, along with the appearance of diatexite migmatites. Co-existing idioblastic garnet and orthopyroxene is observed in metapsammite. Garnet is most commonly found as strings of coarse poikiloblastic grains in melanosome which are truncated on contact with mesosome (Fig: 2.9)(& this study). Sillimanite is replaced by symplectites of spinel and cordierite, and spinel is also observed as isolated grains, inferred to have grown with quartz (Greenfield *et al.*, 1996) (& this study).

2.6.1.7 Zone 5 – Cordierite-K-feldspar-Biotite-Quartz ±Garnet ±Orthopyroxene hybrid diatexite

The hybrid diatexite in Zone 5 has a higher percentage biotite, plagioclase, and quartz than is found in Zone 4 (Fig: 2.10) (Greenfield *et al.*, 1996). The metapelite/metapsammite bedding structure evident in Zones 1-4 have been completely disrupted, with remnant layers found as 10-20cm rotated schollen (rafts) within the more homogenous diatexite matrix. Steeply dipping lenses of K-feldspar with large 6-8 cm megacrysts occur in steeply dipping layers, with an increase in abundance through the gradational contact between Zone 5 and the northern granite. The layering becomes increasingly disrupted, with an increase in the abundance of megacrysts, closer to the northern granite. (Greenfield *et al.*, 1996). Field relationships, mineral mode, and geochemical investigation identified Zone 5 hybrid diatexite as an area of intermingled injections of northern granite into the bedded migmatites (Farrow, 2012; Greenfield *et al.*, 1996).

Figure 2.7: Zone 3 - Diatexite with dark selvedge between the melanosome and leucosome

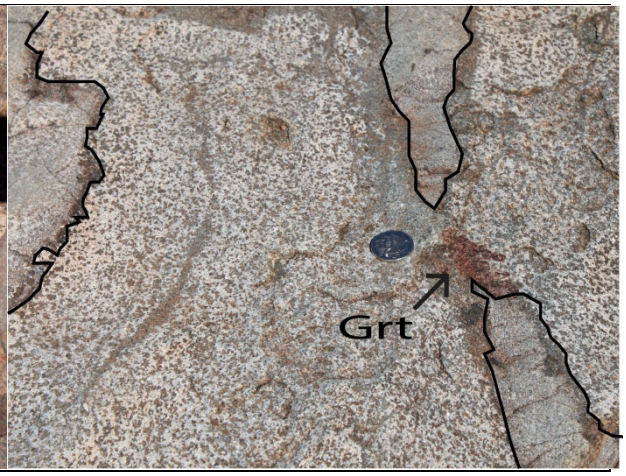

Figure 2.8: Zone 4 - Leucosome garnet forming in dilation structure (boudin neck)

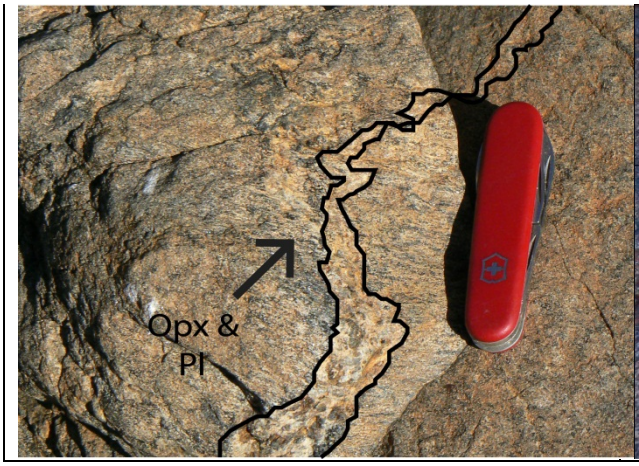

Figure 2.9: Zone 4 - Mafic granulite with orthopyroxene cutting across thin elongated orthopyroxene in foliations

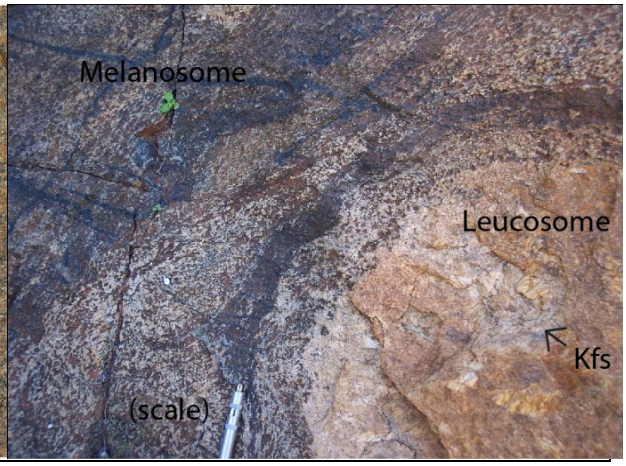

Figure 2.10: Zone 5 - Folded leucosome and melanosome with large K-feldspar at fold hinge

3 Field Work

The fieldwork for this study was undertaken in June 2011. Mount Stafford is located ≈170km north-west of Alice Springs, within the Anmatjira / Reynolds Ranges in the Aileron Province. The field site is located on Coniston Station, and covered a field area at Mount Stafford of approximately 120km^2, from the Lander River in the south-west (Lander Camp) to the granulite grade rocks close to the Eastern Granite. A schematic of the field site is provided in Figure 1.2, along with the location of sample points used in this study.

The sampling strategy for 2011 field work was to provide a complete suite of rocks for transects along Spring Creek, and IGCS Creek. This was completed, and resulted in 24 sample sites and 300kg of samples being collected in 2011. When combined with the 21 sample sites and 250kg of samples collected in 2010, results in a comprehensive archive collection for the Mount Stafford area (Farrow, 2012). A Google map image of the study site, including indication of 2010 and 2011 field sampling, is included in Appendix 2. A summary of transect sample numbers, and granite samples, is provided in Appendix 3.

4 Sample processing and analytical methods

4.1 Introduction

This chapter provides an overview of sample handling and processing for analysis, along with description of laboratory conditions for the analytical techniques used.

Samples were prepared at the ARC National Key Centre for Geochemical Evolution and Metallogeny of Continents (GEMOC), based in the Department of Earth and Planetary Sciences, Macquarie University, North Ryde. X-Ray Fluorescence (XRF) whole rock major element chemistry was prepared and analysed at the University of Beijing, Beijing, People's Republic of China. Field sample and analysis log details are provided in Appendix 4.

4.2 Petrography Sample Preparation

Rock samples from 2011 fieldwork were cut down exposing fresh (unweathered) rock pieces, from which thin section blocks approximately 30x15x10mm were cut. Care was taken to identify areas of petrographic interest, such as selvedges, or any macro mineral developmental relationships. Blocks were impregnated with an epoxy resin under vacuum conditions dried on a heating tray. One side of the block was then ground down on a flat polishing wheel, ready to be mounted on a glass thin section. Once mounted, the blocks were again cut thinly, and further polished to a thickness of ≈30µm. Polished thin sections for samples collected in 2010 were available for analysis.

Petrographic analysis was undertaken under transmitted light conditions using binocular and monocular petrographic microscopes. Initially, the suite of thin sections were analysed for textures, mineral relationships, mode, and the presence or absence of the key minerals for this study (tourmaline, monazite, apatite). Sample sites were chosen for this study based on the preliminary petrographic assessment. These sites were ST1119, ST1005, ST1106 and ST1118 from the Spring Creek Transect, covering an increase in metamorphic grade from greenschist to upper amphibolite. A pair of contrasting protolith types (metapsammite, subaluminous metapelite, aluminous metapelite) were selected for each of the sample site, resulting in eight thin sections total for this study.

Detailed petrographic analysis in Chapter 6 outlines major, minor and accessory mineral assemblages, mineral modal abundance, grain size, textural appearance, grain boundary relationships and structures. The modes of minerals were estimated using ImageJ analysis of SEM back-scattered electron images; ImageJ is a public domain Java image processing program (Rasband, 2012). Grain size is measured from visual assessment of thin sections under a petrographic microscope. Mineral abbreviations follow (Whitney and Evans, 2010).

4.3 X-Ray Fluorescence (XRF) Sample Preparation

Using a hydraulic splitter (Enerpac hydraulic press), rocks from the 2011 fieldwork were split into large chunks, then further pressed until they were broken down into sand-sized particles (2mm). Samples were then reduced to a fine powder by grinding in a TEMA tungsten-carbide mill.

29 samples of milled rock powder were pressed into aluminium base pellets for XRF trace element chemical analysis. 5.5 grams of powder were mixed with 12 drops of an ethanol/PVC mixture, scooped into an aluminium base, then compressed to 5 tonnes to form a compact pellet.

Fused glass discs for XRF major and minor element chemical analysis were prepared at Macquarie University for analysis at Wollongong University. Platinum crucibles were placed on Mettler AE160 scales and zeroed. Sample milled rock powder was placed in the platinum crucible using a metal spatula, wiped down with kim wipes and ethanol, to 300mg and the weight recorded to four decimal places. Any rock powder in excess of this value was discarded, not returned to the sample container. Five crucibles were measured in each sample run. After sample powder had been measured, the scales were again zeroed and 2.5g 100% Lithium Metaborate Flux ($LiBO_2$) added. This was mixed using a metal spatula, wiped down with kim wipes and ethanol before mixing.

Platinum crucibles were placed in a furnace with agitation control, and gradually heated to 1000°C. After 20 minutes at peak temperature, one ammonium iodide tablet is added and agitated for a further five minutes, before the melted rock glass is poured and pressed on a heated hotplate. The glasses are then carefully placed to cool, and then stored in an airtight container.

Loss on Ignition (LOI) utilises ceramic crucibles, which are heated to 1100°C, cooled and placed in an airtight container to avoid sample contamination. Using tongs, a crucible is placed on scales and weight recorded, before being zeroed and 1.2g of sample rock powder added and weight recorded to four decimal places. Crucibles are then heated to 1100°C in a furnace overnight, cooled, and the second weight recorded. LOI can then be calculated from the difference in the weights.

4.4 X-Ray Fluorescence (XRF) Whole Rock Chemical Analysis

Major (>1.0 wt%) and minor (0.1 to 1.0 wt%) element data are reported as weight percent oxide, with trace elements (< 0.1 wt%) reported in parts per million (ppm) (Winter, 2010).

4.4.1 XRF Major and Minor Chemical Analysis

XRF major and minor chemical analysis were performed on the 2011 sample fused glass discs prepared at Macquarie University, by the University of Wollongong on 12/4/2012. Details on the lab equipment or standards used are not available. Analysis results are table in Appendix 9.
XRF major and minor chemical analysis on the 2011 field samples was jointly undertaken by the University of Beijing, China on 4/11/2011. The University of Beijing prepared fused glass discs using the milled rock powder processed at Macquarie University, following the process outlined in (Li *et al.*, 2006). Lower limits of detection are tabled in Appendix 7, and reference standards are tabled in Appendix 8.

4.4.2 XRF Trace Element Chemical Analysis

Pressed rock powder pellets were analysed at Macquarie University for trace chemical elements on a Spectro X-LAB 2000 on 26/9/2011 and are tabled in Appendix 11. The lower limits of detection are tabled in Appendix 7, along with reference standards in Appendix 10. The standards published by USGS (USGS, 2013a, b) don't record a full suite of trace element analysis. Available analyses are recorded, and compared to the standards run as 'unknowns'. A number of standard results are below the lower limit of detection (LLD).

4.5 Backscattered Electron Imaging and Energy Dispersive X-ray Spectroscopy

Scanning Electron Microprobe backscattered electron (SEM-BSE) images show chemical variations in minerals. Grains (and zones within grains) which consist of heavier elements appear lighter in colour, as they more strongly reflect (backscatter) electrons (Winter, 2010). SEM-BSE images were taken of monazite, apatite, xenotime and tourmaline grains from this study's four metapelite / metapsammite pairs of thin sections, that had previously been prepared for petrographic analysis. Thin sections were cleaned using lint-free kimwipes and ethanol solution prior to carbon coating. Tourmaline and monazite grains of interest were circled using a smudge-proof felt-tipped pen, developing a map to allow ease of location under SEM conditions (Appendix 6).

SEM analysis was undertaken at the ARC National Key Centre for Geochemical Evolution and Metallogeny of Continents (GEMOC), based in the Department of Earth and Planetary Sciences at Macquarie University, North Ryde. Analysis in March and April 2012 were on a Bruker 133eV Xflash detector 4010. Analysis undertaken in October and November 2012 were on Oxford Instruments X-Max 20mm$^{2.}$. Copper was used with the Oxford Instruments X-Max as a calibration standard at the beginning of the session, and checked back throughout the session to ensure there had been no instrument drift. Table 4.1 outlines the laboratory conditions for SEM sessions.

Table 4.1: SEM Laboratory Conditions for Mount Stafford Analysis Sessions

	March and April 2012	October and November 2012
Detector type	Bruker 133eV Xflash detector 4010	Oxford Instruments X-Max 20mm^2
SEM Machine	Zeiss EVO® MA 15	Zeiss EVO®
Software	Smart SEM	Aztec v2.0
Technique	SEM-EDS	SEM-EDS
Accelerating Voltage	15.0 kV	20.0 kV
Energy per Channel	15eV, 25eV	10.0eV
Amps	2.268 A	2.228 A
Scanning spot size	650 µm, 460 µm	620 µm
Probe current	10.1 nA	3.1 nA
Beam current	100.0 µA	60.0 µA
Output count rate	Not recorded	≈ 35000
Dwell time	Not recorded	10s
Images	CZ BSD	CZ BSD
Calibration Standard	Not recorded	100% Copper

Assessment of data quality

Energy Dispersive X-ray Spectroscopy (EDS) point sample data was obtained during SEM sessions which allowed quick determination of mineral grains and assemblages in thin section. Calibration during the session on 24/10/2012 had been changed post set up, which affected the readings of the light element boron for that day (up to 20% boron, instead of the expected 10%). Other element data for the session were found to be within error. Data for tourmaline recorded during SEM-EDS sessions was used for identification purposes, whilst EMP data from this study has been used for detailed tourmaline normalisation and analysis. SEM-EDS results are reported in Chapter 7 for the determination of the relationships between accessory phosphates.

Data reports are available from the analysis sessions undertaken on the Oxford Instruments X–Max, however due to the volume of reports, these will be provided electronically as part of this study's archive files.

4.6 Electron Microprobe (EMP) Chemical Analysis

One of the primary aims of this study is to categorise tourmaline across a range of metamorphic conditions and contrasting bulk rock compositions. The fine focus of an electron microprobe (EMP) beam allows for detailed spatial chemical and compositional analysis of in-situ tourmaline grains in thin section. Heavy elements reflect (backscatter) electrons more strongly than light elements, therefore heaver elements will appear as a brighter greyscale under BSE conditions (Potts, 1987).

Following identification of tourmaline grains through SEM-BSE and SEM-EDS analysis, rim and core electron microprobe analysis of multiple randomly-chosen tourmaline grains were undertaken on all eight thin sections (ST1119, ST1005, ST1106, ST1118). Backscattered electron images from samples ST1119 and ST1005 showed tourmaline grains with lighter and darker bands, which is an indication of chemical zonation. Rim-to-rim transect analysis was undertaken on selected tourmaline grains from these samples.

Thin sections were prepared using lint-free kimwipes and ethanol solution, and the previous carbon coating removed. Tourmaline grains of interest were circled using a smudge-proof felt-tipped pen, developing a map to allow ease of identification and location under a reflected light microscope (Appendix 5). Thin sections were then carbon-coated prior to EMP analysis.

EMP analysis was undertaken on 18/3/2013 and 8/4/2013, at the ARC National Key Centre for Geochemical Evolution and Metallogeny of Continents (GEMOC), based in the Department of Earth and Planetary Sciences at Macquarie University, North Ryde. Major element oxides assessed were K_2O, CaO, Na_2O, Fe_2O_{3tot}, Al_2O_3, TiO_2, MgO, SiO_2, Cr_2O_3, and MnO. Microprobe analysis was carried out on a Cameca SX100 electron microprobe using a 20.00nA beam current and accelerating voltage of 15keV, with a beam spot focussing of ≈5µm. Signals used for operation were Kα for: K, Ca, Na, Fe, Al, Ti, Mg, Si, Mn, Cr, which were run against individual calibration standards prior to the analysis session.

Assessment of data quality

Cameca SX100 electron microprobe lower limits of detection were provided by the laboratory, taken against a cpx background. Vienna (cpx) standard reference values were taken as unknowns during analysis, and compared to the long term standards for Vienna. Results are tabled in Appendix 12. Data for EMP tourmaline grain and tourmaline transects are presented in Appendix 13 and 14.

The observed Vienna standard reference values for both EMP analysis sessions (18/3/2013, 8/4/2013) were compared to the long term reference values (n=100). Of the ten unknowns (Vienna) analyses on 18/4, all of the values for Al_2O_3 and CaO values were low and outside error. Analysis for ten unknowns (Vienna) for Al_2O_3 and CaO on 8/4 were also low, with five Al_2O_3 within error and CaO having eight within error. These low results may have implications when categorising tourmaline, as both Al and Ca are critical chemical constituents of tourmaline.

5 Whole Rock Geochemistry

5.1 Introduction

This chapter aims to categorise the whole rock major and trace element data from the eight samples chosen for this study.

Metamorphic processes occur under primarily isochemical conditions, excepting the generation and loss of volatile components such as CO_2 and H_2O. Whole (bulk) rock compositional characteristics generally reflect the composition of the protolith (Vernon and Clarke, 2008). Whole rock composition is a control on the degree of partial melting. A rock which is considered more 'fertile', such as a metapelite, may display a higher level of melt fraction compared to less-fertile quartz-rich metapsammites (Sawyer, 2008). In this way, a local area may experience different percentages of melt production. In the presence of a driving force, the lighter and less viscous melt fraction can be driven away from the residual solid rock, resulting in melt loss and affecting the whole rock chemical composition. (Sawyer, 2008).

Samples from Mount Stafford used in this study are contrasting pairs of psammitic/pelitic beds from the same sample site, and it is envisaged that the analysis of whole rock characteristics will identify features of the associated protolith. XRF major, minor, and trace element data are presented in Appendix 9 and 11. Discussion of sample preparation and laboratory analysis is presented in Chapter 4.

For the purposes of categorising the samples based on major trends or anomalies in the whole rock data, major elements are presented in bivariate plots, and trace element data are presented in multi-element spider diagram, normalised to condrite C1 and presented in order of increasing compatibility**.** Mineral relationships in metamorphic systems are presented on ternary diagrams, such as the AFM diagram, and petrogenic grids, to predict metamorphic composition and mineral relationships in such systems as metapelitic systems (Vernon and Clarke, 2008). For the purposes of this study, a broad overview of whole rock mineral chemistry is sufficient to determine protolith, whilst descriptions of mineral relationships are provided in Petrography, Chapter 6.

5.2 XRF Whole Rock Major Element Analysis

Whole rock SiO2 wt% values for the study samples vary between 76.63 wt% and 56.76 wt%. Figure 5.1a SiO2 vs Al2O3 displays a inverse relationship between SiO2 and Al2O3. The eight samples a clustered in three groups, three samples having predominantly high Al2O3, two having high SiO2, and three with intermediate compositions.

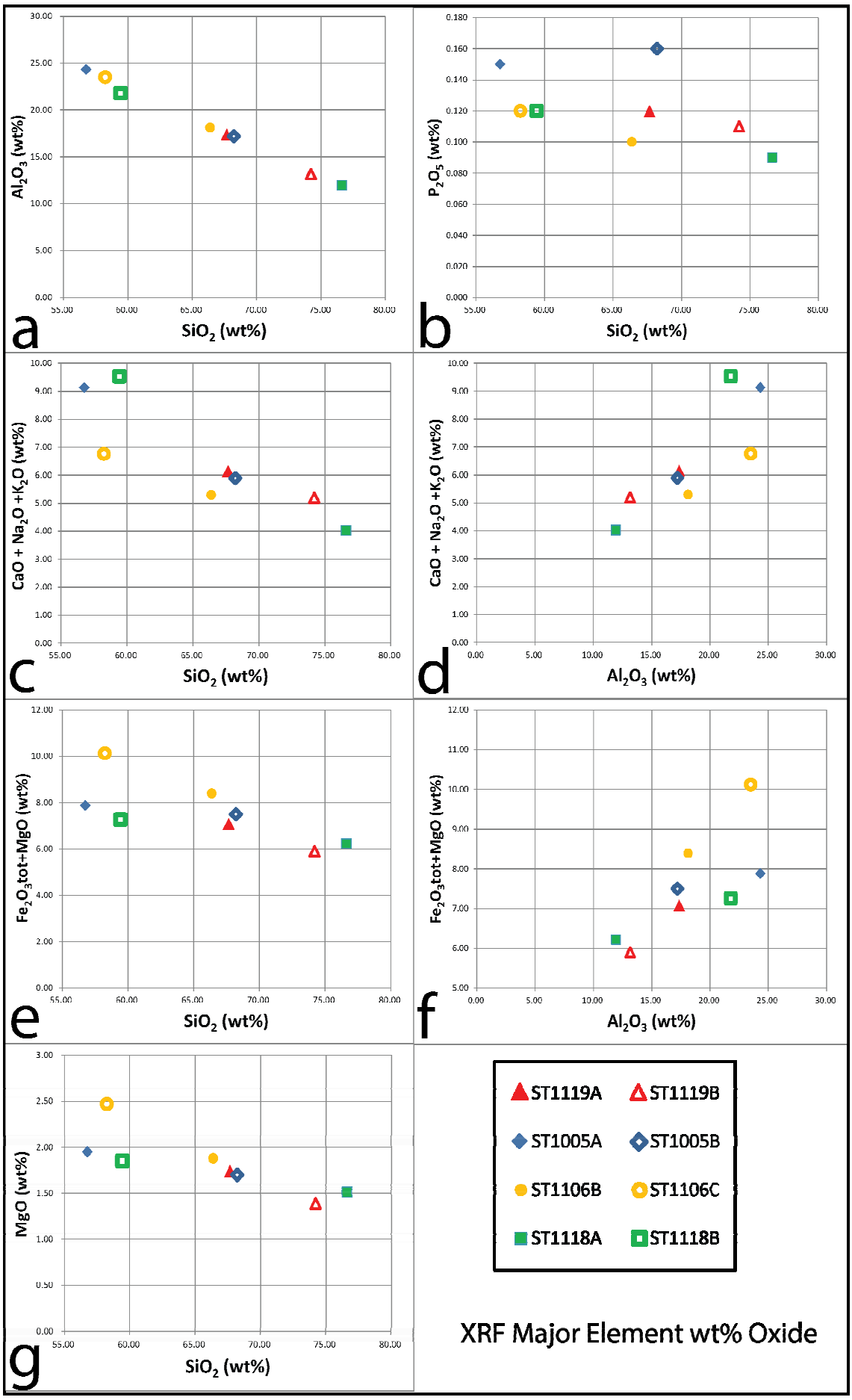

Figure 5.1: Bivariate Plots for Major Element Data

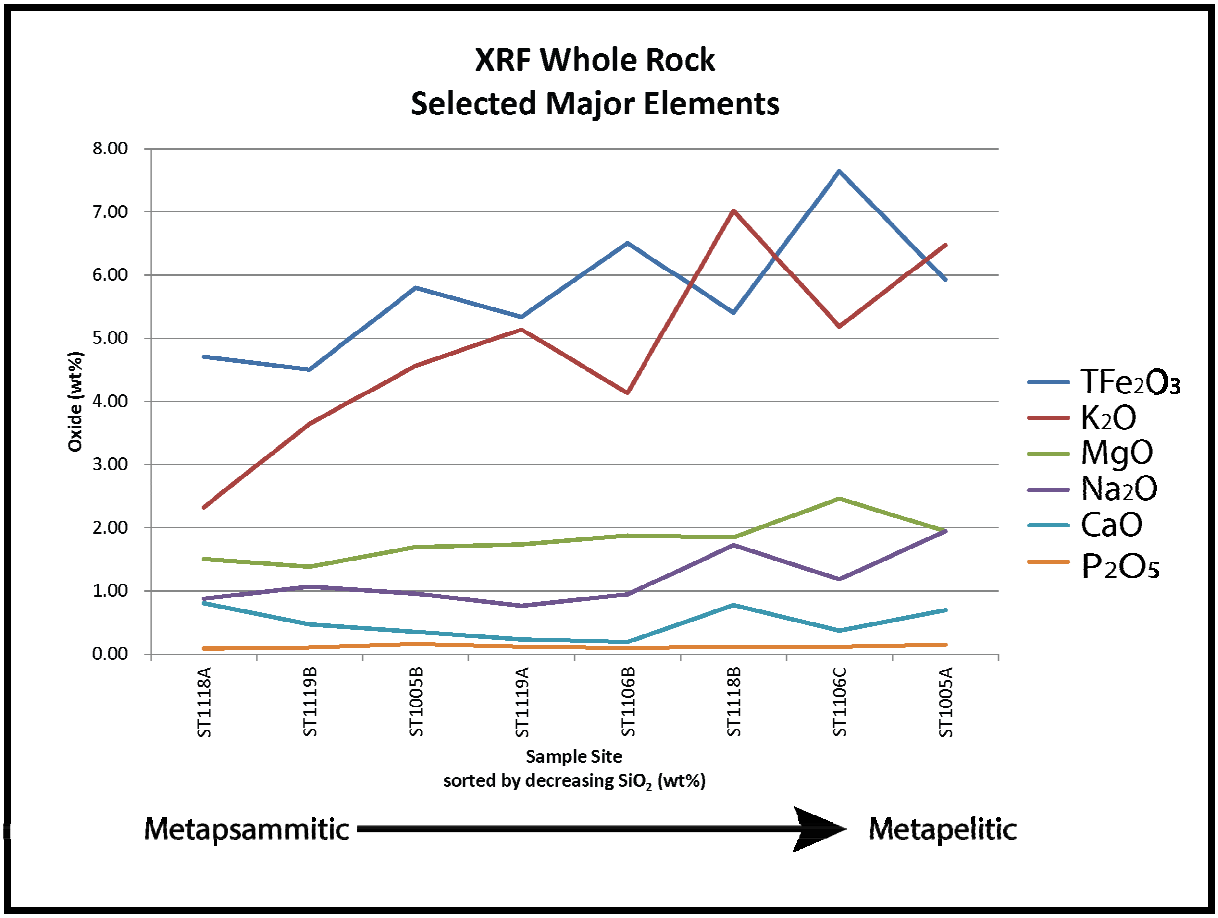

Figure 5.2: Trends in whole rock major and minor element chemistry (oxide wt%)

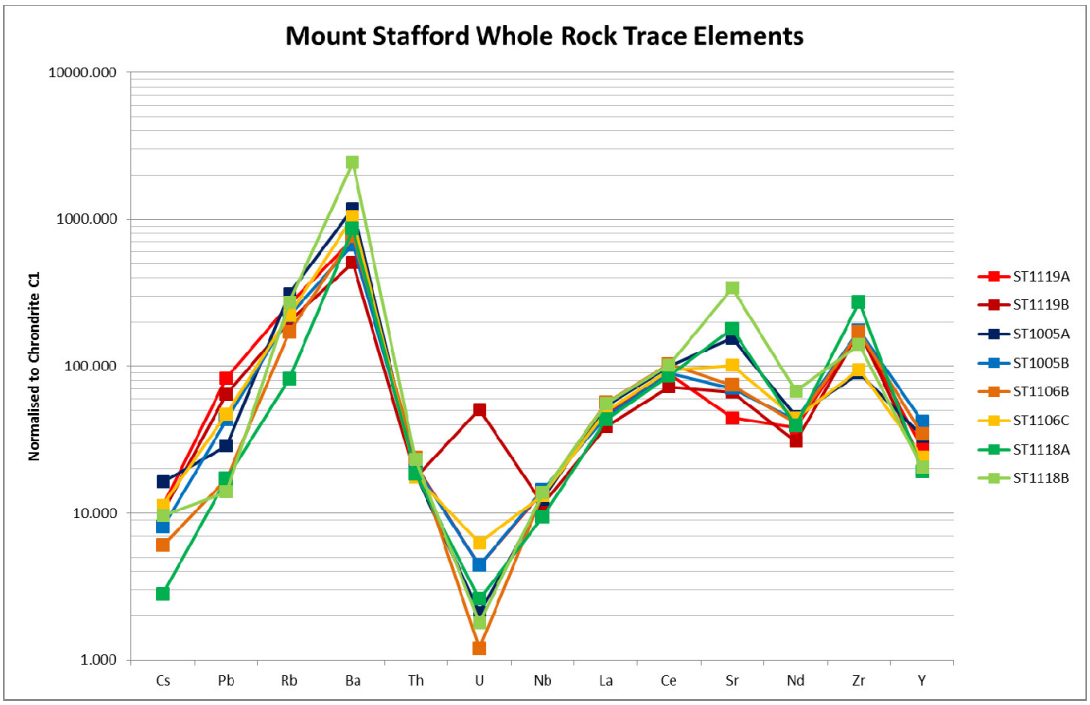

Figure 5.3: Trends in whole rock trace element chemistry (ppm)

6 Petrography

6.1 Introduction

The metasedimentary rocks at Mount Stafford preserve evidence of a lateral increase in metamorphic grade across an area of approximately 10km from greenschist facies in the south-west, through amphibolite to granulite facies in the north-east (Greenfield *et al.*, 1998; White *et al.*, 2003). The metapelite/metapsammite layers are interbedded on a less than decimetre scale, and display progressive evolution of migmatite development that can be related to an increase of temperature, ie: the rocks form a low-pressure high-temperature (LPHT) metamorphic terrain (Greenfield *et al.*, 1998).

In this chapter, petrographic analysis of mineral assemblage and metamorphic textures are undertaken on samples chosen from greenschist to upper amphibolite facies. Four areas from the Spring Creek transect are investigated (Refer: Figure 2.2), focusing on a pair of contrasting pelitic and psammitic samples. Samples have been identified from whole rock analysis as falling into three groups – aluminous metapelite (herein refer to as 'metapelite'), subaluminous metapelite, and metapsammite (Chapter 5).

Mineral identification for this section was undertaken referencing the publications (Augustithis, 1990; Deer *et al.*, 1992; MacKenzie and Guilford, 1980; Shelley, 1997; Vernon, 2004).

6.2 Mineral Assemblage Summary

6.3 ST1119 - Overview

Sample ST1119 represents a subaluminous metapelite / metapsammite pair which reached estimated metamorphic conditions of 2.5kbar at 625°C, which is below the metapelite solidus (White *et al.*, 2003). Modal proportions and grain size are shown in Table 6.1. The samples represent sedimentary rocks which have been heated, resulting in the formation of biotite and muscovite. The subaluminous metapelite has a greater modal proportion of K-feldspar, with andalusite present. The presence of cordierite was not located in thin section for either ST1119A or ST1119B, however this may be due to andalusite replacement of cordierite.

Summary of Mineral Modal Abundance and Size									
Sample number	Major Minerals	Mode %	Grainsize mm	Minor Minerals	Mode %	Grainsize mm	Accessory Minerals	Mode %	Grainsize mm
ST1119A	Quartz	35.3 ±10.0	< 1.0	Tourmaline	4.3 ±2.0	< 0.5	Accessories	0.8 ±0.3	< 0.1
Subaluminous	K-Feldspar (Microcline)	21.7 ±12.0	< 0.5				(Zircon, monazite,		
Metapelite	Biotite	14.3 ±2.5	< 0.5				apatite, illmenite)		
	Muscovite	12.8 ±4.0	< 0.5						
	Andalusite	10.0 ±3.5	< 2.0						
ST1119B	Quartz	51.5 ±7.9	< 1.0	K-Feldspar (Microcline)	9.2 ±5.8	< 0.3	Accessories	0.6 ±0.4	< 0.1
Metapsammite	Biotite	21.5 ±1.5	< 0.5	Tourmaline	3.2 ±2.8	< 0.5	(Zircon, monazite,		
	Muscovite	12.1 ±2.1	< 0.5				apatite, illmenite)		

Table 6.1: ST1119 Summary of Mineral Modal Abundance and Size

6.3.1 ST1119A – Subaluminous Metapelite

And-Bt-Ms-Qtz-Kfs hornfels
with: minor tourmaline and accessory ilmenite, monazite, apatite, zircon

In sample ST1119A, quartz grains are up to 1mm, angular to subrounded, and surrounded by a random matrix of fine grained muscovite, biotite and microcline. Quartz grain edges are predominantly serrated. Muscovite crystaloblasts are present up to 0.5mm. Microcline grains have random inclusions of rounded quartz and biotite laths. Crystalloblastic grains of andalusite are present up to 3mm in length with intergranular quartz (Fig 6-1). Tourmaline is present as zoned and unzoned subhedral grains up to 0.5mm. Some zoned tourmaline grains have rims containing small quartz inclusions, possibly representing detrital cores with a metamorphic overgrowth.

6.3.2 ST1119B - Metapsammite

Bt-Mus-Qz hornfels
with: minor microcline and tourmaline, and accessory ilmenite, monazite, apatite and zircon

Sample ST1119B has a greater modal proportion of quartz compared to ST1119A, although the quartz grains are a similar size <1.0mm. The overall texture is indicative of the sedimentary nature of the protolith, and is reflected in the poorly sorted angular to sub-rounded quartz grains, some of which appear weakly recrystallised from the original sediment. Microcline grains are poikiloblastic with inclusions of random rounded quartz and biotite laths. Muscovite crystalloblasts are also poikiloblastic (Fig 6.2). Tourmaline shows a similar morphology to ST1119A, with zoned and unzoned <0.5mm grains with inclusions in overgrowth rims.

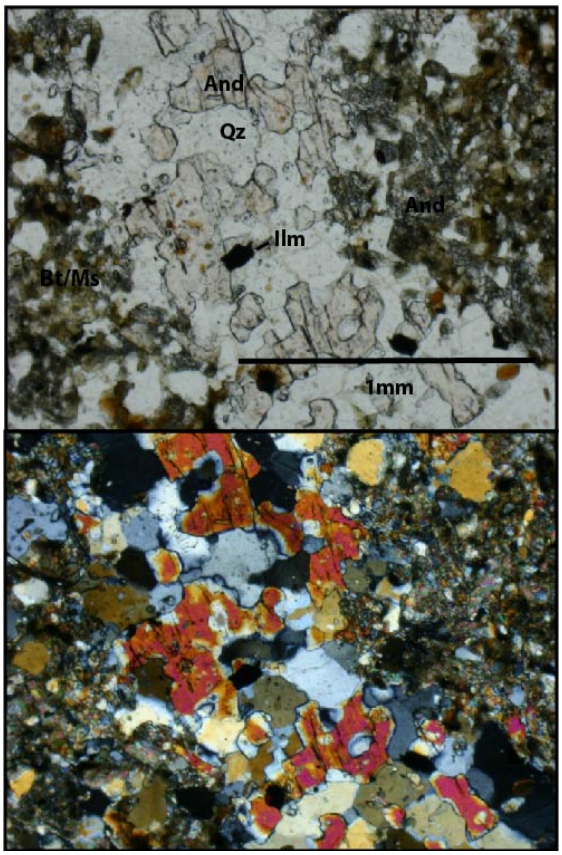

Figure 6.1: ST1119A And-Qtz-Ms-Bt PPL and XPL

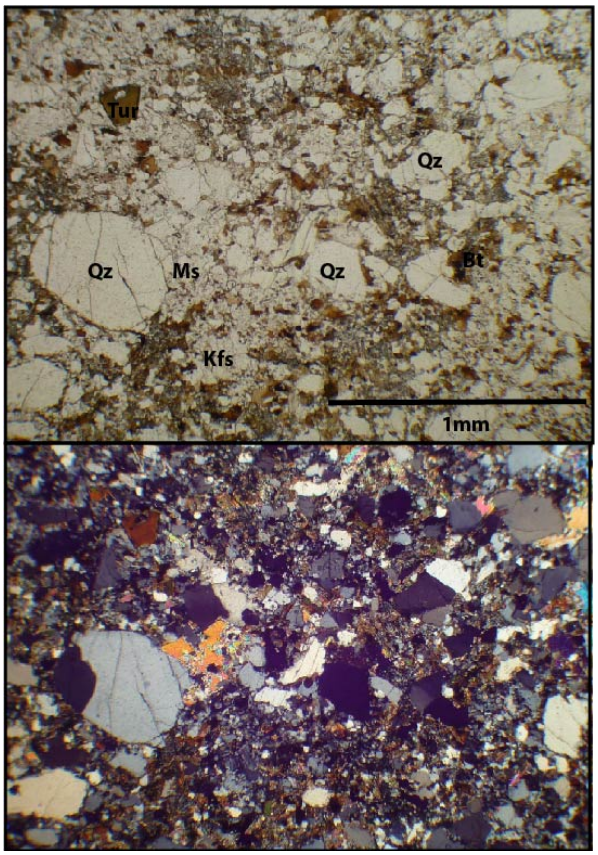

Figure 6.2: ST1119B Ms-Bt-Qz-Tur PPL and XPL

6.4 ST1005 - Overview

At estimated metamorphic conditions of 650°C and 2.7 kbar, both the metapelite (ST1005A) and subaluminous metapelite (ST1005B) show indications of partial melting (Greenfield *et al.*, 1998; White *et al.*, 2003). Modal proportions and grain size are shown in Table 6.2.

Summary of Mineral Modal Abundance and Size									
Sample number	Major Minerals	Mode %	Grainsize mm	Minor Minerals	Mode %	Grainsize mm	Accessory Minerals	Mode %	Grainsize mm
ST1005A	Quartz	17.0 ±2.0	< 2.0	Biotite	8.0 ±1.5	< 0.5	Accessories	0.2 ±0.1	< 0.2
Metapelite	K-Feldspar (Microcline)	30.3 ±5.0	< 1.0	Muscovite	7.0 ±0.5	< 0.5	(Zircon, monazite,		
	Andalusite	13.8 ±4.0	< 1.0	Sillimanite	3.0 ±0.5	< 0.5	apatite, illmenite)		
	Cordierite	14.3 ±3.5	< 2.0	Plagioclase	0.2 ±0.1	< 0.5			
	Tourmaline	9.5 ±1.0	< 3.0						
ST1005B	Quartz	40.2 ±2.0	< 1.0	Muscovite	5.5 ±0.5	< 0.5	Accessories	0.2 ±0.1	< 0.2
Subaluminous	K-Feldspar (Microcline)	28.5 ±3.5	< 0.5	Cordierite	5.0 ±2.3	< 0.5	(Zircon, monazite,		
Metapelite	Biotite	8.0 ± 1.0	< 0.5	Tourmaline	0.5 ±0.1	< 0.1	apatite, illmenite)		
	Andalusite	8.0 ±0.5	< 0.2	Garnet	0.1 ±0.0	< 0.5			
	Sillimanite	8.0 ±0.5	< 0.1						

Table 6.2: ST1005 Summary of Mineral Modal Abundance and Size

6.4.1 ST1005A - Metapelite

Sil-Crd-And-Kfs-Qz-Tur
with: minor biotite and muscovite and accessory zircon, monazite, apatite, illmenite

Microcline and quartz-rich areas in the thin section for ST1005A cover areas up to 2cm across. Microcline in these regions is euhedral, ≈0.5 to 1mm, commonly rectangular, with rounded inclusions of biotite, muscovite, quartz, and rare monazite in the centre of grains. Quartz is interstitial between microcline grains, optically continuous with undulose extinction and low dihedral angles (Fig 6.3). Sillimanite is present as prismatic grains and blades with biotite and as blades within andalusite. Cordierite grains are evident up 2mm however are commonly pseudomorphed by xenoblastic sillimanite, biotite and quartz. Tourmaline forms subhedral idioblastic grains up to 3mm and ≈10% modal abundance in thin section. Biotite shows pleochroic halo damage from abundant micro-zircons.

6.4.2 ST1005B – Subaluminous Metapelite

Sil-And-Grt-Kfs-Qtz-Ms-Bt
with: accessory zircon, monazite, apatite, ilmenite,

Microcline is idioblastic, up to 0.5mm. Quartz is found as optically continuous, interstitial, with undulous extinction and low dihedral angles, and as grains with serrated edges in a decussate mosaic texture. Fibrous symplectites of biotite and sillimanite occur, as well as quartz/silimanite symplectites (Fig: 6.4). Tourmaline is small (≈0.2mm) and bright blue. It has a skeletal form with quartz intergrowths, and is commonly enclosed in biotite. Tourmaline is observed to form rims around biotite crystalloblasts. A single grain of garnet exists in the thin section.

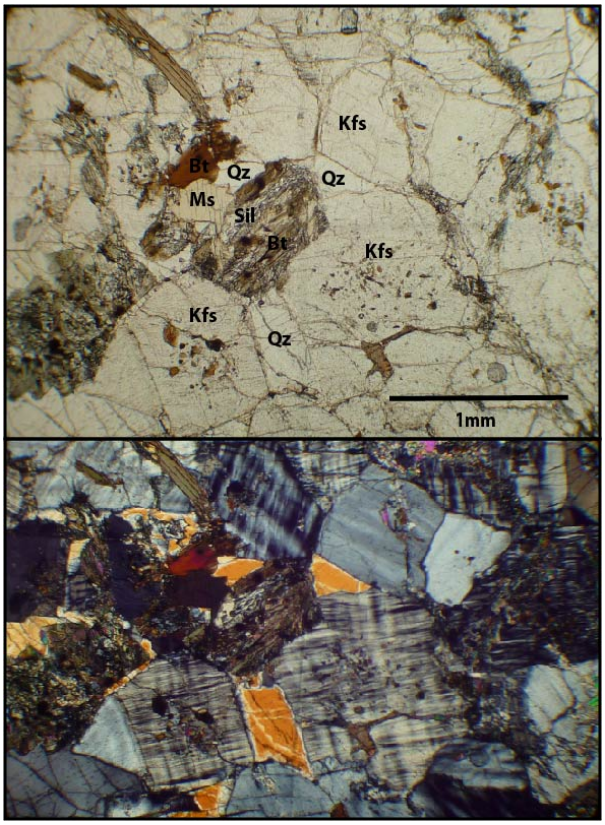

Figure 6.3: ST1005A Sil-Bt-Kfs-Ms-Qz PPL and XPL

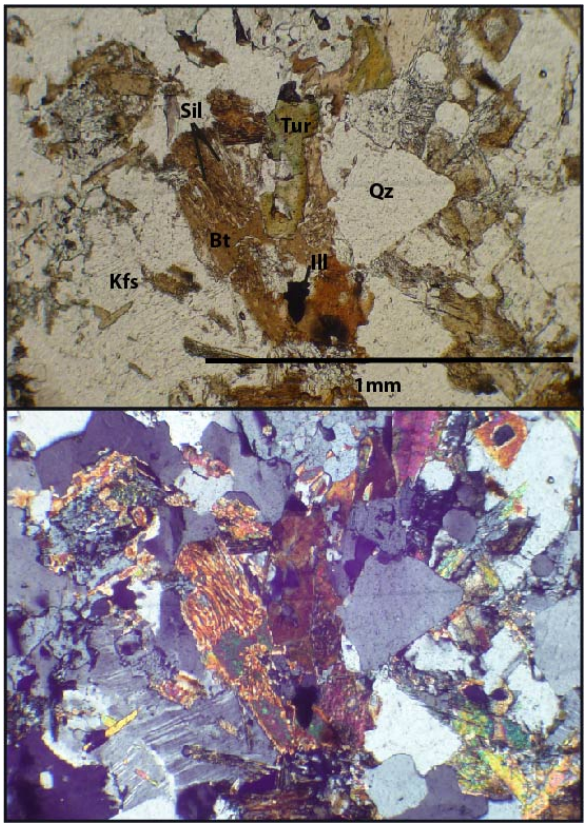

Figure 6.4: ST1005B Sil-Bt-Kfs-Qz-Ilm-Tur PPL and XPL

6.5 ST1106 overview

Sample ST1106 was taken from an outcrop of a schileren migmatite. Estimated metamorphic conditions were ≈650-680°C and ≈2.9-3.3 kbar (White *et al.*, 2003). Modal proportions and grain size are shown in Table 6-3.

Summary of Mineral Modal Abundance and Size									
Sample number	Major Minerals	Mode %	Grainsize mm	Minor Minerals	Mode %	Grainsize mm	Accessory Minerals	Mode %	Grainsize mm
ST1106A	Quartz	15.0 ±3.0	< 1.0	Biotite	5.0 ±1.5	< 0.5	Accessories	1.0 ± 0.2	< 0.1
Subaluminous Metapelite	K-Feldspar (Microcline)	60.0 ±5.0	< 2.0	Tourmaline	2.0 ±0.5	< 0.5	(Zircon, monazite,		
Section	Cordierite	15.0 ±3.0	< 1.0	Sillimanite	5.0 ±1.0	< 0.2	apatite, illmenite,		
							spinel)		
ST1106A	Quartz	80.0 ±1.0	< 1.0	Sillimanite	2.0 ±0.5	< 0.1	Accessories	1.0 ±0.2	< 0.1
Metapsammite	K-Feldspar (Microcline)	10.0 ±1.0	< 0.3	Tourmaline	1.0 ±0.5	< 0.2	(Zircon, monazite,		
section	Biotite	10.0 ±2.0	< 0.3				apatite, illmenite)		
ST1106D	Quartz	15.0 ±5.0	< 1.0	Biotite	5.0 ±1.5	< 0.5	Accessories	1.0 ± 0.3	< 0.2
Metapelite	K-Feldspar (Microcline)	60.0 ±5.0	< 2.0	Tourmaline	2.0 ±0.5	< 0.5	(Zircon, monazite,		
	Cordierite	15.0 ±2.0	< 1.0	Sillimanite	5.0 ±1.0	< 0.2	apatite, illmenite,		
							spinel)		

Table 6.3: ST1106 Summary of Mineral Modal Abundance and Size

6.5.1 ST1106A –Subaluminous Metapelite and Metapsammite

This thin section has two distinct zones with contracting bulk rock composition: metapelite and metapsammite.

Subaluminous Metapelite: Crd-Sil-Spl-Qz-Kfs-Bt
with: minor ilmenite and accessory monazite, zircon, apatite, tourmaline

Metapsammite: Qz-Kfs
with: minor biotite, ilmenite and accessory monazite, zircon, apatite, xenotime

The subaluminous metapelite has idioblastic rectangular microcline up to 1mm, with interstitial optically continuous quartz between the microcline grains. Cordierite exists as rounded inclusion free grains, and as euhedral poikiloblastic grains with inclusions of quartz, biotite and spinel. Both forms of cordierite display evidence of pinite alteration along grain boundaries and fractures. Small 0.05mm euhedral dark green granular spinel (hercynite) grains form as inclusions within quartz with biotite in cordierite and microcline, and amongst swarms of sillimanite needles. Tourmaline is evident as interstitial grains up to 0.5mm.

Between the subaluminous metapelite and metapsammite is a dark selvedge, of biotite, ilmenite & fibrolite, with zircon, monazite and tourmaline (Fig: 6.5). Ilmenite in the selvedge are anhedral, up to 0.5mm, and commonly have inclusions of monazite.

The metapsammite has a fine-grained decussate texture, with quartz up to ≈80% by mode. Quartz has serrated edges and is ≈0.5mm in size. Microcline is interstitial to the quartz up to <0.5mm. There is minor biotite with fibrous sillimanite, along with occasional bright blue tourmaline grains with quartz inclusions.

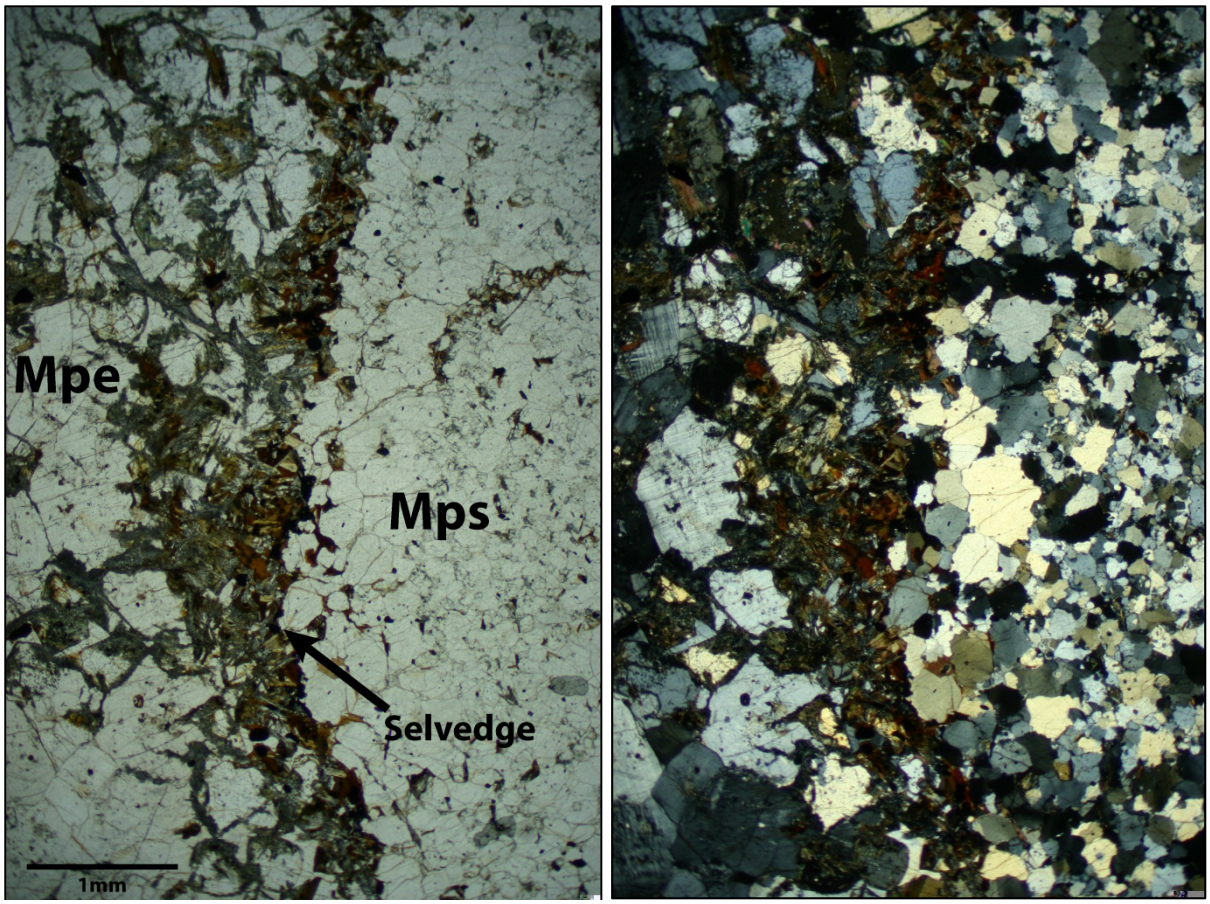

Figure 6.5: ST1106A: Showing metapelite– mafic-rich selvedge – metapsammite comparison of bulk rock compositions separated by a Ilm/Bt rich selvedge
Left: PPL. Right: XPL.

6.6 ST1106D - Metapelite

Crd-Sil-Spl-Qz-Kfs-Bt
with: minor ilmenite and tourmaline and accessory monazite, apatite, zircon

ST1106D is very similar to the subaluminous metapelite section of ST1106A. There is a similar modal proportion of cordierite, microcline, sillimanite, biotite and quartz. The dark green granular spinel (hercynite) inclusions in cordierite and microcline are slightly larger, up to ≈0.1mm. Tourmaline is blue-yellow, anhedral and commonly located with pinite along grain boundaries of cordierite (Fig: 6.6).

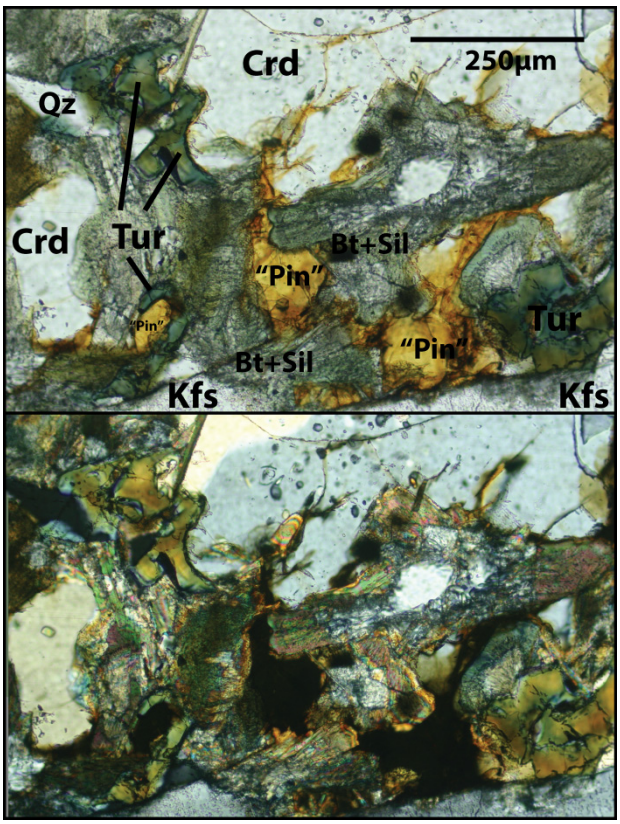

Figure 6.6: ST1106D. Crd with Tur, "Pin", Kfs, Bt+Sil

6.7 ST1118 overview

Site ST1118 contains the highest grade rocks examined in this study, and are estimated to be at peak conditions of ≈780°C and >3.0 kbar (White *et al.*, 2003). Modal proportions and grain size are shown in Table 6.4.

Summary of Mineral Modal Abundance and Size									
Sample number	Major Minerals	Mode %	Grainsize mm	Minor Minerals	Mode %	Grainsize mm	Accessory Minerals	Mode %	Grainsize mm
ST1118A	Quartz	80.0 ±5.0	< 1.0	Biotite	5.0 ±3.0	< 1.0	Accessories	0.2 ±0.1	< 0.1
Metapsammite	K-Feldspar (Microcline)	10.0 ±2.0	< 0.5	Sillimanite	1.0 ±0.2	< 0.2	(Zircon, monazite,		
				Cordierite	1.0 ±0.2	< 0.5	apatite, illmenite)		
				Plagioclase	0.5 ±0.1	< 0.5			
				Garnet	0.5 ±0.1	< 0.5			
ST1118B	Quartz	15.8 ± 8.0	< 1.0	Sillimanite	1.0 ±0.2	< 0.2	Accessories	0.2 ±0.1	< 0.1
Metapelite	K-Feldspar (Microcline)	10.5 ±2.0	< 1.0	Biotite	7.0 ±1.5	< 0.5	(Zircon, monazite,		
	Cordierite	35.5 ±5.5	< 10.0	Tourmaline	0.1 ±0.1	< 0.2	apatite, illmenite)		
				Spinel	1.0 ± 0.5	< 0.2			

Table 6.4: ST1118 Summary of Mineral Modal Abundance and Size

6.7.1 ST1118A - Metapsammite

Qtz-Kfs-Bt
with: minor cordierite, sillimanite, plagioclase and garnet, and accessory zircon, monazite and apatite

Quartz grains in ST1118A have a decussate interlocked texture, and are elongate along a weak foliation. Quartz grains are serrated and commonly have semi-circular embayments, and have rounded quartz and biotite lath inclusions (Fig: 6.7). Embayed cordierite ≈0.5mm has quartz inclusions. Biotite/sillimanite symplectites are evident. Garnet is idioblastic and in contact with biotite.

6.7.2 ST1118B - Metapelite

Crd-Kfs-Sp-Bi-Qz
with: minor garnet, tourmaline, ilmenite and accessory zircon, monazite, apatite

Bright-green spinel, <100µm octahedral, anhedral and rounded grains forming in clusters along edges of cordierite and inside cordierite as inclusions. Idioblastic garnet is found with biotite. Bright blue tourmaline is located within cordierite as inclusions. Poikiloblastic cordierite grains, up to 3mm, contain graded inclusions; Cordierite grains have fine inclusions in the core ≈0.02mm, an inner rim of larger inclusions ≈0.05mm, and an outer rim with the coarsest inclusions ≈0.1mm. This growth pattern is more evident on the largest of the cordierite grains, and is asymmetric. Along the grain edge with the largest inclusions is a spinel rim, which separates the cordierite from a leucosome band of euhedral rectangular microcline and interstitial optically continuous quartz.

Figure 6.8 shows spinel in the centre of a quartz-rich vein. Quartz has developed with c-axis preferred orientations perpendicular to each side of the vein, with spinel forming in a band in between. C-axis preferred growth of quartz is also evident, where quartz has crystallised along the edge of a cordierite grain, with spinel between the cordierite and quartz.

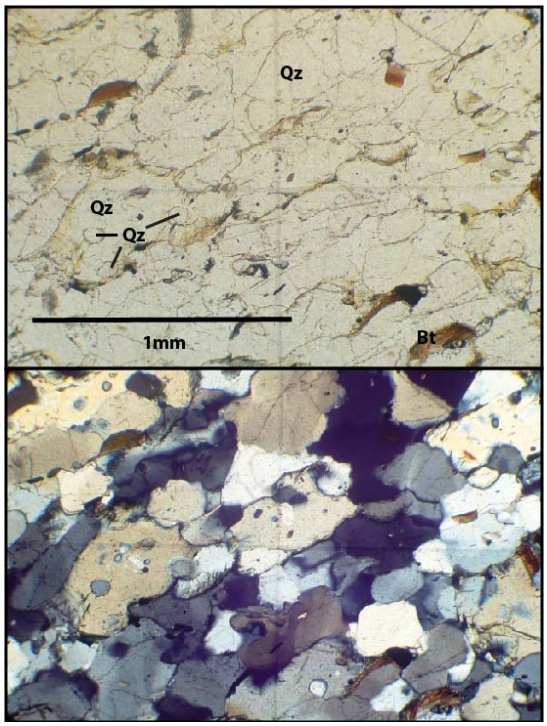

Figure 6.7: ST1118A showing Qz partial melt texture PPL and XPL

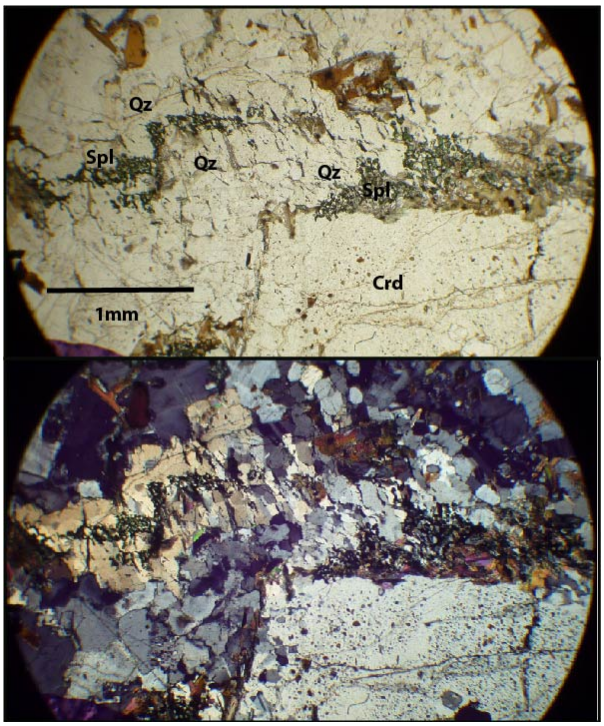

Figure 6.8: ST1118B showing Qz vein with Spl PPL and XPL

7 Mount Stafford – Accessory Phosphate Behaviour

7.1 Introduction

This section focuses on the behaviour of accessory phosphates, to determine whether phosphate accessory phases with comparative bulk rock chemistry (aluminous pelite / psammite) react in a predictable manner with increasing metamorphic grade. Common phosphate accessory minerals in the Mount Stafford metapelites and metapsammites are monazite, apatite and xenotime (Rubatto *et al.*, 2006) (& this study).

7.1 Overview: Accessory Phosphates

Accessory mineral phases can be important indicators of the development of mineral assemblages in metamorphic environments (Wark and Miller, 1993). Accessory phases can host the majority of trace and radioactive elements used in isotopic and geochronological investigations, and due to some accessory mineral's mechanical and geochemical stability can be used as indicators of source materials and evolution of melt composition (Wark and Miller, 1993). The majority of a trace element budget (REE, P, Y, Zr, Hf) can be held in a rock's accessory minerals so the growth or consumption of accessory minerals present can be a primary control the distribution of trace elements throughout a rock (Pyle and Spear, 2003).

7.1.1 Metamorphic Apatite

Apatite is a common accessory mineral in metamorphic rocks, and can be found in rocks with a diverse range of bulk compositions, and at various metamorphic grades from low-temperature alteration, migmatites, through to ultra high-pressure environments. The occurrence of apatite is dictated by the availability of key constituents, namely P, Ca and F which are found in greater than trace levels in most rocks, and it's stability is not considered to be controlled by other locally occurring phosphates (Spear and Pyle, 2002). The chemical formula of apatite is:

Apatite: $Ca_5(PO_4)_3(F,OH,Cl)$

Three key apatite end members are [$Ca_5(PO_4)_3F$] fluorapatite, [$Ca_5(PO_4)_3OH$] hydroxylapatite and [$Ca_5(PO_4)_3Cl$] chlorapatite. Metamorphic apatite is typically within the fluorapatite range, with compositions becoming OH and Cl depleted with increasing metamorphic grade (Spear and Pyle, 2002)

Substitutions are usually as trace amounts, and include Ca substitution for the cations K, Na, Mn, Ni, Cu, Co, Zn, Ba, Cd, Sr, Ba, Pb, Sb, Y, U and REEs, and replacement of PO_4^{3-} by anionic complexes such as $AsO_4^{3-,}$ SO_4^{2-}, CO_3^{2-} and SiO_4^{4-}. (Hughes and Rakovan, 2002). Minor elements Mg, Fe and Mn are found at low concentrations of less than 0.1 cations/8 oxygens. Apatite coexisting with monazite in pelitic systems typically have low REE contents, however higher concentrations may occur due to tiny inclusions of monazite and xenotime in apatite (Spear and Pyle, 2002).

7.1.2 Metamorphic Monazite and Xenotime

Monazite and xenotime are orthophosphates with the general formula $A(PO_4)$, where A is LREE for monazite (usually La, Ce, Nd, Pr), and Y, HREE for xenotime (Hughes and Rakovan, 2002). The chemical formula of monazite and xenotime is

Monazite: $[(LREE)PO_4]$ Xenotime: $[(Y, HREE)PO_4]$

Both xenotime and monazite are accessory minerals in a wide range of rocks including granites, pegmatites, gneisses, carbonates, migmatites and quartz veins, along with having the mechanical and chemical stability to survive weathering processes to be included in alluvial deposits (Hughes and Rakovan, 2002). They are abundant in metapelitic rocks but are less commonly found in rocks with more calcic and mafic bulk compositions (Spear and Pyle, 2002). Monazite has been reported in metamorphic systems from low pressure contact aureoles through to granulite facies and ultra high-pressure pelitic rocks. Monazite incorporates uranium and thorium, to the point where it is used as an ore for thorium and a secondary source of uranium (Spear and Pyle, 2002).

Xenotime has been found in rocks from the chlorite zone through to corderite+K-feldspar zones. In garnet zones, xenotime can be found in the rock matrix however if garnet is present, it may be consumed as garnet grows and incorporates Y and HREE. If garnet is absent, xenotime can be present in all metamorphic grades (Spear and Pyle, 2002).

7.1.3 Phosphate solubility in melts

Monazite stability can depend on P-T conditions, neighbouring mineral compositions, and the composition of any metamorphic and/or hydrothermal fluids present (Ondrejka *et al.*, 2012).

The breakdown reaction of monazite is controlled by the Ca and Na content of fluid present. If the Ca content is lowered and Na content increased, the solubility of monazite is decreased and other mineral formation, such as allanite, is promoted at the expense of apatite. If the fluid has an excess of K, the growth of allanite is supressed and precipitation of apatite and secondary monazite is promoted (Ondrejka *et al.*, 2012). Common products of metamorphic breakdown of monazite $(Ce,La,Nd,Pr)PO_4$ are apatite $Ca_5(PO_4)_3(F,Cl,OH)$, huttonite or thorite ($ThSiO_4$), allanite-(Ce) $(Ce,Ca,Y,La)_2(Al,Fe^{+3})_3(SiO_4)_3(OH)$, epidote $Ca_2Al_2(Fe^{3+};Al)(SiO_4)(Si_2O_7)O(OH)$, or clinozoisite (a form of epidote) (Ondrejka *et al.*, 2012).

Accessory phosphates have a relatively low integranular diffusion rate under metamorphic conditions. If a reaction phase proceeds, the rim of a grain may be affected to a greater extent than the core, leading to chemical zoning (Spear and Pyle, 2002). Zoning observed in apatite, xenotime and monazite may also be further complicated by multiple episodes of growth and resorption, and it is therefore not straightforward to demonstrate that a particular growth zone has been in equilibrium with any other phase. Approaches in assessing equilibrium in these minerals commonly include relationship with garnet, textural analysis, evaluation of element partitioning and chemical zoning, and thermodynamic modelling (Spear and Pyle, 2002).

7.2 Mount Stafford Accessory Phosphates

7.2.1 Methodology

The occurrence and textural relationships between apatite, monazite and xenotime was investigated. scanning electron microscope back scatter electron (SEM-BSE) imaging of this study's petrographic thin sections was undertaken to determine mineral occurrence and textural relationships. Details recorded were grain size, internal structure, and mode to assist in determine dissolution/precipitation relationships.

Refer to Chapter 4 for laboratory conditions and Appendix 6 for scanning electron microprobe (SEM) maps of thin sections.

SEM conditions were updated during analysis, to ensure the best resolution for investigation of internal zoning. This was done by lowering the scanning spot size from 650µm to 500µm to 460µm, and increasing the voltage from 15 kV to 25 kV. Table 7.1 provides a summary of this study's petrographic observations, the rock type as identified through whole rock analysis, and the estimated temperature and pressure for each sample site based on White *et al*, 2003.

Table 7.1 – Summary of Apatite, Monazite and Xenotime

Summary of Apatite, Monazite and Xenotime - mode, size, form and textural relationships

					Apatite	100 = all accessories		Monazite	100 = all accessories		Xenotime	100 = all accessories		
Approx. Zone	**Sample site**	**Rock type**	**Estimated T***	**Estimated P***	**Size**	**Mode**	**Form**	**Size**	**Mode**	**Form**	**Size**	**Mode**	**Form**	**Notes**
2a	ST1119A	Subaluminous Metapelite	≈625°C	≈2.5 kbar	20-120µm	20/100	Round to euhedral, slightly embayed	Matrix - ≈10-50µm Rims - ≈10µm	15/100	Larger single grains in matrix. On rims of apatite	N/A	0/100	Not observed	
	ST1119B	Metapsammite			10-100µm	20/100	Round to euhedral, slightly embayed	Matrix - ≈10-20µm Rims - ≈10µm	15/100	Matrix varied from euhedral to embayed. Mnz in Ap was embedded	≈10µm	3/100	rare individual grains in matrix	
2c	ST1005A	Metapelite	≈650°C	≈2.7 bar	10-20µm	5/100	tear-shaped. Occ. w. Mnz on rim	Matrix - ≈10-25µm Rims - ≈10µm	25/100	euhedral, with internal zoning	≈10µm	3/100	within Tourmaline	Monazite mode and grain size increase, apatite mode and grain size decrease
	ST1005B	Subaluminous Metapelite			20-120µm	20/100	Round to euhedral, slightly embayed	Matrix - ≈10-50µm Rims - ≈10µm	15/100	Euhedral to subhedral, matrix, inclusions in Ap, grain boundary on Ilm, Ap.	≈10µm	0.5/100	Single matrix grain observed.	Big difference between Sub-Al Metapelite and the Metapelite. The metapelite Ap were much smaller, whereas the sub-Al metapelite was similar to ST1119A - not much in the way of mode or form changes
3	ST1106A	Subaluminous Metapelite	≈650-680°C	≈2.8-3.3 kbar	20-120µm	15/100	Euhedral to anhedral, conact with Ilm	5-50µm	15/100	In matrix, and grain boundary on Ap.	≈20µm	5/100	Grain boundary and inclusions in Ap	
	ST1106A	Metapsammite			50-250µm	20/100	large anhedral grains up to 250µm	20-50µm	15/100	inside rims of apatite (embayed)	N/A	0/100	Not observed	metapsammite had Ap with Mz and Xtm on rims. Very large apatites Theory: that there was less available REE to form Mz and Xtm, so whatever free P there was went to Ap formation. Also - Ap have mutiple accessories on rims - zircon, Mz, Ilm, Xtm.
	ST1106D	Metapelite			20-50µm	25/100	in quartz, along with other incompatible accessory minerals	20-50µm	25/100	embayed within rims of ilmenite - may have nucleated, and ilm grown around?	20-40µm	10/100	in quartz, along with other incompatible accessory minerals	
3	ST1118A	Metapsammite	≈740 deg°C	>3.0 kbar	10-75µm	20/100	Large anhedral grains	10-100µm	10/100	inside rims of apatite (embayed)	≈10µm	5/100	In matrix, and grain boundary on Ap.	Very similar to metapsmmite of ST1106A - large apatite with Mnz and Xtm on rims
	ST1118B	Metapelite			10-50µm	5/100	small grains within Crd	10-30µm	20/100	In matrix with Spinel, and small grains within Crd also with spinel	≈10µm	5/100	In Crd located on on Ap grain boundary, no single grains	

* White *et al* (2003) - temperature estimates and melt proportions for different rock types at Mount Stafford

7.3 ST1119 Phosphates

ST1119A – Subaluminous Metapelite

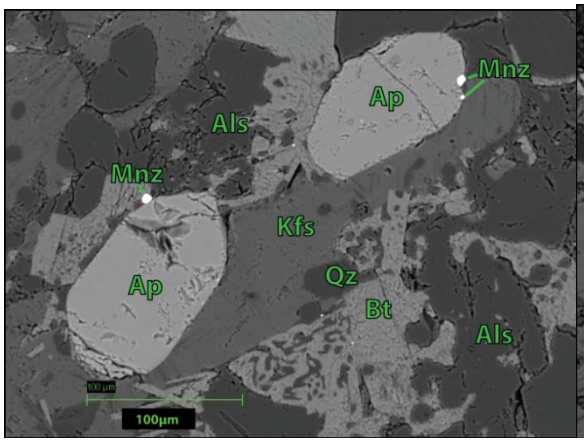

Figure 7.1: ST1119A - Apatite, with monazite on grain boundary

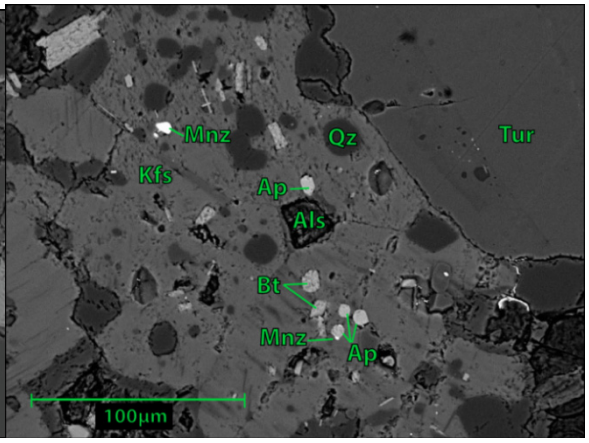

Figure 7.2: ST1119A - Matrix monazite and apatite

Apatite in ST1119A is euhedral, with slight embayments and between 20-150µm. Monazite is observed as matrix grains 20-50µm, or on apatite grain boundaries ≈10µm.

ST1119B - Metapsammite

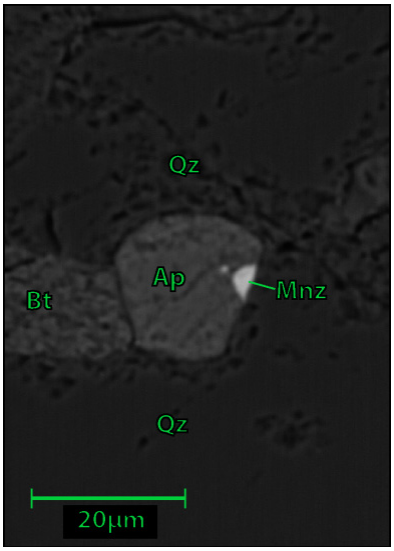

Figure 7.3: ST1119B - Apatite, with monazite inside grain boundary

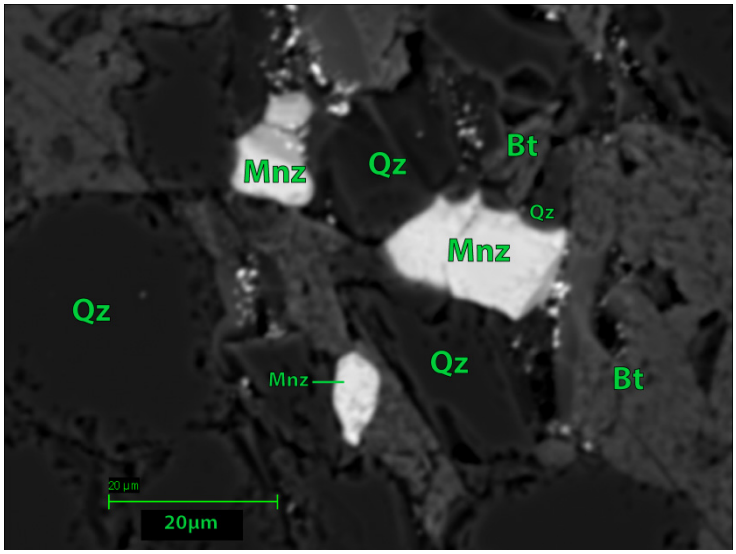

Figure 7.4: ST1119B - Matrix monazite and apatite

Apatite is euhedral, 20-50µm. Monazite is located in the matrix and on apatite grain boundaries. Monazite on apatite grain boundary is embedded into the grain rather than along the edge. Xenotime ≈30µm was observed in the matrix as an inclusion within biotite.

7.4 ST1005 Phosphates

ST1005A – Metapelite

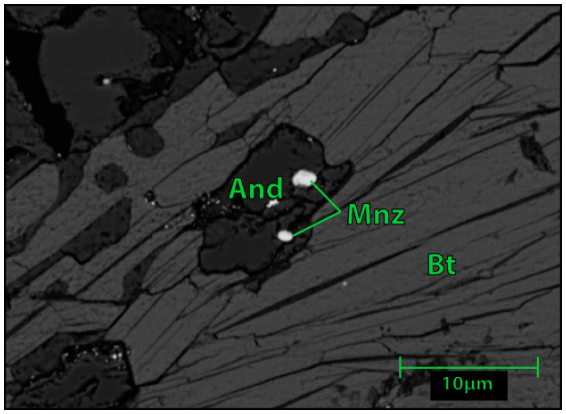

Figure 7.5: ST1005A - Monazite in Andalusite

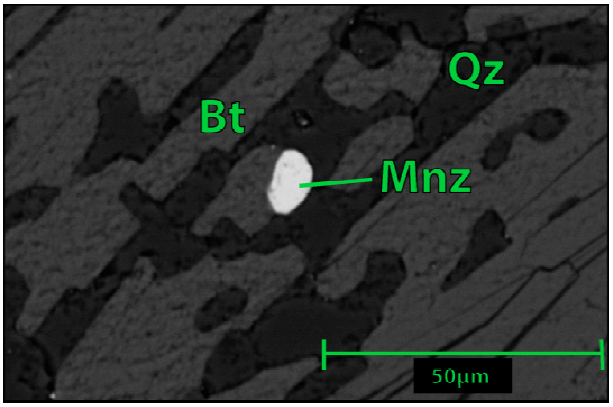

Figure 7.6: ST1005A - Monazite with biotite and quartz

Monazite in this sample is observed in tourmaline, biotite, andalusite, K-feldspar and quartz, and euhedral grains up to <50µm. Xenotime and monazite were observed as inclusions in large metamorphic tourmaline grains, and may have been trapped as inclusions during growth of tourmaline from B-rich fluids.

Mode and size of apatite has reduced between grades. Mode and size of monazite had increased, whilst xenotime occurrences are similar to ST1119.

ST1005B – Subaluminous Metapelite

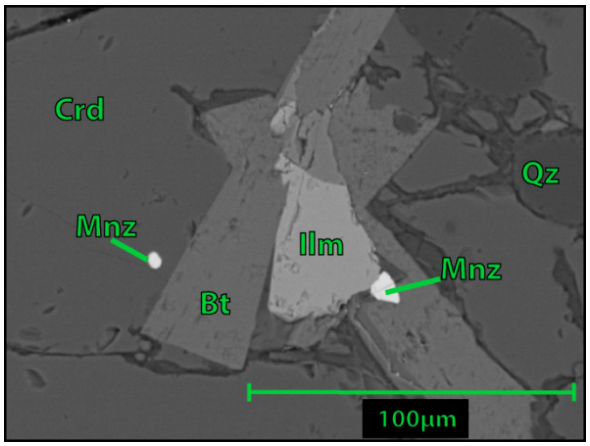

Figure 7.7: ST1005B - Apatite, with monazite on grain boundary

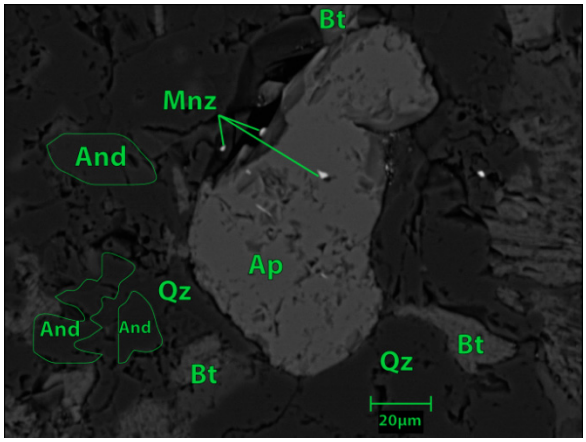

Figure 7.8: ST1005B - Apatite and Ca-rich monazite

Large apatite grains 20-120µm are subhedral and embayed. Apatite has been observed with high-Ca monazite. This mineral was investigated as epidote, however does not have any Al, Fe or Mn. There is a relationship between ilmenite grains and monazite forming along grain boundaries. A single grain of xenotime was observed.

7.5 ST1106 Phosphates

ST1106A – Metapsammite

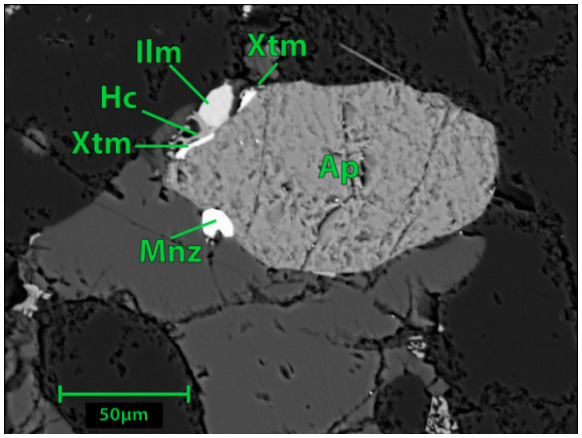

Figure 7.9: ST1106A - Apatite with Monazite, Xenotime and Ilmenite

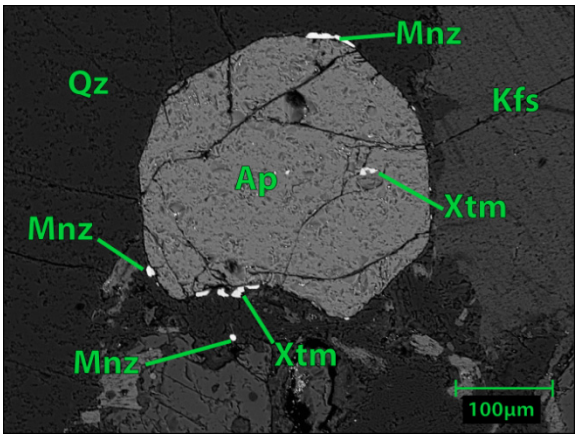

Figure 7.10: ST1106A - Apatite, Monazite and Xenotime

Apatite in metapsammite section of the thin section are large, up to ≈250µm. Apatite has xenotime inclusions, along with xenotime, monazite and ilmenite on apatite rims. Apatite is subhedral to euhedral, ≈40-120µm. Monazite is observed on the rim of apatite.

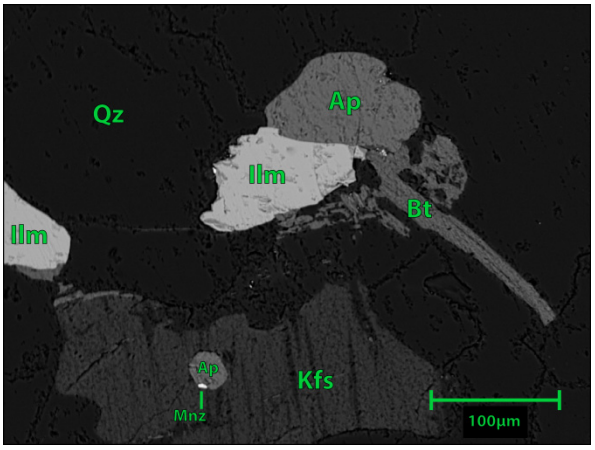

Figure 7.11: ST1106A – Metapsammite – Apatite and Ilmenite

ST1106D - Metapelite

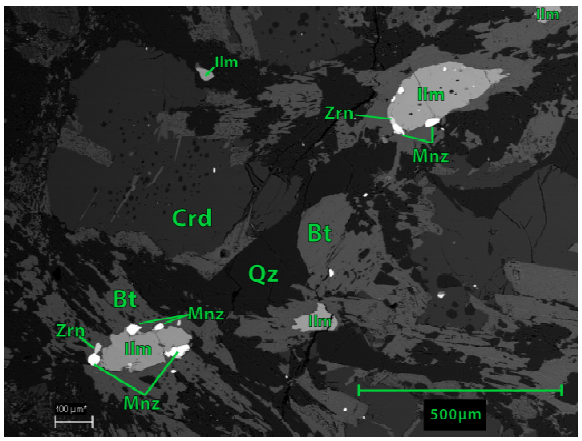

Figure 7.12: ST1106D – Relationship between monazite and ilmenite

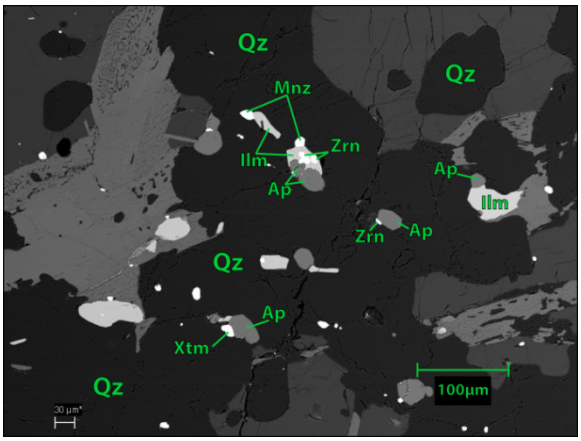

Figure 7.13: ST1106D – Incompatible accessory minerals in quartz

Zircon and monazite are observed to be located along the grain boundary of ilmenite, in a similar manner to having been observed on the grain boundaries of apatite. Figure 7.13 shows a number of incompatible accessory minerals (apatite, zircon, monazite, ilmenite, xenotime) in quartz.

7.6 ST1118 Phosphates

ST1118A – Metapsammite

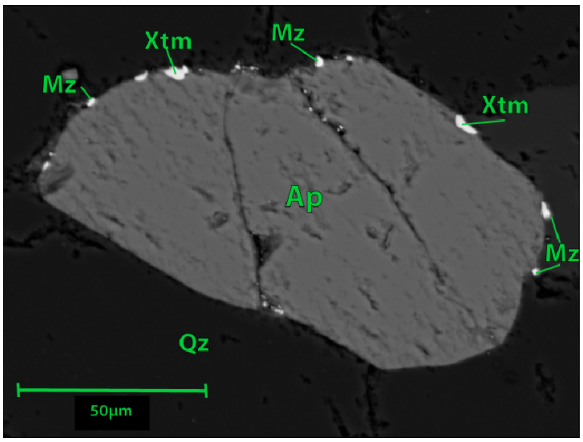

Figure 7.14: ST1118A – Apatite, xenotime, and high Ca-monazite

Apatite in the metapsammite is <100µm, with grain boundary monazite and xenotime. Monazite has a high-Ca signature. Matrix monazite is observed <75µm.

ST1118B - Metapelite

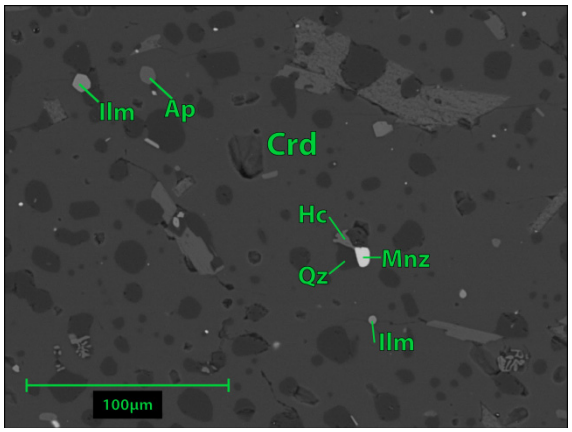

Figure 7.15: ST1118B – Monazite, apatite and ilmenite in cordierite

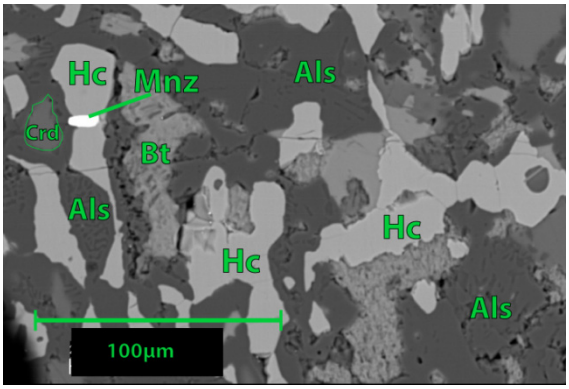

Figure 7.16: ST1118B – Matrix monazite

Monazite is commonly located as multiple inclusions in cordierite, <50µm. Xenotime is observed on apatite grain boundaries, within cordierite, but not as single grains.

7.2 Discussion

Monazite in this study was observed in all metamorphic grades, as inclusions or on grain boundaries of apatite and ilmenite, or as single grains within the matrix (Table 7.1). Xenotime is first observed at lower amphibolite grade, estimated temperature/pressure of 650°C at 2.7kbar (White *et al*., 2003), on grain boundaries of apatite and as inclusions in tourmaline. At high grades, xenotime was absent from the matrix but still present on apatite grain boundaries.

Within metapelites, monazite size and abundance increases with increasing metamorphic grade whilst apatite mode and size is observed to decrease due to increases with metamorphic grade. In metapsammites, apatite/monazites relationships are stable with monazite located as single grains and on rims of larger <250µm apatite grains, up to upper amphibolite grade. Corona or replacement textures around monazite, apatite or xenotime were not observed during in-situ analysis through the course of this study.

Scientific interest in the behaviour of the phosphate accessory minerals apatite, monazite and xenotime have resulted in a number of studies focusing on the determination of information that these accessory minerals hold regarding the reaction history of a rock through metamorphic processes, especially through trace element studies, for example coupled with garnet trace element zoning, and Th/Pb, U/Pb or Pb/Pb dating techniques (Spear and Pyle, 2002).

Williams, 2001 published a study on the response of detrital zircon and monazite to regional metamorphism and partial melting within the Cooma complex, in Southeastern Australia (Williams, 2001). The Cooma complex is very similar to the Mount Stafford area, in that it has a similar protolith of a turbidite sequence with metapelite/metapsammite layers, is relatively undeformed and has experienced high-temperature low-pressure (HPLT) metamorphism, for which exposure is accessible from low to high grade. Williams found that the breakdown of hydrous phases of REE and P bearing minerals at low metamorphic grades (≈200°C) can release REE and P into the system which allows for new monazite formation. At around 520-600°C new monazite starts to regrow, and was found to be

concentrated around biotite. With the melt remaining peraluminous, under 850°C and REE concentrations around the 100-350ppm level, monazite saturation was maintained (Williams, 2001).

Rubatto, *et al* (2001, 2006) investigated the behaviour of zircon and monazite at Mount Stafford, and in the nearby Reynolds Ranges, central Australia. Detailed geochronological determination of zircon and monazite grains and coupled with the investigation of trace element compositional domains aimed to link accessory phase growth with the overall mineral assemblage. It was found that metamorphic monazite was forming in Zone 2 at temperatures ≈650°C. The metamorphic Zone 2a, which is the lowest zone in this Honours research project, observed monazite ≈10µm on grain boundaries of apatite. It is noted that the studies of Rubatto *et al* (2001, 2006) was undertaken on monazite and zircon separates. Textural observation from the in-situ relationships between apatite and micro-monazite at low (greenschist) grades indicates the precipitation of metamorphic monazite at temperatures 25°C less than previously recorded for this site, although this is in within temperature range of the observed new growth of monazite from the Cooma Complex (Williams, 2001).

8 Investigation of Tourmaline

8.1 Introduction

This section describes the study of tourmaline grains from four pairs of representative thin sections from a transect of increasing grade from greenschist to upper amphibolite (Spring Creek Transect), Mount Stafford. The aims of this research are to develop criteria for the assessment of tourmaline geochemistry, and based on this criteria categorise changes in geochemistry of tourmaline between metamorphic zones of increasing grade from this study's samples.

8.2 Analytical Methodology

Petrographic and SEM-BSE images are used to provide a visual indication of the variations in size, form, colour and any internal chemical zoning within tourmaline grains from this study's representative thin sections. Electron microprobe (EMP) analysis is used for the classification of tourmaline and to identify chemical variations within grains via EMP transects. Normalisation procedures, classification and nomenclature of tourmaline follows (Henry *et al.*, 2011; Novák *et al.*, 2009).

The Al-Fe-Mg diagrams of Henry and Guidotti (1985) are used to relate tourmaline composition and source rocks in sedimentary and metamorphic environments (Henry and Dutrow, 1996; Henry and Guidotti, 1985). WinClastour v1.5 is a MicroSoft Visual Basic 6.0 program which allows for the calculation of tourmaline structural formulae from EMP data, following tourmaline nomenclature from Henry and Dutrow, 1996 (Yavuz *et al.*, 2006). Slight modifications were made during this study to output data to align nomenclature more closely with (Henry *et al.*, 2011). WinClastour v1.5 output data was graphed using Golden Software Grapher 10 (2013) (demo version). A new program, called WinTcac, is being developed to replace WinClastour and will reference the Henry *et al,* 2011 nomenclature. WinTcac is currently being reviewed for release (2013, Dr F. Yavuz, *personal communication.*).

8.3 Tourmaline Chemistry and Crystallography

The basic structural formula of tourmaline is:

$$\mathbf{XY_3Z_6(T_6O_{18})(BO_3)_3VW}$$

Where:
X = Ca, Na, K, or vacant
Y = Li^{1+}, Mn^{2+}, Mg^{2+}, Fe^{2+}, Al^{3+}, Cr^{3+}, V^{3+} Ti^{3+}, Fe^{3+}
Z = Al^{3+}, Cr^{3+}, Fe^{3+}, V^{3+}
T = Si^{4+} (minor Al^{3+})
B = B^{3+}
V = O^{2-}, OH^{1-}
W = F^{1-}, O^{2-} and/or OH^{1-}
(Novák *et al.*, 2009)

Tourmaline has 31 anions situation across eight sites in its structural formula, and is able to accommodate a wide range of major, minor and trace elements. The X-site is commonly occupied by

Na, and Ca with minor K, or can be vacant to some degree. The tetrahedral BO_3 groups in tourmaline form a major part of the structure, averaging 10% by oxide weight (Henry and Dutrow, 1996). The overall crystal structure is dominated by tetrahedral rings in the T site, normally occupied by Si with minor Al substitution, that have the apical oxygen aligned, creating a crystal (-c) pole (Henry and Dutrow, 1996). Tourmaline which forms under low to medium metamorphic grades can develop a compositional polarity at each pole of the c-axis. The +c pole (Fig 8.1) can preferentially incorporate Mg and Al, without changing Fe contents, which can result in different Mg/Fe ratios at each c-axis pole of tourmaline (Henry and Dutrow, 1996).

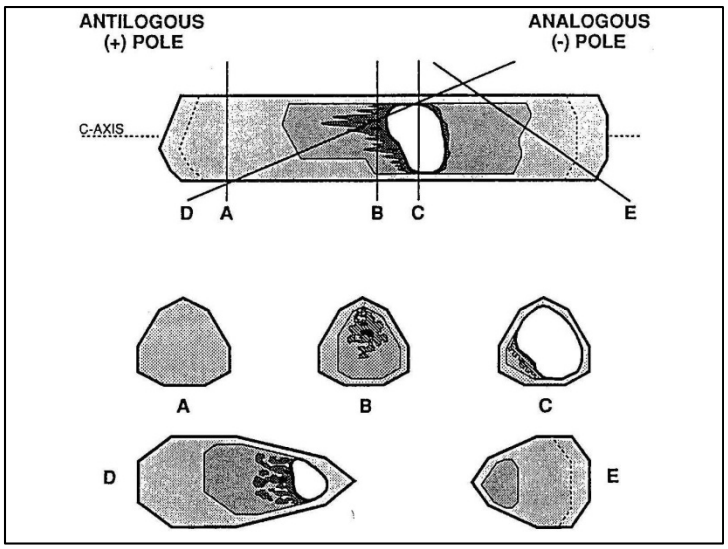

Figure 8.1: Schematic cross section of tourmaline retaining a detrital core, with three metamorphic growth zones (Henry and Dutrow, 1996)

8.4 Tourmaline Nomenclature and Classification

Tourmaline species are traditionally classified into two solid-solution series, the schorl-dravite series and the schorl-elbaite series, however there are also solid solutions between dravite-uvite, dravite-povandraite, elbaite-liddioatite, and other tourmaline end members (Henry and Dutrow, 1996).

The classification of tourmaline is dependent on the amount of analytical data available. Level 1 classification is based on complete analytical and structural data, Level 2 classification is applied when complete analytical data is available, including oxidation states of transition elements and data for light elements. Many tourmaline studies rely on classification based on incomplete data, such as that obtained through EMP analysis, and this is subject to Level 3 classification procedure (Henry *et al.*, 2011).

Normalisation procedures also vary depending on the level of data available. For Level 1 classification, it is based on 31 oxygens, Level 2 is 29 oxygens, and Level 3 is 24.5 oxygens. A full description of normalisation procedures can be found in Novak *et al*, 2009, Appendix A3.

Level 3 classification firstly orders cations and anions in order of relative site abundance (Table 8.1), and establishes the principle tourmaline subgroup by determining the X-site cation (Na, Ca+K) or vacancy. W-site (OH^{1-}, F^{1-} or O^{2-}) and V-site (O^{2-}, OH^{1-}) are established if anion data is available. The Z-site is predominantly Ai^{3+}. The assignment of the Y-site cation is a key factor in tourmaline classification, as demonstrated in Table 8.2 where it is shown to be the distinguishing feature in the

determination of elbaite, schorl and dravite. The Si^{4+} with (minor Al^{3+}) resides in the T-site, and the B-site contains B^{3+}.

Table 8.1: Relative site abundance of cations and anions in tourmaline-group minerals

Site	Relative abundance of ions with different valence states	Common cations and anions at each site in order of relative abundance
X	$R^{+} > R^{2+} > \square$ (vacancy)	$\underline{R^{+}}$: $*Na^{1+} >> K^{1+}$ $\underline{R^{2+}}$: Ca^{2+}
Y	$R^{2+} > R^{3+} > R^{+} > R^{4+}$	$\underline{R^{2+}}$: $Fe^{2+} \sim Mg^{2+} > Mn^{2+} >>> Zn^{2+}, Ni^{2+}, Co^{2+}, Cu^{2+}$ $\underline{R^{3+}}$: $Al^{3+} >> Fe^{3+} > Cr^{3+} >> V^{3+}$ $\underline{R^{+}}$: Li^{1+} $\underline{R^{4+}}$: Ti^{4+}
Z	$R^{3+} >> R^{2+}$	$\underline{R^{3+}}$: $Al^{3+} >> Fe^{3+} > Cr^{3+} > V^{3+}$ $\underline{R^{2+}}$: Mg^{2+}
T	$R^{4+} >> R^{3+}$	$\underline{R^{4+}}$: Si^{4+} $\underline{R^{3+}}$: $Al^{3+} > B^{3+}$
B	R^{3+}	$\underline{R^{3+}}$: B^{3+}
V	$S^{-} >> S^{2-}$	$\underline{S^{-}}$: OH^{1-} $\underline{S^{2-}}$: O^{2-}
W	$S^{-} \sim S^{2-}$	$\underline{S^{-}}$: $OH^{1-} \sim F^{1-}$ $\underline{S^{2-}}$: O^{2-}

(Novák *et al.*, 2009)

Table 8.2: Recommended names for Level 3 determined tourmalines

Alkali tourmaline subgroup

	(X)	(Y_3)	(Z_6)	V_3 likely	W unknown
Elbaitic tourmaline	Na	Li and Al	Al	(OH)	unknown
Schorlitic tourmaline	Na	Fe^{2+}	Al	(OH)	unknown
Dravitic tourmaline	Na	Mg	Al	(OH)	unknown
Buergeritic tourmaline	Na	Fe^{3+}	Al	(O)	unknown
Olenitic tourmaline	Na	Al	Al	(OH)	unknown
Povondraitic tourmaline	Na	Fe^{3+}	Fe^{3+}	(OH)	unknown
Chromium-dravitic tourmaline	Na	Mg	Cr	(OH)	unknown
Vanadium-dravitic tourmaline	Na	Mg	V	(OH)	unknown

Calcic Tourmaline Subgroup

	(X)	(Y_3)	(Z_6)	V_3 likely	W unknown
Liddicoatitic tourmaline	Ca	Li and Al	Al	(OH)	Unknown
Uvitic tourmaline	Ca	Mg	Al	(OH)	unknown
Feruvitic tourmaline	Ca	Fe^{2+}	Al	(OH)	unknown

From: (Novák *et al.*, 2009)

8.5 Analytical Strategy

Tourmaline grains from polished thin sections for this study's samples (ST1119, ST1005, ST1106, ST1118) were analysed using a petrographic microscope, observing colour, form, size, abundance, zoning and any other distinguishing features. Grains were photographed using a petrographic microscope, and imaged using scanning electron microscope backscatter electron (SEM-BSE) imaging to determine any internal zoning that may provide an indication to chemical variations within grains.

Electron microprobe (EMP) data was collected for tourmaline from all representative thin sections, and detailed transects were taken of selected tourmaline grains from ST1119 and ST1005. EMP laboratory conditions are outlined in Chapter 4, and EMP analytical data is presented in Appendices 13 and 14.

8.6 Analytical Results

EMP laboratory conditions are outlined in Chapter 4. EMP data was normalised to 24.5 oxygens. Full petrographic details of this study's samples are provided in Chapter 6, and a summary of tourmaline petrography is provided in this chapter. Figure 8.3 provides an overview of metamorphic conditions and key indicator minerals for this study. Transect labels are referenced to the electron microprobe (EMP) points, by circle number (ie: ST1119 C3).

Table 8.3: Sample site metamorphic conditions and key indicator minerals

Approx. Zone	Sample site	Rock type	Mineral Occurences (observed, +Qz)	Estimated T *	Estimated P *
2a	ST1119A	Subaluminous Metapelite	Kfs-And-Ms-Bt	≈625°C	≈2.5 kbar
	ST1119B	Metapsammite	Ms-Bt-Kfs		
2c	ST1005A	Metapelite	Crd-And-Sil-Kfs-Ms-Bt	≈650°C	≈2.7 kbar
	ST1005B	Subaluminous Metapelite	Crd-And-Sil-Kfs-Ms-Bt		
3	ST1106A	Subaluminous Metapelite	Crd-Sil-Kfs-Bt	≈650-680°C	≈2.8-3.3 kbar
	ST1106A	Metapsammite	Kfs-Sil-Bt		
	ST1106D	Metapelite	Crd-Sil-Kfs-Bt-Spl		
3	ST1118A	Metapsammite	Crd-Sil-Kfs-Grt-Pl-Bt	≈740 deg°C	>3.0 kbar
	ST1118B	Metapelite	Crd-Sil-Kfs-Bt-Spl		

* White *et al (* 2003) - Calculated temperature and pressure estimates for different metamorphic zones at Mount Stafford

ST1119A – Subaluminous Metapelite

Sample ST1119 represents a subaluminous metapelite / metapsammite pair which reached estimated metamorphic conditions of 2.5kbar at 625°C, which is below the metapelite solidus (White *et al.*, 2003).

Tourmaline is present in thin section as either yellow-blue grains with yellow rims, or as small (≈50µm) yellow grains. Tourmaline grains are subhedral to euhedral, and sizes range from 0.03mm to 0.5mm. Zoning is observed in core-rim relationships, commonly with the rims containing fine quartz inclusions. Tourmaline mode is estimated at 4.3 ±2%. Eleven core and rim analyses from ST1119A was plotted on a Al-Mg-$Fe_{(tot)}$ ternary diagram, which displays distinct regions that define tourmalines from different rock types (Fig: 8.3) (Henry and Guidotti, 1985). ST1119A displayed tourmaline within the schorl-dravite series, sourced from two different rock types: 1) within Li-poor granitoid and associated pegmatites and aplites, and 2) metapelites and metapsammites coexisting with an Al-saturating phase. To more closely investigate this relationship, EMP transects were undertaken on two representative tourmaline grains from ST1119A.

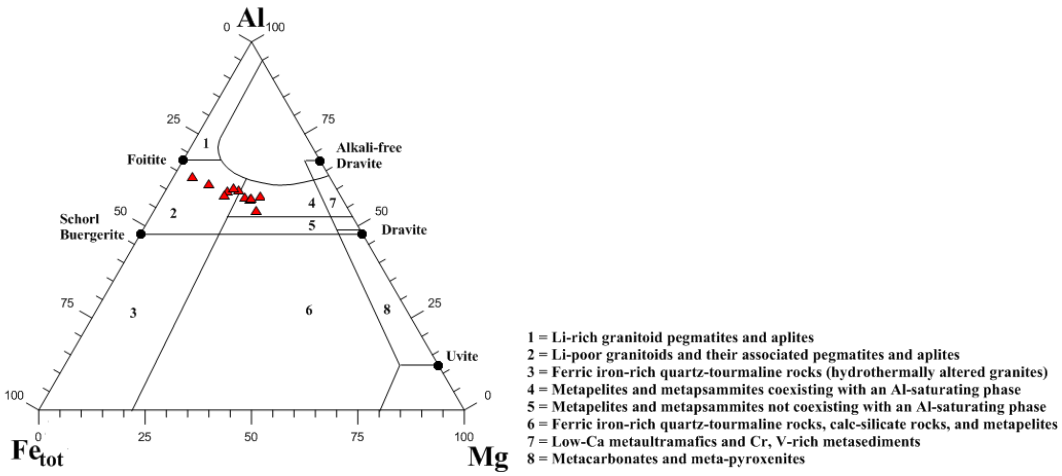

Figure 8.2: ST1119A - Al-$Fe_{(tot)}$-Mg diagram showing a range of tourmaline formation environments across the schorl-dravite series

The transect grains from ST1119A were selected based on observed core-rim relationships in microphotograph and SEM-BSE images. Tourmaline grain ST1119A C3 is approximately 0.5mm and shows a lighter yellow-blue core surrounded by a darker yellow rim (Fig: 8.3). The core-rim relationship is evident under BSE, and has been highlighted in the BSE image for reference (Fig: 8.4).

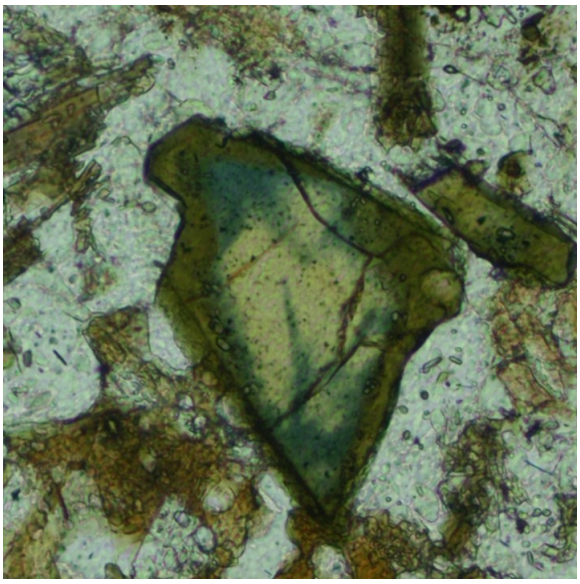

Figure 8.3: ST1119A C3 - Microphotograph of Tourmaline (ppl)

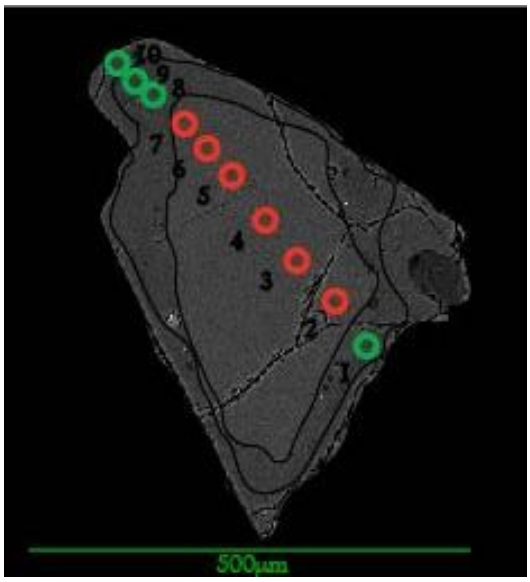

Figure 8.4: ST1119A C3 - SEM-BSE Image of tourmaline showing EMP transect points

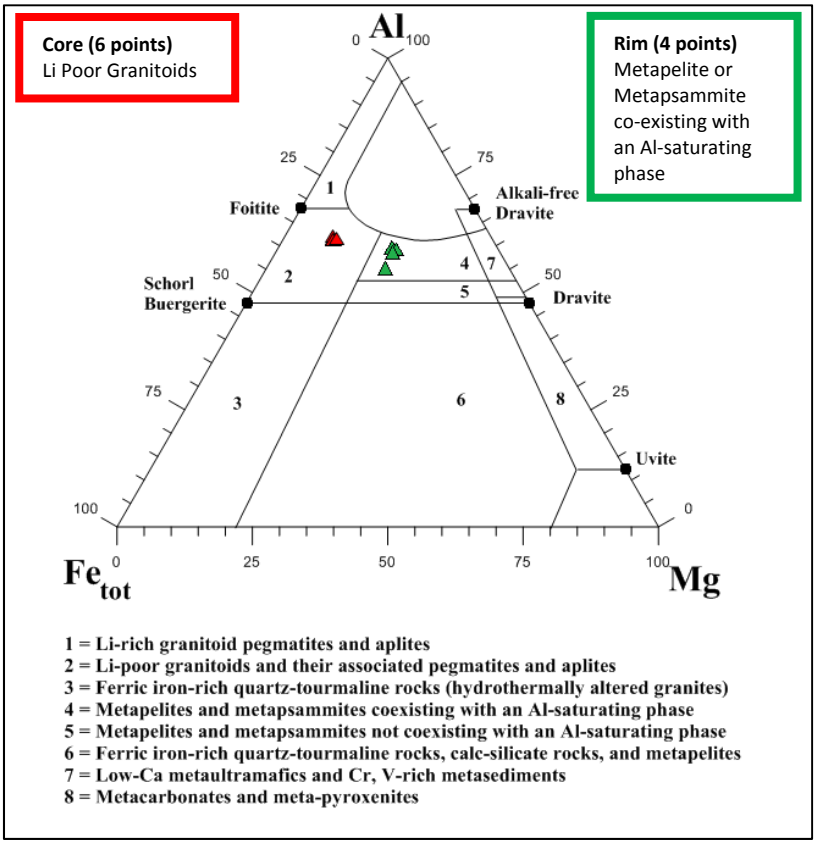

Figure 8.5: ST1119A C3 - Al-Fe$_{(tot)}$-Mg diagram for a tourmaline core-rim transact displaying variations in tourmaline formation and type

The second ST1119A tourmaline grain chosen for transect was euhedral ≈250µm and dark yellow (Fig: 8.6). A possible remnant core was observed in SEM-BSE and the transect points were aligned to sample this area (Fig: 8.7).

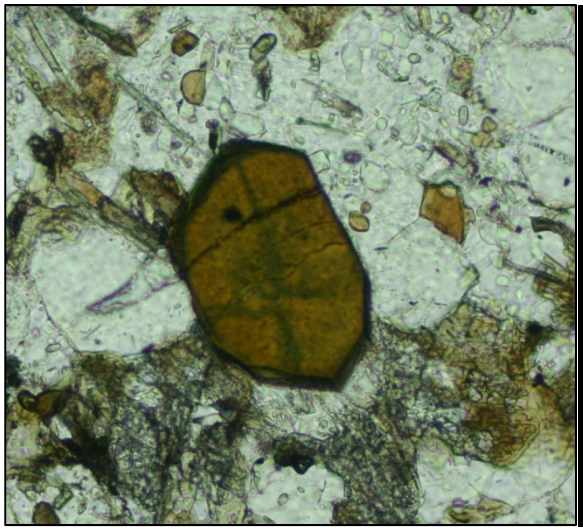

Figure 8.6: ST1119A C2 - Tourmaline (ppl)

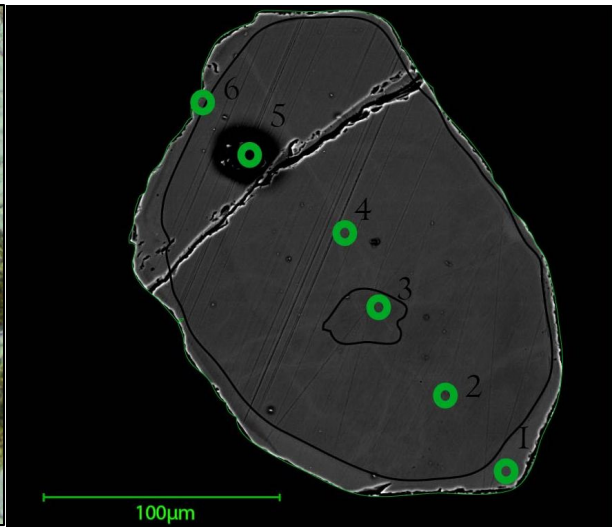

Figure 8.7: ST1119A C2 - SEM-BSE Image of tourmaline showing EMP transect points

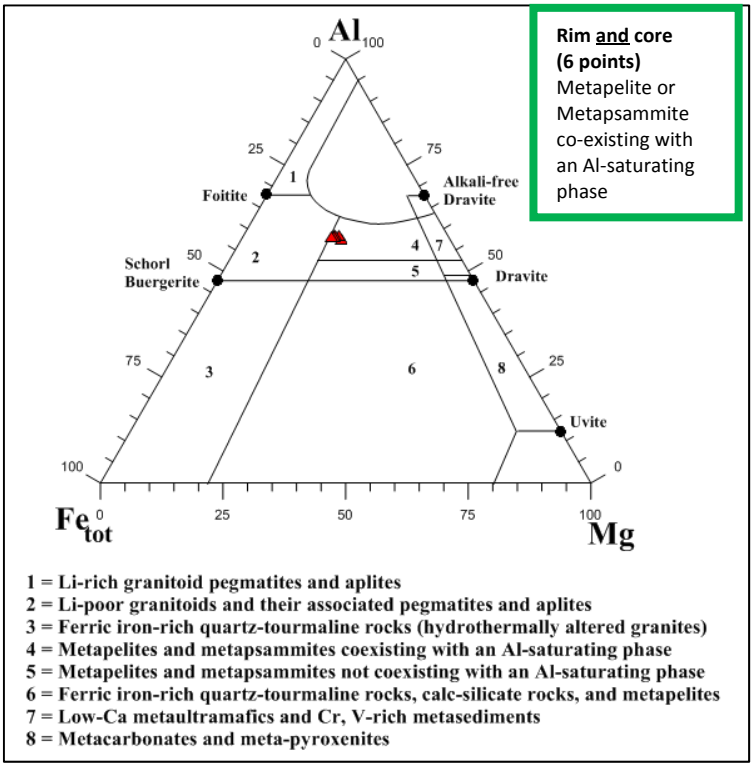

Figure 8.8: ST1119A C2 - Al-Fe$_{(tot)}$-Mg diagram for a tourmaline core-rim transact Indicating that tourmaline formed in a single rock type

Grain ST1119A C2 was found to be within the schorl-dravite series, and formed from a metapelite / metapsammite coexisting with an Al-saturating phase. There was no chemical variation distinguishing a core-rim relationship.

ST1119B - Metapsammite

Tourmaline in thin section from sample ST1119B displays a similar morphology to tourmaline from ST1119A, with zoned and unzoned <0.5mm grains, and a mode of 3.2 ±2.8%. Nine analyses were taken of core and rim points for the greenschist grade metapsammite (ST1119B), which are plotted in Figure 8.9. Tourmaline grains are indicated to be from three separate rock types: 1) Li-poor granitoid and associated pegmatites and aplites, 2) metapelites and metapsammites coexisting with an Al-saturating phase, and 3) metapelites and metapsammites not coexisting with an Al-saturating phase.

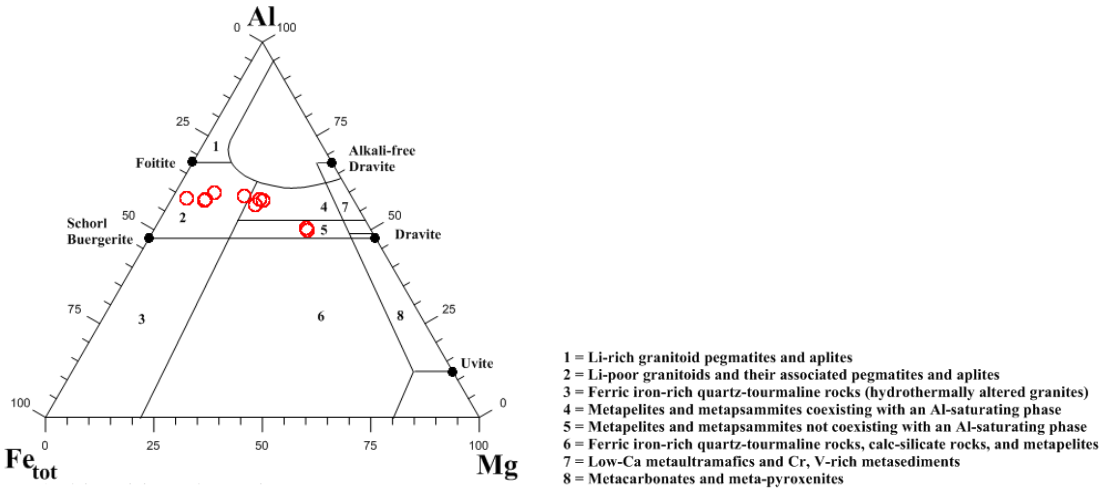

Figure 8.9: ST1119B - Al-Fe$_{(tot)}$-Mg diagram

A transect was undertaken on a representative tourmaline grain from ST1119B, which did not appear to have any core-rim zoning under ppl (Fig: 8.10), however did show rim zonation under BSE imaging (Fig: 8.11).

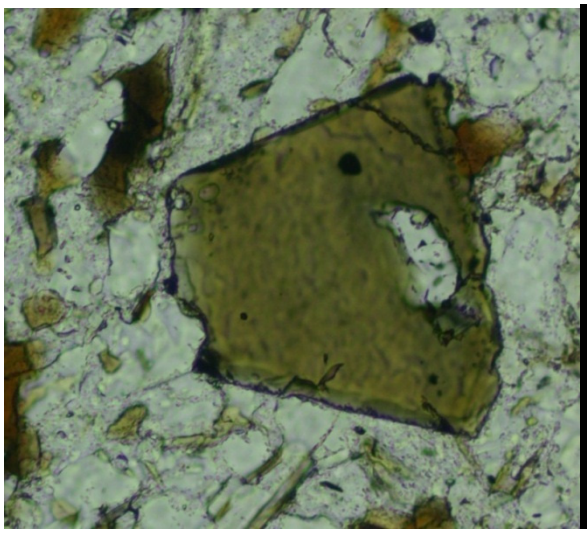

Figure 8.10: ST1119B C1 - Tourmaline (ppl)

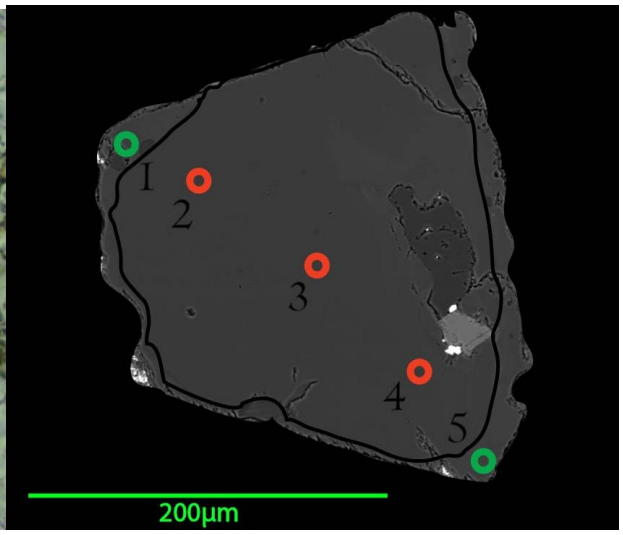

Figure 8.11: ST1119B C1 – SEM-BSE Image of tourmaline showing EMP transect points

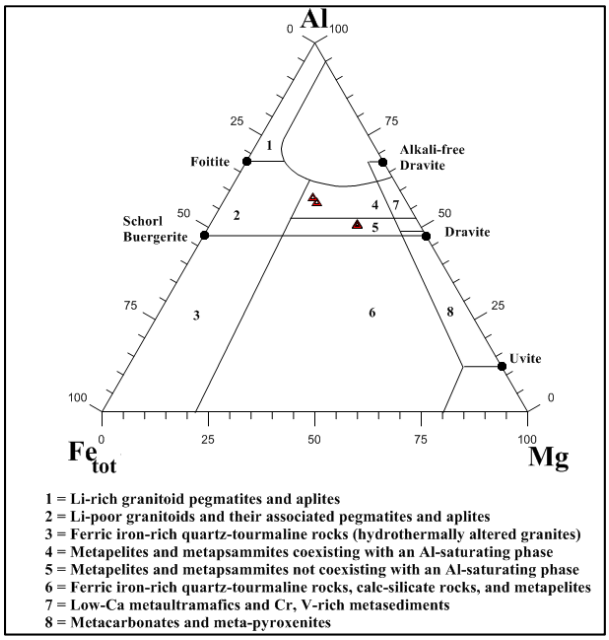

Figure 8.12: ST1119B C1 - Al-Fe$_{(tot)}$-Mg diagram for a tourmaline core-rim transact Indicating that tourmaline formed in different rock types

Transect results from ST1119B showed that a chemically distinguishable core sourced from a metapelite /metapsammite not coexisting with a Al-saturating phase was rimmed by metamorphic tourmaline coexisting with an Al-saturated phase. Core and rim tourmaline compositions for sample ST1119 have been summarised in figure 8.13.

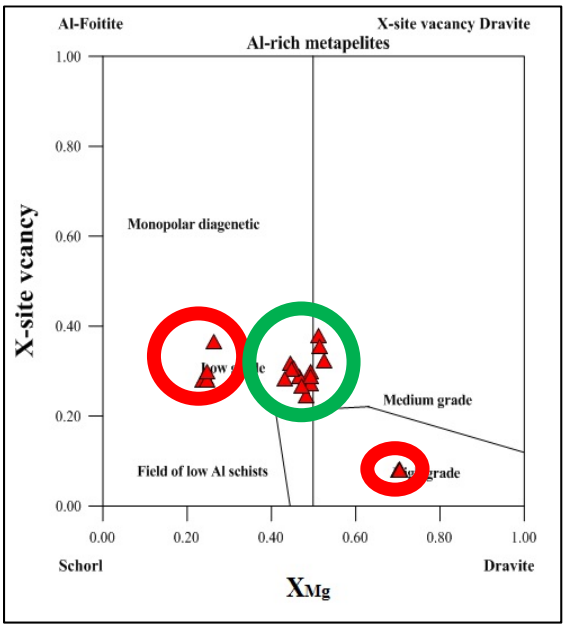

Figure 8.13: ST1119 - Summary of core-rim formation environments Green circle: rim and whole grain. Red circle: core

The high grade core recorded fell into field 2, and indicates detritus from an Li-poor granitoid (Henry and Guidotti, 1985). The low grade cores (field 5) may be sourced from carbonate bearing metapelite or metapsammite, with rim and whole grains at medium grade formed in pelitic schist co-existing with Mg phase and Al phase (Henry and Guidotti, 1985).

ST1005A - Metapelite

At estimated metamorphic conditions of 650°C and 2.7 kbar, both the metapelite (ST1005A) and subaluminous metapelite (ST1005B) show indications of partial melting (Greenfield *et al.*, 1998;

White *et al.*, 2003). Tourmaline observed in ST1005A displays an increase of up to ≈10% modal abundance in thin section, and an increase in grain size. Tourmaline forms large yellow-blue subhedral cracked idioblastic grains up to 3mm (8.14).

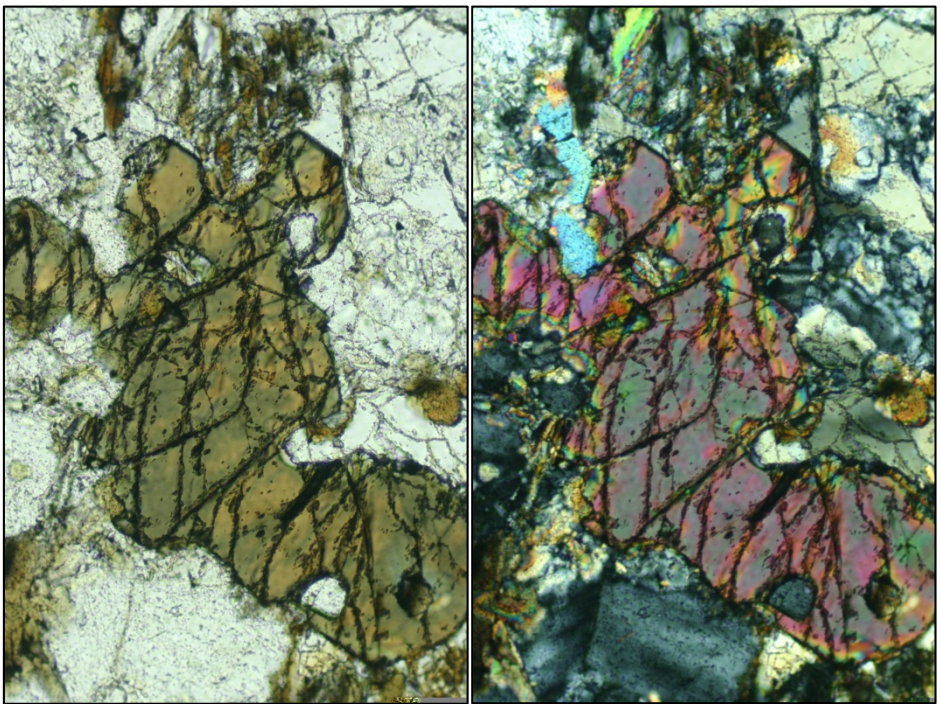

Figure 8.14: ST1005A – Representative tourmaline (ppl, xpl)
Base of photograph: 1mm.

A transect was undertaken along the c-axis on a representative tourmaline grain from ST1005A (Fig: 8.15 and 8.16).

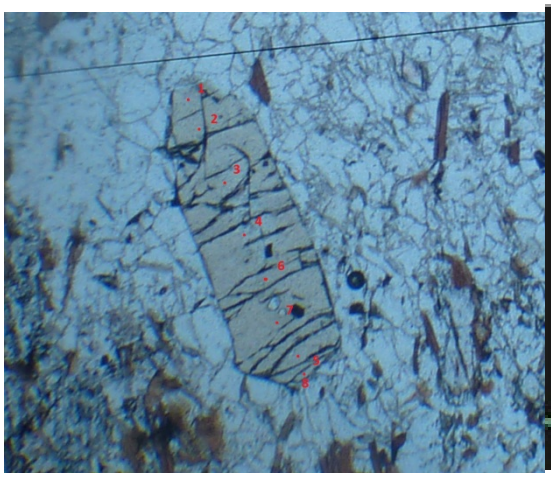

Figure 8.15: ST1005A C1 - Tourmaline (ppl)

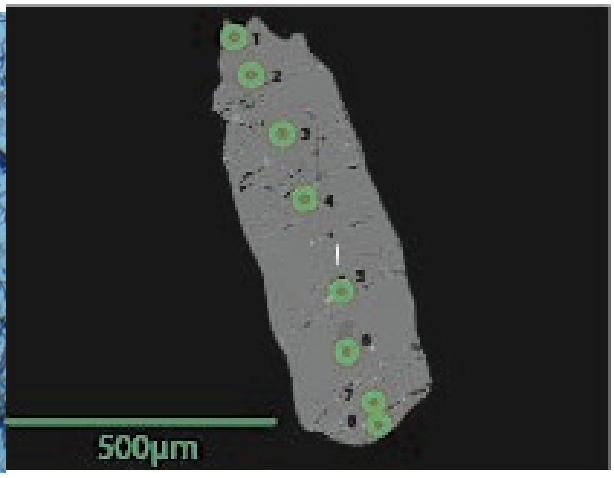

Figure 8.16: ST1005A C1 – SEM-BSE Image of tourmaline showing EMP transect points

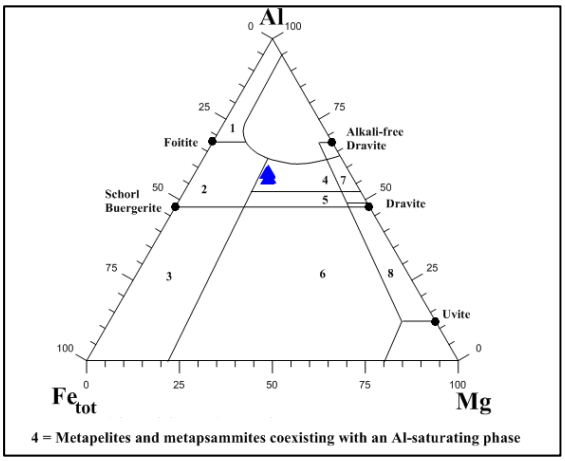

Figure 8.17: ST1005A C1 - Al-Fe$_{(tot)}$-Mg diagram for transect

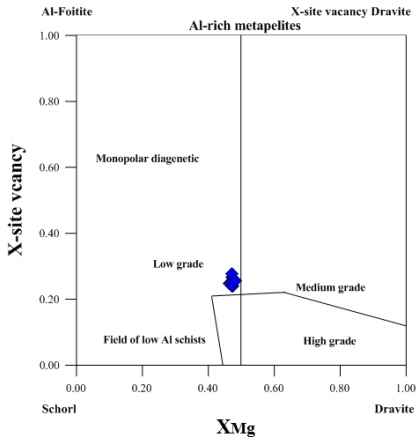

Figure 8.18: ST1005A C1 – Low grade metamorphic tourmaline

When plotted up on a Al-Fe$_{(tot)}$-Mg diagram, and against an indication of grade (Fig: 8.17 and 8.18) ST1005A C1 was found to be schorl-dravite low grade metamorphic tourmaline.

ST1005B – Subaluminous Metapelite

In contrast to the metapelite at the same grade (ST1005A), tourmaline grains in ST1005B were small <0.2mm, bright blue, and modal proportions 3.2 ±2.8% (8.19). Tourmaline has a skeletal form with quartz intergrowths, and is commonly enclosed in biotite and is observed to form rims around biotite crystalloblasts. A transect was undertaken on one small grain (Fig: 8.20).

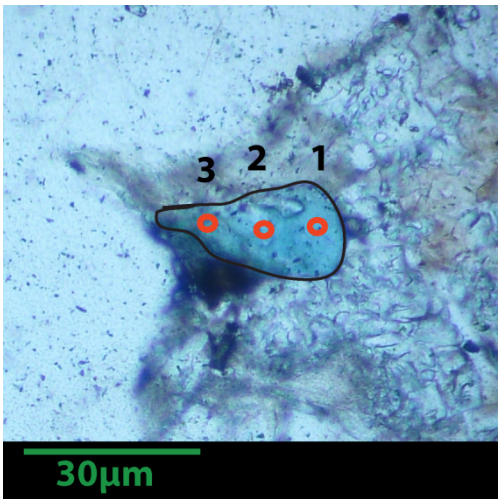

Figure 8.19: ST1005B C5 – Representative tourmaline grain transect

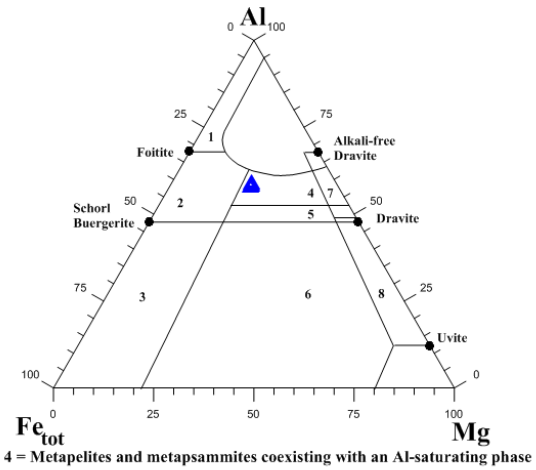

Figure 8.20: ST1005B C5 – Al-Fe$_{(tot)}$-Mg diagram for transect

ST1106A – Subaluminous Metapelite, & Metapsammite

Sample ST1106 was taken from an outcrop of a schileren migmatite. Estimated metamorphic conditions were ≈650-680°C and ≈2.9-3.3 kbar (White *et al.*, 2003). The thin section for ST1106A has two distinct zones with contracting bulk rock composition: metapelite and metapsammite. The form of tourmaline in the subaluminous metapelite is interstitial grains, up to 0.5mm commonly within fine grained pinnite along cordierite grain boundaries, in modal proportions of 2.0 ±0.5 %. Tourmaline in the metapsammite portion of the thin section was occasional bright blue tourmaline

grains with quartz inclusions. Analysis focused on the subaluminous metapelite portion of the thin section.

8.7 ST1106D - Metapelite

Tourmaline form in ST11106D is very similar to the subaluminous metapelite section on ST1116A. Toumrline is blue-yellow, anhedral and commonly located with pinite along grain boundaries of cordierite, up to modal proportions of 2.0 ±0.5% (Fig: 8:21). Eleven points were analysed, and are plotted in Figures 8.22 and 8.23. There is an indication of metamorphic grade increase, as evident from the data set crossing the low/medium line in Figure 8.23.

Figure 8.21: ST1106D – Tourmaline (ppl), showing point analysis locations (red spots) Base of photograph is ≈200µm

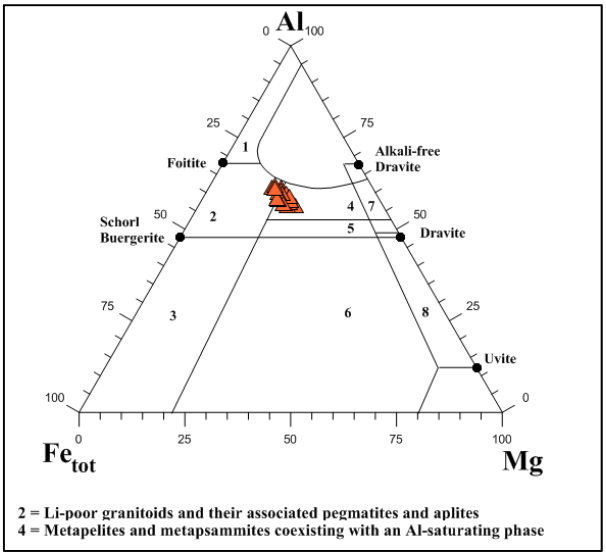

Figure 8.22: ST1106D – Al-Fe$_{(tot)}$-Mg diagram

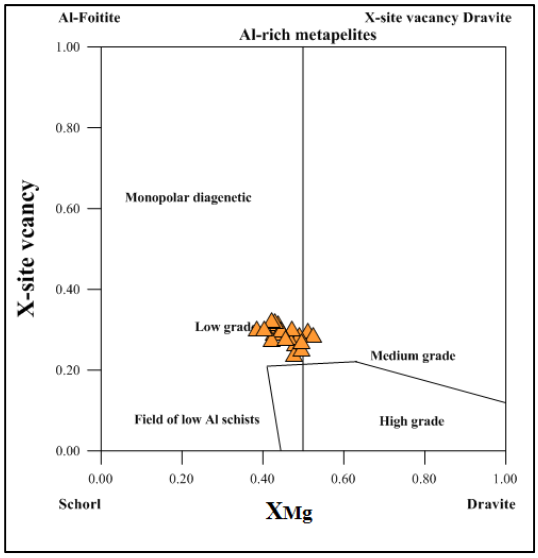

Figure 8.23: ST1106D – Tourmaline grade

ST1118A - Metapsammite

Site ST1118 contains the highest grade rocks examined in this study, and are estimated to be at peak conditions of ≈780°C and >3.0 kbar (White *et al.*, 2003).

In metapsammite sample ST1118A, tourmaline was not observed.

ST1118B - Metapelite

Tourmaline present was present in low modal proportions 0.1 ±0.1%, commonly as small bright blue <0.1mm inclusions in cordierite. When analysed, tourmaline fell within the range of high-grade metamorphic metapelites coexisting with an Al-saturating phase (Fig: 8.24 and 8.25).

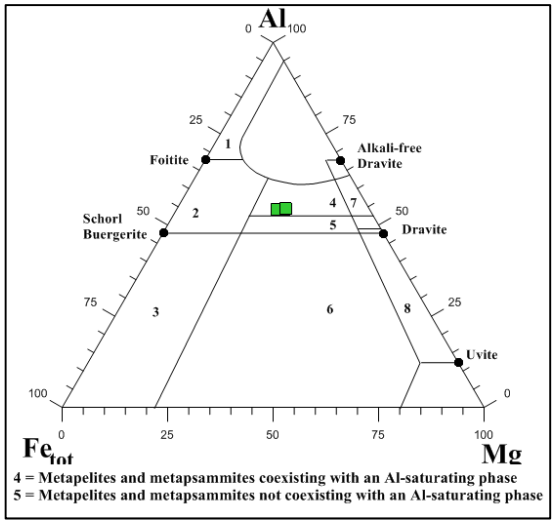

Figure 8.24: ST1118B - Al-Fe$_{(tot)}$-Mg diagram

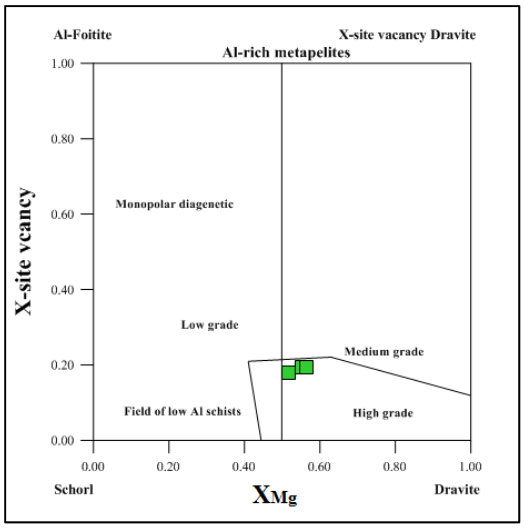

Figure 8.25: ST1118B – Tourmaline grade

8.8 Discussion

Studies on tourmaline from igneous, hydrothermal, and metamorphic systems have shown it to be a valuable petrographic indicator mineral. Tourmaline is ubiquitous in a range of environments and is extremely chemically and mechanically stable once formed. Its sensitivity to system changes during formation results in the storage of a diverse range of chemical, textural and isotopic information during growth (Henry and Dutrow, 1996).

8.8.1 Tourmaline development - Closed-System

Tourmaline development depends fundamentally on the availability of boron. During closed system behaviour of B during metamorphism, B is derived from minerals found locally within the rock system (Henry and Dutrow, 1996). For B to be retained in the rock, there must be a B-host (ie: muscovite, clay minerals) or a B stable mineral (ie: tourmaline), else B loss can occur. B released from the breakdown of B-host minerals can therefore become available for the formation of tourmaline (Henry and Dutrow, 1996).

At low metamorphic grades, the breakdown of clay minerals can be a significant release of B toward tourmaline production. This can be observed by overgrowths on detrital tourmaline cores (Henry and Dutrow, 1996). If B is released slowly from B-host minerals such as muscovite, the resultant tourmaline growth pattern will exhibit chemical zonation which is consistent with continuous breakdown reactions that are ultimately muscovite-consuming. If muscovite is a reactant in a discontinuous reaction, a large proportion of B is released as muscovite is consumed relatively quickly. Any pre-existing tourmaline grains will therefore be more likely to form thicker, unzoned or weakly zoned overgrowths (Henry and Dutrow, 1996).

8.8.2 Tourmaline Development - Open-System

Dehydration melting reactions or the input of hydrothermal fluids in low temperature metamorphic rocks >150°C can result in leaching of B as it is strongly partitioning into fluid phases. Infiltration of B-rich fluids can produce tourmaline development and distinct chemical and textural features which can be used to identify whether B introduction has occurred. Care needs to be taken when identifying whether a high concentration of tourmaline is due to the influence of external B sources, as, noted above, B enrichment can be influenced by in-situ reactions of B source minerals (ie: muscovite) (Henry and Dutrow, 1996).

8.8.3 Tourmaline stability study

Figure 8.26 shows a compilation by Hinsberg *et al*, 2011 of publicised tourmaline stability estimates. Of relevance to this study are point 3, stability of schorl, and points for 8 which is sourced from a tourmaline stability experiment using samples from Mount Stafford (Spicer *et al.*, 2004). Estimated temperature and pressure for this study's sample sites are in the range of 625-740°C, and 2.5-3.2kbar (White *et al.*, 2003), which encompasses the tourmaline stability estimate for schorl (point 3) but falls short of laboratory behaviour of natural tourmaline samples from Mount Stafford which were unstable between 840-870°C. This would provide an indication that tourmaline from this study's samples would be expected to be stable at greenschist and lower amphibolite grade.

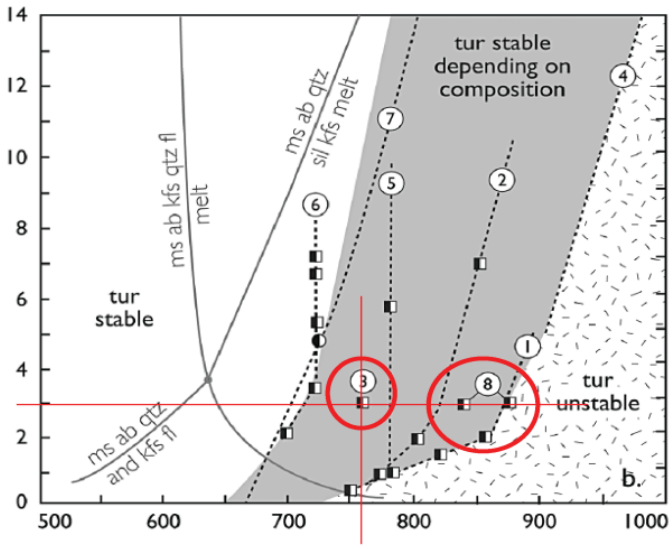

Figure 8.26: T/P Stability estimates for schorl, and for natural tourmaline sourced from Mount Stafford (van Hinsberg *et al.*, 2011)

8.9 Conclusion

Tourmaline formation in the lower (greenschist) grades at Mount Stafford has been found to be a result of closed system behaviour of fluids due to the break down of B-host minerals (clay minerals, mica) and formation of metamorphic tourmaline rims on detrital cores (ST1119A and ST1119B). The formation of up to 3mm unzoned euhedral tourmaline grains in metapelite (ST1005A) is considered to be related to the rapid consumption of muscovite (Henry and Dutrow, 1996). Mode and form of tourmaline reduces up-grade, as subhedral grains along mineral boundaries (ST1106). At highest grade (ST1118), tourmaline is absent from metapsammite, and evident as small grains within cordierite which indicates B loss via fluid movement at higher metamorphic grades.

9 Research Conclusion

The interbedded metapelites and metapsammites of the Mount Stafford Beds preserve a suite of metamorphic isograds and progressive evolution of migmatite morphology as a result of a steep lateral geothermal gradient of 75°C / km across a 10 km wide regional aureole (Vernon *et al.*, 1990). The migmatite banding at Mount Stafford is controlled by the interbedded turbidite protolith, rather than differentiation due to leucosome/melanosome segregation (Rubatto *et al.*, 2006) (& this study). The melting history at Mount Stafford has been found to be controlled by a series of biotite breakdown reactions, at different P/T conditions and contrasting whole rock . Melt mobilisation is limited across wide areas, which is confirmed by the constant bulk rock composition of metapelites and metapsammites across the area (Greenfield *et al.*, 1998; Rubatto *et al.*, 2006; White *et al.*, 2003)

The metamorphic Zone 2a, which is the lowest zone in this Honours research project, observed monazite ≈10µm on grain boundaries of apatite. It is noted that the studies of Rubatto *et al* (2001, 2006) was undertaken on monazite and zircon separates. Textural observation from the in-situ relationships between apatite and micro-monazite at low (greenschist) grades indicates the precipitation of metamorphic monazite at temperatures 25°C less than previously recorded for this site, although this is in within temperature range of the observed new growth of monazite from the Cooma Complex (Williams, 2001).

Tourmaline formation in the lower (greenschist) grades at Mount Stafford has been found to be a result of closed system behaviour of fluids due to the breakdown of B-host minerals (clay minerals, mica) and formation of metamorphic tourmaline rims on detrital cores (ST1119A and ST1119B). The formation of up to 3mm unzoned euhedral tourmaline grains in metapelite (ST1005A) is considered to be related to the rapid consumption of muscovite . Mode and form of tourmaline reduces up-grade, as subhedral grains along mineral boundaries (ST1106). At highest grade (ST1118), tourmaline is absent from metapsammite, and evident as small grains within cordierite which indicates B loss via fluid movement at higher metamorphic grades.

9.1 Further work

The utilisation of tourmaline as a key indicator mineral should be definitely be encouraged, hopefully be regarded as common to petrologic and fluid studies, as zircon and monazite are regarded in U/Pb and trace element studies. The primary restriction on the investigation of tourmaline in petrologic studies is the understanding of it compositional complexity. This has long been recognised, and studies are building on the methodology database, for example through the key paper by Henry and Guidotti (1985), importance of major element composition, sector zoning and fluid/melt composition (Marks *et al.*, 2013), evaluation on the controls of tourmaline in granitic, hydrothermal, and metapelitic systems (Göd *et al.*, 2010; Pesquera *et al.*, 2013; Pirajno and Smithies, 1992), and trace element partitioning and isotope fractionation of boron between white mica and tourmaline (Klemme *et al.*, 2011).

The pending release of the software program WinTcac (2013, Dr F. Yavuz, *personal communication*) is anticipated to be of great benefit in the normalisation of tourmaline, and in graphing tourmaline

relationships. The interface between WinClastour and Grapher 10.0 currently is highly problematic due to versioning issues.

Tourmaline is a sensitive monitor of the trace element composition of fluids (Klemme *et al.*, 2011; Marks *et al.*, 2013). Further work on tourmaline at Mount Stafford could include investigation of trace element and isotope partitioning between muscovite and tourmaline, and include some of the higher grade samples available. Analysis on tourmaline separates would be encouraged, as this would allow observation of the grain form, and the section which is being analysised (ie: a-, b- or c-axis, or oblique to these).

In-situ monazite dating, and more detailed investigation of monazite and xenotime internal structures would provide more information to assist in identifying multiple generations of monazite and relationships between accessory minerals.

10 References

Augustithis, S. S. (1990). Atlas of Metamorphic-Metasomatic Textures and Processes. Elsevier Science Publishers B.V., Amsterdam, The Netherlands.

Brown, M. (1973). The definition of metatexis, diatexis and migmatite. *Proceedings of the Geologists' Association*. Vol. 84, No. Part 4, pp. 371-382, IN371-IN372.

Buick, I. S., Hand, M., Vry, J., Cartwright, I., and Read, C. (1999). Polymetamorphism and reactivation of the Reynolds Range area, northern Arunta Inlier, central Australia : petrological, geochronological, geochemical and structural constraints. Field Guide No. 2. *Geological Society of Australia. Specialist Group in Geochemistry, Mineralogy, and Petrology.*

Claoué-Long, J., Edgoose, C., and Worden, K. (2008a). A correlation of Aileron Province stratigraphy in central Australia. *Precambrian Research*. Vol. 166, No. 1-4, pp. 230-245.

Claoué-Long, J., Maidment, D., and Donnellan, N. (2008b). Stratigraphic timing constraints in the Davenport Province, central Australia: A basis for Palaeoproterozoic correlations. *Precambrian Research*. Vol. 166, No. 1-4, pp. 204-218.

Claoué-Long, J. C., and Hoatson, D. M. (2005). Proterozoic mafic-ultramafic intrusions in the Arunta Region, central Australia: Part 2: Event chronology and regional correlations. *Precambrian Research*. Vol. 142, No. 3-4, pp. 134-158.

Collins, W. J., and Shaw, R. D. (1995). Geochronological constraints on orogenic events in the Arunta Inlier: a review. *Precambrian Research*. Vol. 71, No. 1-4, pp. 315-346.

Collins, W. J., and Vernon, R. H. (1991). Orogeny associated with anticlockwise P-T-t paths; evidence from low-P, high-T metamorphic terranes in the Arunta Inlier, central Australia. *Geology (Boulder)*. Vol. 19, No. 8, pp. 835-835-838.

Collins, W. J., Vernon, R. H., and Clarke, G. L. (1991). Discrete proterozoic structural terranes associated with low-P, high-T metamorphism, Anmatjira Range, Arunta Inlier, central Australia: tectonic implications. *Journal of Structural Geology*. Vol. 13, No. 10, pp. 1157-1171.

Deer, W. A., Howie, R. A., and Zussman, J. (1992). An introduction to the rock-forming minerals. 2nd Edition. Longman Group UK Limited, Harlow, Essex, England.

Farrow, K. (2012). Petrographic and Geochronological Investigation of S-Type Granites from a Low-Pressure High-Temperature Regional Aureole: Mount Stafford, Central AustraliaHonours Thesis]: Macquarie University.

Göd, R., Heiss, G., and Koller, F. (2010). Geochemistry of Metapelite Hosted Tourmalinites, Eastern Alps, Austria. *Jahrbuch der Geologischen Bundesanstalt* Vol. 150, pp. 325-3341.

Greenfield, J. E., Clarke, G. L., Bland, M., and Clark, D. J. (1996). In-situ migmatite and hybrid diatexite at Mt Stafford, central Australia. *Journal of Metamorphic Geology*. Vol. 14, No. 4, pp. 413-426.

Greenfield, J. E., Clarke, G. L., and White, R. W. (1998). A sequence of partial melting reactions at Mt Stafford, central Australia. *Journal of Metamorphic Geology*. Vol. 16, No. 3, pp. 363-378.

Henry, D. J., and Dutrow, B. L. (1996). Metamorphic tourmaline and its petrologic applications. *Reviews in Mineralogy and Geochemistry*. Vol. 33, No. 1, pp. 503-557.

Henry, D. J., and Guidotti, C. V. (1985). Tourmaline as a petrogenetic indicator mineral- An example from the staurolite-grade metapelites of NW Maine. *American Mineralogist*. Vol. 70, No. 1-2, pp. 1-15.

Henry, D. J., Novák, M., Hawthorne, F. C., Ertl, A., Dutrow, B. L., Uher, P., and Pezzotta, F. (2011). Nomenclature of the tourmaline-supergroup minerals. *American Mineralogist*. Vol. 96, No. 5-6, pp. 895-913.

Hughes, J. M., and Rakovan, J. (2002). The Crystal Structure of Apatite, $Ca_5(PO_4)_3(F,OH,Cl)$. *in* Kohn, M. J., Rakovan, J., and Hughes, J. M., eds., *Phosphates: Geochemical, Geobiological, and Materials Importance*, Volume 48. Washington, DC, Mineralogical Society of America, pp. 1-12.

Klemme, S., Marschall, H. R., Jacob, D. E., Prowatke, S., and Ludwig, T. (2011). Trace-element partitioning and boron isotope fractionation between white mica and tourmaline. *The Canadian Mineralogist*. Vol. 49, No. 1, pp. 165-176.

Li, X.-H., Li, Z.-X., Wingate, M. T. D., Chung, S.-L., Liu, Y., Lin, G.-C., and Li, W.-X. (2006). Geochemistry of the 755Ma Mundine Well dyke swarm, northwestern Australia: Part of a Neoproterozoic mantle superplume beneath Rodinia? *Precambrian Research*. Vol. 146, No. 1–2, pp. 1-15.

MacKenzie, W. S., and Guilford, C. (1980). Atlas of rock-forming minerals in thin section. Longman Group Limited, Essex, United Kingdom.

Marks, M. A. W., Marschall, H. R., Schühle, P., Guth, A., Wenzel, T., Jacob, D. E., Barth, M., and Markl, G. (2013). Trace element systematics of tourmaline in pegmatitic and hydrothermal systems from the Variscan Schwarzwald (Germany): The importance of major element composition, sector zoning, and fluid or melt composition. *Chemical Geology*. Vol. 344, No. 0, pp. 73-90.

Novák, M., Henry, D., Hawthorne, F. C., Ertl, A., Uher, P., Dutrow, B., and Pezzotta, F. (2009). Nomenclature of the tourmaline-group minerals. *Report of the Subcommittee on Tourmaline Nomenclature to the International Mineralogical Association's Commission on New Minerals, Nomenclature and Classification*.

Ondrejka, M., Uher, P., Putiš, M., Broska, I., Bačík, P., Konečný, P., and Schmiedt, I. (2012). Two-stage breakdown of monazite by post-magmatic and metamorphic fluids: An example from the Veporic orthogneiss, Western Carpathians, Slovakia. *Lithos*. Vol. 142–143, No. 0, pp. 245-255.

Pesquera, A., Torres-Ruiz, J., García-Casco, A., and Gil-Crespo, P. P. (2013). Evaluating the Controls on Tourmaline Formation in Granitic Systems: a Case Study on Peraluminous Granites from the Central Iberian Zone (CIZ), Western Spain. *Journal of Petrology*. Vol. 54, No. 3, pp. 609-634.

Pirajno, F., and Smithies, R. H. (1992). The FeO/(FeO+MgO) ratio of tourmaline: A useful indicator of spatial variations in granite-related hydrothermal mineral deposits. *Journal of Geochemical Exploration*. Vol. 42, No. 2–3, pp. 371-381.

Potts, P. J. (1987). A Handbook of Silicate Rock Analysis. Blackie & Son Limited, United Kingdom.

Pyle, J. M., and Spear, F. S. (2003). Yttrium zoning in garnet: Coupling of major and accessory phases during metamorphic reactions. *American Mineralogist*. Vol. 88, No. 4, pp. 708.

Research Services Branch, National Institute of Mental Health, Bethesda, Maryland, USA. . *ImageJ. Public domain Java image processing program.* (2012) [http://rsbweb.nih.gov/ij/index.html]

Rubatto, D., Hermann, J., and Buick, I. S. (2006). Temperature and bulk composition control on the growth of monazite and zircon during low-pressure anatexis (Mount Stafford, central Australia). *Journal of Petrology*. Vol. 47, No. 10, pp. 1973-1996.

Sawyer, E. W. (2008). Working with Migmatites: Nomenclature for the Constituent Parts. *in* Sawyer, E. W., and Brown, M., eds., Working with Migmatites, Volume 38, Mineralogical Association of Canada Short Course, p. 1-28.

Shelley, D. (1997). Igneous and metamorphic rocks under the microscope. Chapman & Hall, London, United Kingdom.

Spear, F. S., and Pyle, J. M. (2002). Apatite, Monazite, and Xenotime in Metamorphic Rocks. *in* Kohn, M. J., Rakovan, J., and Hughes, J. M., eds., *Phosphates: Geochemical, Geobiological, and Materials Importance*, Volume 48. Washington, DC., Mineralogical Society of America, pp. 292-335.

Spicer, E. M., Stevens, G., and Buick, I. S. (2004). The low-pressure partial-melting behaviour of natural boron-bearing metapelites from the Mt. Stafford area, central Australia. *Contributions to Mineralogy & Petrology*. Vol. 148, No. 2, pp. 160-179.

Stewart, A. J., and Chan, R. A. (1982). Napperby, Northern Territory: Bureau of Mineral Resources, Geology and Geophysics.

USGS. (2013a). U.S. Geological Survey Certificate of Analysis - Basalt, Columbia River, BCR-2.

USGS. (2013b). U.S. Geological Survey Certificate of Analysis - Basalt, Hawaiian Volcanic Observatory, BHVO-2

van Hinsberg, V. J., Henry, D. J., and Marschall, H. R. (2011). Tourmaline: an ideal indicator of its host environment. *The Canadian Mineralogist*. Vol. 49, No. 1, pp. 1-16.

Vernon, R. H. (2004). A practical guide to rock microstructure. Cambridge University Press, Cambridge, United Kingdom.

Vernon, R. H., and Clarke, G. L. (2008). Principles of Metamophic Petrology. Cambridge University Press, New York, NY.

Vernon, R. H., Clarke, G. L., and Collins, W. J. (1990). Local, mid-crustal granulite facies metamorphism and melting: an example in the Mount Stafford area, Central Australia. *in* Ashworth, J. R., and Brown, M., eds., High-temperature Metamorphism and Crustal Anatexis: London, UK, Unwin Hyman.

Wang, W., Clarke, G. L., and Daczko, N. R. (pending submission). Effects of whole rock composition on melt fertility at low-P conditions; metasedimentary migmatite at Mt Stafford, central Australia. *Journal of Metamorphic Geology*.

Wark, D. A., and Miller, C. F. (1993). Accessory mineral behavior during differentiation of a granite suite: monazite, xenotime and zircon in the Sweetwater Wash pluton, southeastern California, U.S.A. *Chemical Geology*. Vol. 110, No. 1–3, pp. 49-67.

White, R. W., Powell, R., and Clarke, G. L. (2003). Prograde Metamorphic Assemblage Evolution during Partial Melting of Metasedimentary Rocks at Low Pressures: Migmatites from Mt Stafford, Central Australia. *Journal of Petrology*. Vol. 44, No. 11, pp. 1937-1960.

Whitney, D. L., and Evans, B. W. (2010). Abbreviations for names of rock-forming minerals. *The American Mineralogist*. Vol. 95, No. 1, pp. 185-187.

Williams, I. S. (2001). Response of detrital zircon and monazite, and their U-Pb isotopic systems, to regional metamorphism and host-rock partial melting, Cooma Complex, southeastern Australia. *Australian Journal of Earth Sciences*. Vol. 48, pp. 557-580.

Winter, J. D. (2010). Principles of Igneous and Metamorphic Petrology. 2nd Ed. Prentice Hall, New Jersey, USA.

Xie, X., Yan, M., Wang, C., Li, L., and Shen, H. (1989). Geochemical Standard Reference Samples GSD 9–12, GSS 1–8 and GSR 1–6. *Geostandards Newsletter*. Vol. 13, No. 1, pp. 83-179.

Yavuz, F., Yavuz, V., and Sasmaz, A. (2006). WinClastour—a Visual Basic program for tourmaline formula calculation and classification. *Computers & Geosciences*. Vol. 32, No. 8, pp. 1156-1168.

Appendix 1: Fieldwork Scales

Scale Marker	cm
Aus. 10 cent piece	2.3
Metal / Blue Pencil	13.0
Penknife	7.0

Appendix 2: Mount Stafford Sample Sites - 2010 and 2011

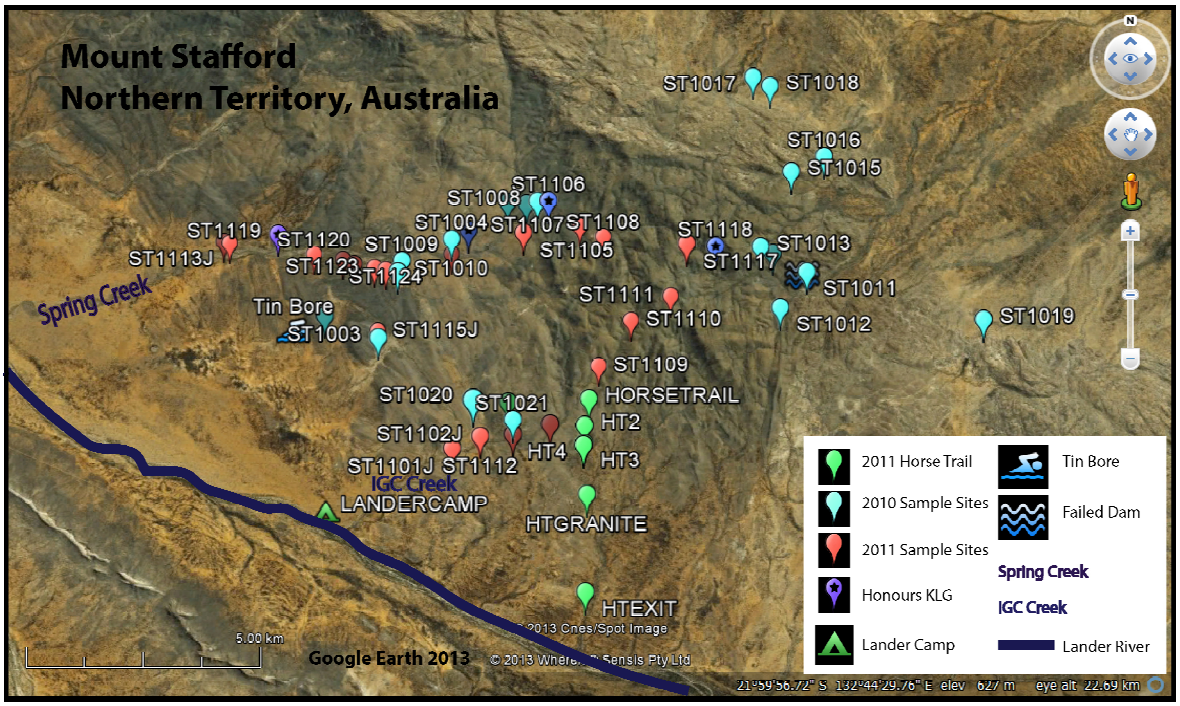

Mount Stafford, Northern Territory, Central Australia
Lander Camp 22° 3'40.13"S, 132°35'0.62"E
(Google Earth, 2013)

Appendix 3: Mount Stafford Transect and Granite Sample Numbers.

Mount Stafford Transect Samples

In order of increasing metamorphic grade (SW-NE)

Spring Creek Transect
ST1113
ST1114
ST1119
ST1120
ST1121
ST1122
ST1123
ST1124
ST1009
ST1010
ST1004, ST1116
ST1005
ST1105, ST1006
ST1007
ST1008
ST1106
ST1107
ST1108
ST1118
ST1117

IGC Creek Transect
ST1101
ST1102, ST1112, ST1020
ST1103, ST1021
ST1104
ST1109
ST1110
ST1111
ST1118, ST1012
ST1117, ST1013, ST1014

Granites
ST1015 to ST1019
HT Granite

Appendix 4: Field Sample and Analysis Log

Field Sample Log

Field Details				Analytical Techniques							
Year	Sample ID	GPS Coordinates	Field Notes	Thin Section	LOI	XRF Pellets	Trace Analysis	XRF Fused glass discs	Majors Analysis	EMP Analysis	SEM Analysis
2011	ST1119A	22° 0'29.07"S 132°34'20.95"E	And-Crd amphibolite Crd may be in the centre of dark sections. And on fresh surfaces is glassy and has a pink tinge.	9/08/2011	28/10/2011	14/09/2011	Macquarie 26/9/2011	20/10/2011	Wollongong 12/4/2012, China 4/11/2011	GEMOC 18/3/2013, 8/4/2013	GEMOC Mar, April, Oct, Nov 2012
	ST1119B			9/08/2011	28/10/2011	14/09/2011	Macquarie 26/9/2011	20/10/2011	Wollongong 12/4/2012, China 4/11/2011	GEMOC 18/3/2013, 8/4/2013	GEMOC Mar, April, Oct, Nov 2012
2010	ST1005A	22° 0'26.92"S 132°36'46.86"E	(Eileen) Folding of Crd indicates folding happened afer melting or late on in melting stage. Prismatic Sil in leuco, Sil psedomorphs And in 1cm crystals. Oxide is non-magnetic, prob. Ilm.	9/08/2011	28/10/2011	14/09/2011	Macquarie 26/9/2011	20/10/2011	Wollongong 12/4/2012, China 4/11/2011	GEMOC 18/3/2013, 8/4/2013	GEMOC Mar, April, Oct, Nov 2012
	ST1005B			9/08/2011	28/10/2011	14/09/2011	Macquarie 26/9/2011	20/10/2011	Wollongong 12/4/2012, China 4/11/2011	GEMOC 18/3/2013, 8/4/2013	GEMOC Mar, April, Oct, Nov 2012
2011	ST1106A	22° 0'6.43"S 132°37'48.21"E	Large 5mm square Kfs in the pelite layers. Estimate that may be 50% feldspar. Zone 3 - Both Mpe and Mps layers show signs of melting. Along Mps layers there are darker reaction zones.	9/08/2011						GEMOC 18/3/2013, 8/4/2013	GEMOC Mar, April, Oct, Nov 2012
	ST1106B				28/10/2011	14/09/2011	Macquarie 26/9/2011	20/10/2011	Wollongong 12/4/2012, China 4/11/2011		
	ST1106C				28/10/2011	14/09/2011	Macquarie 26/9/2011	20/10/2011	Wollongong 12/4/2012, China 4/11/2011		
	ST1106D			9/08/2011						GEMOC 18/3/2013, 8/4/2013	GEMOC Mar, April, Oct, Nov 2012
2011	ST1118A	22° 0'40.00"S 132°39'55.00"E	A - Mps with garnet. B - Mpe. Taken from RH stream, upstream from confluence.	9/08/2011	28/10/2011	14/09/2011	Macquarie 26/9/2011	20/10/2011	Wollongong 12/4/2012, China 4/11/2011	GEMOC 18/3/2013, 8/4/2013	GEMOC Mar, April, Oct, Nov 2012
	ST1118B			9/08/2011	28/10/2011	14/09/2011	Macquarie 26/9/2011	20/10/2011	Wollongong 12/4/2012, China 4/11/2011	GEMOC 18/3/2013, 8/4/2013	GEMOC Mar, April, Oct, Nov 2012

Appendix 5: Electron Microprobe (EMP) Maps

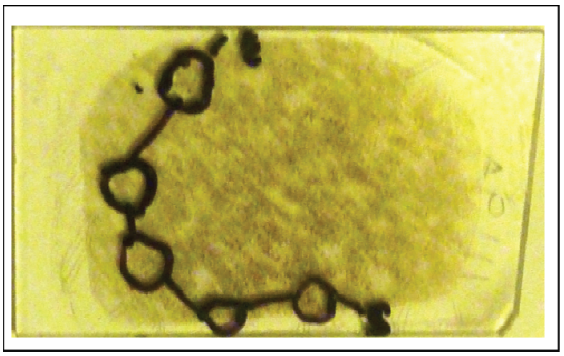

ST1119A

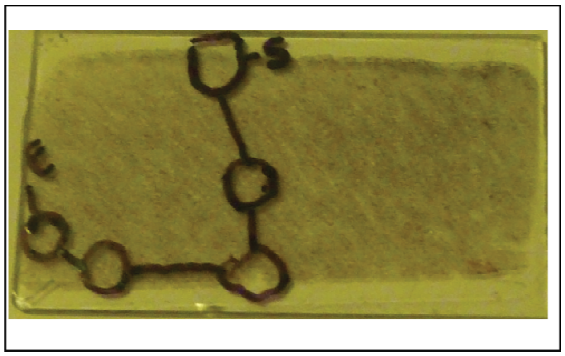

ST1119B

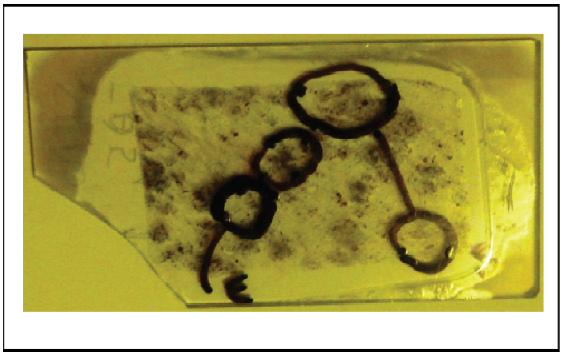

ST1005A

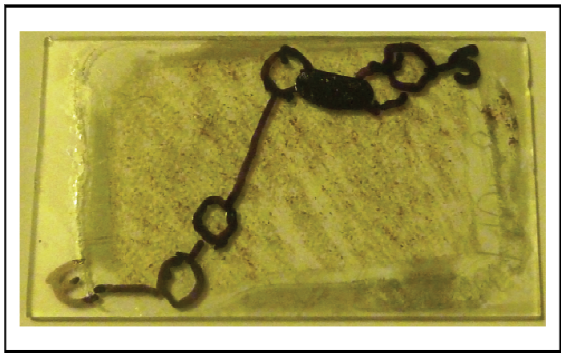

ST1005B

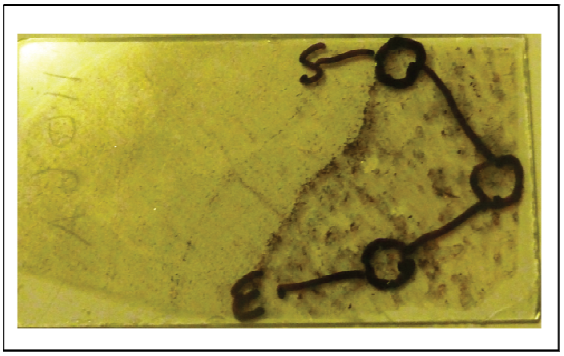

ST1106A

ST1106D

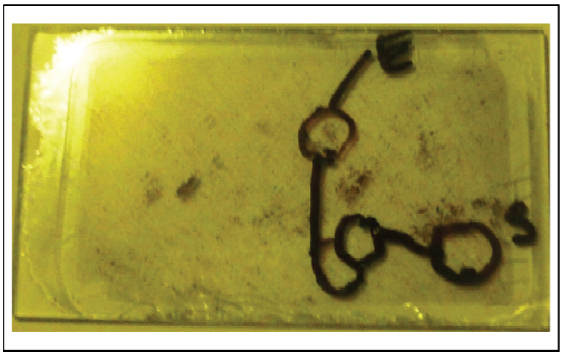

ST1118A

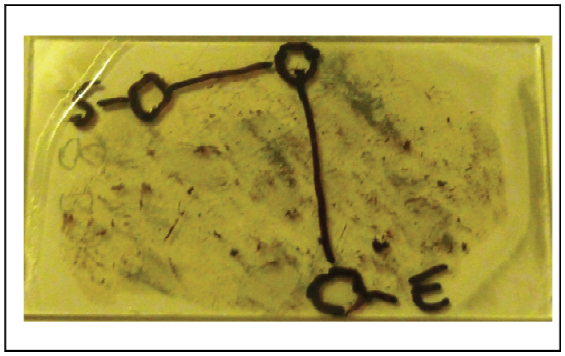

ST1118B

Appendix 6: Scanning Electron Microscope (SEM) Maps

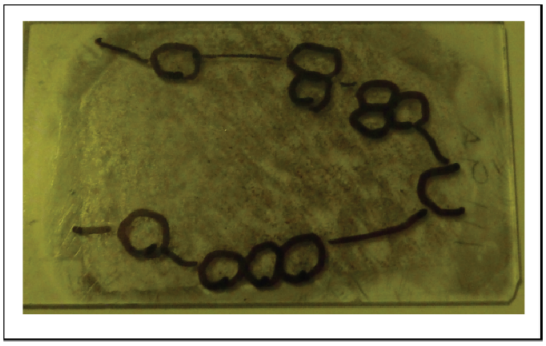

ST1119A

ST1119B

ST1005A

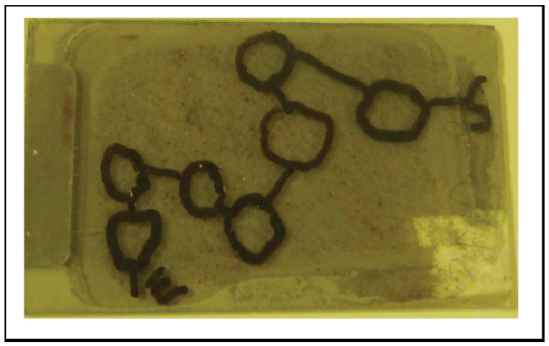

ST1005B

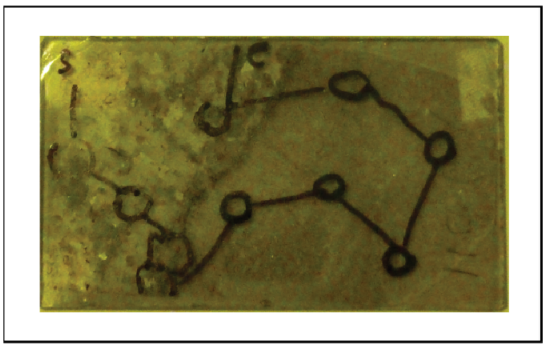

ST1106A

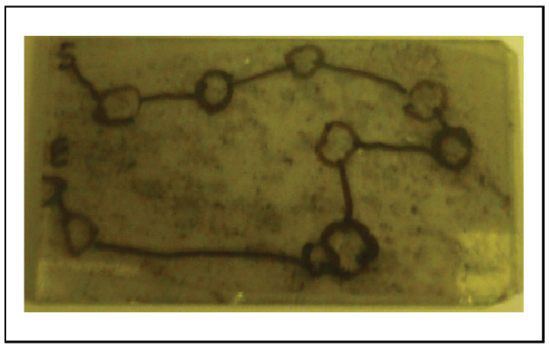

ST1106D

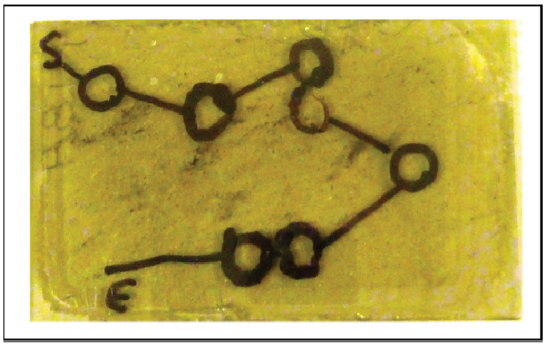

ST1118A

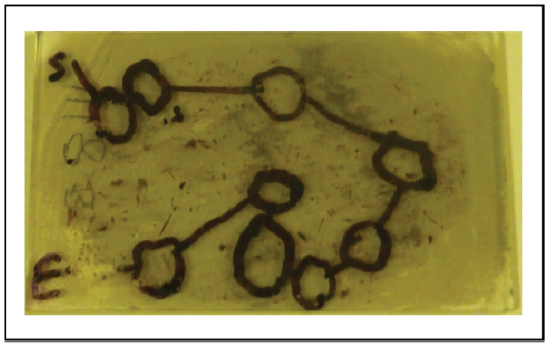

ST1118B

Appendix 7: XRF Whole Rock Lower Limit of Detection

XRF Major, Minor and Trace Element Lower Limit of Detection

Element	LLD wt% Oxide	Element	LLD ppm	Element	LLD ppm
SiO_2	0.01	V	1	Cd	0.2
TiO_2	0.01	Cr	0.3	In	0.3
Al_2O_3	0.03	Co	0.4	Sn	0.4
Fe_2O_3	0.01	Ni	0.3	Sb	0.5
MnO	0.01	Cu	0.3	Te	1
MgO	0.02	Zn	0.3	I	1
CaO	0.01	Ga	0.3	Cs	1.5
Na_2O	0.04	Ge	0.2	Ba	1.5
K_2O	0.01	As	0.3	La	2
P_2O_5	0.01	Se	0.2	Ce	3
		Br	0.3	Nd	5
		Rb	0.3	Hf	2
		Sr	0.2	Tl	0.7
		Y	0.2	Pb	0.2
		Zr	0.2	Bi	0.5
		Nb	0.2	Th	0.5
		Mo	0.2	U	0.5

Appendix 8: Measured and Reported Reference Standards for XRF Major and Minor Elements

Measured and Reported Reference Standards for XRF Analysis (Majors) Beijing University

	GRS1	Mean (*n*= 1)	StDev	**GSR3**	Mean (n=1)	StDev
SiO_2	72.83	72.86	0.03	44.64	44.52	0.12
TiO_2	0.29	0.29	0.00	2.36	2.37	0.01
Al_2O_3	13.40	13.37	0.03	13.83	13.86	0.03
$Fe_2O_{3\ tot}$	2.14	2.11	0.03	13.40	13.30	0.10
MnO	0.060	0.060	0.000	0.170	0.170	0.000
MgO	0.42	0.42	0.00	7.77	7.71	0.06
CaO	1.55	1.54	0.01	8.81	8.77	0.04
Na_2O	3.13	3.19	0.06	3.38	3.40	0.02
K_2O	5.01	4.99	0.02	2.32	2.31	0.01
P_2O_5	0.093	0.110	0.017	0.950	1.170	0.220
LOI	0.69	0.69	0.00	2.24	2.39	0.15
Total	99.61	99.63		99.87	99.97	

(Xie *et al.*, 1989)

Appendix 9: Mount Stafford XRF Whole Rock Major and Minor Element Analysis

Beijing - XRF Whole Rock Analysis (wt% Oxide)

Sample name	SiO_2 (%)	TiO_2 (%)	Al_2O_3 (%)	TFe_2O_3 (%)	MnO (%)	MgO (%)	CaO (%)	Na_2O (%)	K_2O (%)	P_2O_5 (%)	LOI (%)	TOTAL
ST1119A	67.68	0.54	17.36	5.34	0.040	1.74	0.24	0.77	5.14	0.120	0.70	99.67
ST1119B	74.21	0.46	13.16	4.51	0.030	1.39	0.48	1.07	3.65	0.110	0.70	99.77
ST1005A	56.76	0.50	24.33	5.93	0.070	1.95	0.70	1.95	6.48	0.150	0.64	99.46
ST1005B	68.22	0.60	17.20	5.80	0.040	1.70	0.36	0.96	4.57	0.160	0.58	100.19
ST1106B	66.39	0.61	18.13	6.51	0.050	1.88	0.20	0.95	4.14	0.100	1.28	100.24
ST1106C	58.25	0.65	23.50	7.65	0.060	2.47	0.38	1.19	5.19	0.120	0.68	100.14
ST1118A	76.63	0.54	11.94	4.71	0.070	1.51	0.81	0.88	2.33	0.090	0.44	99.95
ST1118B	59.44	0.69	21.79	5.41	0.070	1.85	0.78	1.73	7.02	0.120	0.52	99.41

Beijing - Whole Rock traces from XRF Fused Glass Discs (same session as above)

Sample name	FeO (wt%)Oxide	Ba (ppm)	Cr (ppm)	Ni (ppm)	Sr (ppm)	V (ppm)	Zr (ppm)
ST1119A	3.88	735.56	57.36	20.33	53.29	62.74	187.60
ST1119B	5.27	527.97	40.99	12.54	75.94	51.45	192.56
ST1005A	4.56	1164.27	77.84	29.61	165.34	74.59	93.00
ST1005B	4.33	684.51	62.18	21.59	78.91	66.06	183.42
ST1106B	3.00	797.59	67.85	21.16	84.61	68.63	184.16
ST1106C	5.94	1024.11	88.22	41.62	110.83	85.29	105.34
ST1118A	3.54	893.89	45.38	18.05	185.38	53.73	308.19
ST1118B	4.20	2515.28	65.66	23.13	352.32	83.09	147.49

Wollongong - XRF Whole Rock Analysis (wt% Oxide)

Sample name	SiO_2 (%)	TiO_2 (%)	Al_2O_3 (%)	Fe_2O_3 (%)	MnO (%)	MgO (%)	CaO (%)	Na_2O (%)	K_2O (%)	P_2O_5 (%)	SO_3 (%)	LOI (%)	TOTAL
ST1005A	57.80	0.48	26.48	5.90	0.062	2.29	0.68	0.86	6.42	0.214	0.09	1.00	102.30
ST1005B	69.11	0.60	19.23	5.53	0.038	1.81	0.35	< 0.02	4.55	0.244	0.09	0.80	102.35
ST1106B	66.73	0.59	19.41	6.08	0.043	1.64	0.20	< 0.02	4.05	0.191	0.10	1.51	100.55
ST1106C	58.66	0.64	24.74	7.32	0.054	2.36	0.42	< 0.02	5.00	0.207	0.09	0.90	100.38
ST1118A	77.09	0.53	12.71	4.41	0.059	0.96	0.82	2.05	2.31	0.209	0.09	0.68	101.92
ST1118B	60.57	0.67	23.18	5.42	0.065	1.65	0.81	1.08	6.86	0.218	0.09	0.73	101.34
ST1119A	66.77	0.52	17.89	5.13	0.031	1.20	0.25	< 0.02	5.05	0.226	0.07	1.12	98.25
ST1119B	74.33	0.45	13.99	4.29	0.030	0.86	0.50	< 0.02	3.68	0.216	0.08	0.95	99.36

Appendix 10: Measured and Reported Reference Standards for XRF Trace Elements

Measured and Reported Reference Standards for XRF Trace Chemical Analysis

Element	BCR-2 (USGS)	BCR-2 MacUni (n=1)	sd	BVHO-2 (USGS)	BHVO-2 MacUni (n=3)	sd
V	416	432.8	16.8	317	342.0	25.0
Cr	18	< 1.8	16.2	280	314.4	34.4
Mn	1520	1461	59	1290	1279	11
(wt%) Fe	9.66	9.251	0.409	8.63	8.554	0.076
Co	37	25.1	11.9	45	46.7	1.7
Ni		11.8		119	114.9	4.1
Cu	19	13.1	5.9	127	123.2	3.8
Zn	127	116.5	10.5	103	96.0	7.0
Ga	28	21.6	6.4	21.7	19.9	1.8
Ge	6.8	< LLD			< 0.3	
As		1			< LLD	
Se		< LLD			< 0.3	
Rb	48	46.8	1.2	9.8	8.7	1.1
Sr	346	339.3	6.7	389	387.1	1.9
Y	37	36.4	0.6	26	26.6	0.6
Zr	188	181.1	6.9	172	164.4	7.6
Nb		11.4			16.9	
Mo	248	194.4	53.6		3.4	
Ag		< 0.8			0.5	
Cd		0.6			0.7	
Sn		2.1			1.8	
Sb		< LLD			< LLD	
Te		< 0.2			0.4	
Cs	1.1	< LLD			< LLD	
Ba	683	663.8	19.2	130	125.3	4.7
La	25	18.4	6.6		11.7	
Ce	53	43.6	9.4	38	31.9	6.1
Pr	6.8	7.8	1		< 5.0	9.9
Nd	28	29.5	1.5	25	15.1	
Hf	4.8	< LLD		4.1	< LLD	
Ta		< 2.0			< 2.0	
Tl		< LLD			< LLD	
Pb	11	8.4	2.6		< 0.5	
Bi		< LLD			< LLD	
Th	6.2	8.1	1.9	1.2	1.6	0.4
U	1.69	< LLD			1.3	

(USGS, 2013a, b)

Appendix 11: Mount Stafford XRF Whole Rock Trace Element Analysis

XRF Trace Element (ppm) analysis data table

Element	ST1119A	ST1119B	ST1005A	ST1005B	ST1106B	ST1106C	ST1118A	ST1118B
V	67.4	46.9	89.1	83.1	79.4	94.1	60.5	91.3
Cr	86.2	62.4	98.8	95.5	86.6	108.7	66.8	107.9
(wt%) Mn	0.0277	0.02584	0.0546	0.03311	0.03854	0.04441	0.04747	0.05432
(wt%) Fe	3.654	3	4.139	3.9	4.396	5.125	3.008	3.748
Co	47.7	39.1	31	32.3	28.1	37.5	20.5	16.2
Ni	21.8	16	31.7	22.6	27.7	45.1	23.1	23.8
Cu	24.8	14.2	16	0.9	18.6	26.8	3.5	1.4
Zn	62.6	51.8	120	73.5	46.3	124.3	60.6	111.5
Ga	24.4	17.5	31.6	22.7	24.8	31	15.3	25.3
Ge	3.9	1	2.6	< 0.3	< 0.3	1.8	2.5	1.7
As	6.1	2.7	9.7	< 0.3	< 0.3	13.3	< 0.3	< 0.3
Se	0.6	< 0.2	< 0.2	< 0.2	< 0.2	0.2	< 0.2	< 0.2
Rb	265.8	205.4	314.6	222.7	173.2	224.9	84.4	275.9
Sr	51.8	73.8	162.8	78	81.2	108.6	187	347.9
Y	29.1	23.2	34.9	43.4	35.9	25.5	20.6	22.1
Zr	175.4	177.7	93.9	179.3	174.9	98.6	276.7	143.8
Nb	14.3	11.7	12.7	14.6	13.9	13.5	9.7	14
Mo	0.3	< 0.2	0.2	1	< 0.2	0.5	0.4	0.5
Ag	< 0.8	< 0.8	< 0.8	< 0.8	< 0.8	< 0.8	< 0.8	< 0.8
Cd	< 0.2	0.2	< 0.2	< 0.2	0.4	< 0.2	< 0.2	0.2
Sn	7	5.1	7.8	4.8	2.4	4.8	< 0.4	3
Sb	< 0.5	< 0.5	< 0.5	< 0.5	< 0.5	< 0.5	< 0.5	< 0.5
Te	< 0.2	0.2	< 0.2	< 0.2	< 0.2	< 0.2	< 0.2	< 0.2
Cs	11.4	10.4	16.5	8.2	6.2	11.5	3	9.8
Ba	739.2	510.9	1183	675.3	768	1047	862.4	2451
La	47.4	38.9	53.4	45.2	56.6	49.1	43.3	55.9
Ce	89.6	73	99.9	90.4	103.9	94.3	86.6	102.6
Pr	< 5.0	< 5.0	7.7	8.1	9.6	5.3	< 5.0	< 5.0
Nd	38.5	31.3	46.1	43.3	41.3	44.6	39.6	68.4
Hf	5.4	1.5	< 2.0	3.1	1.7	2.2	6.8	< 2.0
Ta	5.5	2.1	1.8	5.7	< 2.0	2.7	< 2.0	< 2.0
Tl	4.8	2.9	1.3	2.8	0.7	3.4	0.7	0.6
Pb	19.6	16.4	85.8	67.2	31.2	45.7	19.5	49.6
Bi	1.7	0.5	< 0.5	17.5	< 0.5	1.2	< 0.5	< 0.5
Th	21.3	17.6	18.7	20.6	23.7	17.7	18.5	23.2
U	2.6	1.8	4.4	50.7	2.1	4.4	1.2	6.3

Appendix 12: Electron Microprobe (EMP) Standards Analysis

CAMECA SX100 ELECTRON MICROPROBE
Large area LIF, PET and TAP
Lower limits of detection for 15 kV

Element	LLD (wt%)	% rsd
SiO_2	**0.03**	0.27
TiO_2	**0.02**	0.19
Al_2O_3	**0.01**	0.18
FeO	**0.03**	0.34
MnO	**0.03**	0.55
MgO	**0.03**	0.22
CaO	**0.02**	0.27
Na_2O	**0.02**	0.56
K_2O	**0.01**	0.49
Cr_2O_3	**0.04**	0.56
NiO	**0.03**	0.30
P_2O_5	**0.01**	0.65
Cl	**0.01**	0.82

Vienna cpx
Long Term Standards

	n=100	sd
SiO_2	49.88	0.35
TiO_2	1.49	0.03
Al_2O_3	7.60	0.04
FeO	8.29	0.09
MnO	0.14	0.02
MgO	12.30	0.10
CaO	17.48	0.09
Na_2O	2.68	0.04
Total	99.86	

Vienna cpx
Mount Stafford Analysis Sessions

	18/03/2013		8/04/2013	
	n=10	sd	n=10	sd
SiO_2	50.12	0.13	50.14	0.20
TiO_2	1.49	0.03	1.48	0.02
Al_2O_3	7.21	0.02	7.53	0.03
FeO	8.10	0.10	8.34	0.08
MnO	0.122	0.025	0.126	0.023
MgO	12.24	0.02	12.30	0.06
CaO	17.34	0.08	17.45	0.09
Na_2O	2.38	0.03	2.52	0.03
K_2O	0.014	0.009	0.012	0.007
Cr_2O_3	0.008	0.012	0.011	0.013
NiO	0.007	0.010	0.004	0.007
P_2O_5	0.019	0.016		
Total	99.04		99.91	

Vienna Standard Unknown Analysis - 18/3/2013

DataSet/ Point	K_2O	CaO	Na_2O	FeO	Al_2O_3	TiO_2	MgO	SiO_2	MnO	Cr_2O_3	NiO	P_2O_5	Total
1 / 1 .	0.0022	17.3585	2.3356	8.0072	7.1830	1.4492	12.2708	50.2358	0.1005	<LLD	<LLD	0.0442	98.9869
1 / 2 .	0.0131	17.4164	2.3894	8.0113	7.2008	1.5104	12.2567	49.9814	0.1741	0.0326	0.0265	0.0115	99.0240
1 / 3 .	0.0232	17.2896	2.4133	8.3093	7.1815	1.4970	12.2432	50.2195	0.1130	0.0085	<LLD	0.0336	99.3316
1 / 4 .	0.0196	17.3685	2.3701	8.0598	7.2134	1.5355	12.2116	49.9847	0.1244	0.0072	0.0012	0.0335	98.9296
1 / 5 .	0.0076	17.4134	2.3990	8.2058	7.2114	1.4457	12.2067	50.1561	0.1057	0.0000	<LLD	0.0246	99.1760
1 / 6 .	0.0040	17.3564	2.3404	8.0278	7.1973	1.4953	12.2212	50.1527	0.1306	0.0242	0.0161	0.0057	98.9717
1 / 7 .	0.0080	17.3498	2.3876	7.9924	7.2502	1.5325	12.2195	50.0087	0.1047	<LLD	0.0184	0.0303	98.9020
1 / 8 .	0.0265	17.1456	2.4138	8.1195	7.2224	1.4946	12.2504	50.1713	0.0839	<LLD	0.0012	0.0245	98.9537
1 / 9 .	0.0112	17.3807	2.3829	8.0545	7.1880	1.4700	12.2126	50.3430	0.1398	0.0012	0.0000	0.0286	99.2124
1 / 10 .	0.0272	17.2960	2.3612	8.1810	7.2427	1.4932	12.2693	49.9317	0.1448	0.0024	0.0081	0.0351	98.9927

Vienna Standard Unknown Analysis - 8/4/2013

DataSet/ Point	K_2O	CaO	Na_2O	FeO	Al_2O_3	TiO_2	MgO	SiO_2	MnO	Cr_2O_3	NiO	Total
1 / 1 .	0.0113	17.3226	2.4989	8.3967	7.5374	1.4528	12.3171	50.3177	0.1333	0.0170	0.0070	100.0118
1 / 2 .	0.0234	17.3959	2.5023	8.2929	7.5497	1.4769	12.2865	50.2419	0.1209	0.0243	<LLD	99.9146
1 / 3 .	0.0029	17.5616	2.4739	8.3219	7.5549	1.4822	12.2596	49.8162	0.0938	0.0146	<LLD	99.5818
1 / 4 .	0.0230	17.3767	2.5418	8.3134	7.4936	1.4582	12.3977	49.8057	0.1272	<LLD	0.0046	99.5419
1 / 5 .	0.0153	17.4276	2.5319	8.3774	7.5037	1.4776	12.3366	50.2819	0.1283	<LLD	<LLD	100.0802
1 / 6 .	0.0080	17.3885	2.5195	8.3216	7.5745	1.5048	12.3409	50.2805	0.1346	0.0134	<LLD	100.0862
1 / 7 .	0.0142	17.5008	2.5558	8.4733	7.5652	1.4768	12.2844	50.1383	0.0959	0.0377	0.0104	100.1529
1 / 8 .	0.0044	17.5372	2.5424	8.2449	7.4818	1.5211	12.2674	50.1471	0.1377	<LLD	<LLD	99.8839
1 / 9 .	0.0142	17.4257	2.5522	8.4672	7.4963	1.4881	12.2806	50.0093	0.1753	<LLD	<LLD	99.9089
1 / 10 .	0.0037	17.5909	2.4616	8.2271	7.5017	1.4938	12.1810	50.3802	0.1179	<LLD	0.0197	99.9775

Appendix 13 : Mount Stafford Tourmaline EMP Point Analysis

ST1119A - Thin Section Tourmaline EMP Mineral Chemistry (wt%)

DataSet/Point	43 / 1.	44 / 1.	45 / 1.	46 / 1.	47 / 1.	48 / 1.	49 / 1.	50 / 1.	51 / 1.	52 / 1.	53 / 1.
Comment	1119A C1 1	1119A C1 2	1119A C2 1	1119A C3 1	1119A C3 2	1119A C3 3	1119A C4 1	1119A C4 2	1119A C4 3	1119A C5 1	1119A C5 2
Comment 2	CORE	RIM	CORE	CORE	CORE	CORE	CORE	CORE	CORE	CORE	CORE
SiO_2	36.3606	35.7277	36.1908	34.7907	34.5817	33.7072	36.0857	35.4320	34.7010	35.1838	36.5037
TiO_2	0.6723	0.6666	0.8997	0.3550	0.9548	0.3682	1.1575	0.6208	1.0188	0.8510	1.1181
Al_2O_3	34.2176	34.0186	32.9464	34.7490	32.5870	35.3647	31.4456	34.0453	32.8657	33.3067	33.3406
Cr_2O_3	0.0000	0.0249	0.0000	0.0000	0.5819	0.0199	0.0669	0.0000	0.5848	0.0036	0.0120
Fe_2O											
FeO	9.2585	10.3558	9.1308	11.5989	8.7044	12.6213	8.9269	9.5493	8.5937	10.9142	7.6525
MnO	0.0497	0.0403	0.0642	0.0361	0.0041	0.0751	0.0487	0.0352	0.0041	0.0960	0.0364
MgO	3.9321	3.3374	4.4487	2.0833	4.7269	1.0194	5.5456	3.4862	4.8209	3.2775	5.2387
CaO	0.5908	0.6027	0.3821	0.4745	1.1759	0.3963	1.0836	0.4372	1.2354	0.6292	0.5985
Na_2O	1.6602	1.7413	1.9434	1.8883	1.5936	1.5128	1.6302	1.6495	1.5410	1.8314	1.7874
K_2O	0.0388	0.0369	0.0388	0.0578	0.0744	0.0360	0.0376	0.0396	0.0594	0.0394	0.0427
Total	86.7806	86.5521	86.0449	86.0335	84.9847	85.1209	86.0284	85.2950	85.4248	86.1329	86.3307
Normalised to 24.5 Oxygen											
Si	5.9334	5.8883	5.9660	5.8080	5.7999	5.7125	5.9687	5.8937	5.7850	5.8598	5.9509
Ti	0.0825	0.0827	0.1116	0.0446	0.1205	0.0469	0.1440	0.0777	0.1278	0.1066	0.1371
Al	6.5808	6.6078	6.4010	6.8369	6.4413	7.0637	6.1300	6.6742	6.4574	6.5378	6.4058
Cr	0.0000	0.0032	0.0000	0.0000	0.0772	0.0027	0.0087	0.0000	0.0771	0.0005	0.0015
Fe+3											
Fe+2	1.2635	1.4274	1.2588	1.6194	1.2209	1.7889	1.2348	1.3284	1.1981	1.5202	1.0433
Mn	0.0069	0.0056	0.0090	0.0051	0.0006	0.0108	0.0068	0.0050	0.0006	0.0135	0.0050
Mg	0.9566	0.8200	1.0933	0.5185	1.1818	0.2575	1.3674	0.8645	1.1981	0.8138	1.2731
Ca	0.1033	0.1064	0.0675	0.0849	0.2113	0.0720	0.1920	0.0779	0.2207	0.1123	0.1045
Na	0.5253	0.5564	0.6211	0.6112	0.5182	0.4971	0.5228	0.5320	0.4981	0.5914	0.5650
K	0.0081	0.0078	0.0082	0.0123	0.0159	0.0078	0.0079	0.0084	0.0126	0.0084	0.0089
H	0.0000	0.0000	0.0000	0.0000	0.0000	0.0000	0.0000	0.0000	0.0000	0.0000	0.0000
Total	15.4603	15.5056	15.5365	15.5408	15.5875	15.4598	15.5833	15.4617	15.5754	15.5643	15.4952

X Site	Ca	0.1033	0.1064	0.0675	0.0849	0.2113	0.0720	0.1920	0.0779	0.2207	0.1123	0.1045
	Na + K	0.5333	0.5642	0.6293	0.6235	0.5341	0.5049	0.5307	0.5404	0.5107	0.5998	0.5738
	Vacancy	0.3634	0.3294	0.3032	0.2916	0.2546	0.4232	0.2772	0.3817	0.2686	0.2880	0.3216

ST1119B - Thin Section Tourmaline EMP Mineral Chemistry (wt%)

DataSet/Point	30 / 1.	33 / 1.	34 / 1.	36 / 1.	37 / 1.	38 / 1.	39 / 1.	41 / 1.	42 / 1.
Comment	1119B c1 1	1119B c1 2	1119B c2 1	1119B c2 3	1119B c3 1	1119B c3 2	1119B c4 1	1119B c5 1	1119B c5 2
Comment 2	CORE	RIM	CORE	CORE	CORE	RIM	CORE	CORE	RIM
SiO_2	35.7787	35.9008	35.9676	34.6855	35.2287	35.5662	35.7320	35.4897	35.5858
TiO_2	0.8675	0.8915	0.5171	0.3330	0.6198	0.6039	0.3938	1.1133	1.0080
Al_2O_3	30.3577	29.9961	33.5142	32.6524	32.9008	32.6218	33.6879	32.5137	32.9007
Cr_2O_3	0.1197	0.1488	0.0724	0.0000	0.0047	0.0000	0.0035	0.0168	0.2178
Fe_2O									
FeO	6.1176	6.2198	9.8041	14.9678	13.5798	13.6492	12.2770	8.4169	8.3480
MnO	0.0135	0.0177	0.0372	0.0481	0.0615	0.0595	0.0308	0.0000	0.0374
MgO	8.3382	8.4578	3.6799	0.7594	1.7915	1.7633	2.0522	4.5462	4.8058
CaO	2.8175	2.8169	0.1822	0.0882	0.1142	0.0954	0.1254	0.9233	0.8419
Na_2O	1.2707	1.2641	1.8557	1.9643	2.0729	2.0287	1.6753	1.6486	1.4871
K_2O	0.0884	0.0802	0.0377	0.0280	0.0546	0.0299	0.0431	0.0569	0.0520
Total	85.7695	85.7936	85.6680	85.5266	86.4285	86.4178	86.0210	84.7253	85.2845
Normalised to 24.5 Oxygen									
Si	5.9014	5.9243	5.9629	5.9300	5.9195	5.9727	5.9653	5.9313	5.9043
Ti	0.1076	0.1107	0.0645	0.0428	0.0784	0.0763	0.0495	0.1400	0.1258
Al	5.9014	5.8338	6.5483	6.5793	6.5156	6.4564	6.6283	6.4043	6.4335
Cr	0.0156	0.0194	0.0095	0.0000	0.0006	0.0000	0.0005	0.0022	0.0286
Fe+3									
Fe+2	0.8439	0.8584	1.3593	2.1401	1.9083	1.9169	1.7141	1.1764	1.1584
Mn	0.0019	0.0025	0.0052	0.0070	0.0088	0.0085	0.0044	0.0000	0.0053
Mg	2.0503	2.0807	0.9095	0.1935	0.4488	0.4414	0.5107	1.1327	1.1887
Ca	0.4979	0.4981	0.0324	0.0162	0.0206	0.0172	0.0224	0.1653	0.1497
Na	0.4064	0.4044	0.5965	0.6511	0.6753	0.6605	0.5423	0.5342	0.4784
K	0.0186	0.0169	0.0080	0.0061	0.0117	0.0064	0.0092	0.0121	0.0110
H									
Total	15.7450	15.7491	15.4960	15.5661	15.5875	15.5563	15.4466	15.4986	15.4835

X Site	Ca	0.4979	0.4981	0.0324	0.0162	0.0206	0.0172	0.0224	0.1653	0.1497
	Na + K	0.4250	0.4213	0.6045	0.6572	0.6870	0.6669	0.5514	0.5463	0.4894
	Vacancy	0.0771	0.0806	0.3632	0.3266	0.2924	0.3159	0.4261	0.2883	0.3609

ST1005A Thin Section Tourmaline EMP Mineral Chemistry (wt%)

DataSet/Point	69 / 1.	70 / 1.	72 / 1.	73 / 1.	74 / 1.	75 / 1.	76 / 1.	77 / 1.	78 / 1.	79 / 1.	80 / 1.	81 / 1.
Comment	1005A C1 1	1005A C1 2	1005A C2 2	1005A C2 3	1005A C2 4	1005A C2 5	1005A C3 1	1005A C3 2	1005A C4 1	1005A C4 2	1005A C4 3	1005A C4 4
Comment 2	CORE	CORE	CORE	CORE	CORE	RIM	CORE	CORE	CORE	RIM	CORE	RIM
SiO_2	35.3349	35.1175	35.5000	35.6482	36.3851	35.4222	34.8522	35.1405	36.4920	35.3082	35.5537	36.6878
TiO_2	1.0767	1.1127	0.9793	1.0270	0.4459	0.8944	0.9491	0.8867	0.4568	1.2139	1.0700	0.4262
Al_2O_3	32.8187	32.8720	33.6527	33.0340	34.0234	33.5016	33.3955	33.7219	34.0463	32.9290	32.4520	33.5632
Cr_2O_3	0.1673	0.2864	0.0000	0.0322	0.0715	0.0525	0.0954	0.0203	0.0585	0.0724	0.0472	0.0167
Fe_2O												
FeO	8.9363	8.9478	9.5369	8.9984	9.1552	9.3169	9.2687	9.2419	8.9189	8.9289	9.8904	7.9973
MnO	0.0166	0.0000	0.0093	0.0124	0.0000	0.0073	0.0155	0.0083	0.0000	0.0124	0.0164	0.0000
MgO	4.6221	4.5277	3.7903	4.5263	3.8852	4.2597	4.2512	4.0946	3.7812	4.5847	4.3508	5.1556
CaO	1.0107	1.0172	0.7222	0.8609	0.4411	0.8345	0.9205	0.8186	0.4242	1.0999	0.9048	0.3448
Na_2O	1.7006	1.6703	1.6744	1.6976	1.4952	1.7439	1.7862	1.6940	1.5137	1.6955	1.7083	1.8012
K_2O	0.0448	0.0586	0.0384	0.0542	0.0539	0.0460	0.0523	0.0591	0.0431	0.0564	0.0392	0.0350
Total	85.7287	85.6101	85.9035	85.8913	85.9565	86.0789	85.5868	85.6858	85.7348	85.9012	86.0328	86.0278
Normalised to 24.5 Oxygen												
Si	5.8634	5.8394	5.8758	5.8946	5.9796	5.8543	5.8033	5.8309	6.0014	5.8484	5.9029	5.9970
Ti	0.1344	0.1392	0.1219	0.1278	0.0551	0.1112	0.1189	0.1107	0.0565	0.1513	0.1336	0.0524
Al	6.4183	6.4420	6.5647	6.4378	6.5899	6.5256	6.5537	6.5947	6.5990	6.4283	6.3501	6.4659
Cr	0.0219	0.0377	0.0000	0.0042	0.0093	0.0069	0.0126	0.0027	0.0076	0.0095	0.0062	0.0022
Fe+3												
Fe+2	1.2401	1.2443	1.3201	1.2444	1.2583	1.2878	1.2907	1.2825	1.2267	1.2369	1.3733	1.0933
Mn	0.0023	0.0000	0.0013	0.0017	0.0000	0.0010	0.0022	0.0012	0.0000	0.0017	0.0023	0.0000
Mg	1.1434	1.1224	0.9352	1.1158	0.9519	1.0495	1.0553	1.0129	0.9270	1.1321	1.0769	1.2563
Ca	0.1797	0.1812	0.1281	0.1525	0.0777	0.1478	0.1642	0.1455	0.0747	0.1952	0.1610	0.0604
Na	0.5471	0.5385	0.5373	0.5443	0.4764	0.5588	0.5767	0.5450	0.4827	0.5445	0.5499	0.5708
K	0.0095	0.0124	0.0081	0.0114	0.0113	0.0097	0.0111	0.0125	0.0090	0.0119	0.0083	0.0073
H												
Total	15.5603	15.5571	15.4926	15.5345	15.4095	15.5525	15.5886	15.5385	15.3847	15.5597	15.5644	15.5056

X Site	Ca	0.1797	0.1812	0.1281	0.1525	0.0777	0.1478	0.1642	0.1455	0.0747	0.1952	0.1610	0.0604
	Na + K	0.5566	0.5509	0.5454	0.5557	0.4877	0.5685	0.5878	0.5575	0.4917	0.5564	0.5582	0.5781
	Vacancy	0.2637	0.2678	0.3265	0.2918	0.4346	0.2837	0.2480	0.2970	0.4336	0.2484	0.2808	0.3615

ST1005B Thin Section Tourmaline EMP Mineral Chemistry (wt%)

DataSet/Point	62 / 1.	63 / 1.	64 / 1.	65 / 1.	68 / 1.
Comment	1005B C1 1	1005B C1 2	1005B C2 1	1005B C3 1	1005B C5 1
Comment 2	CORE	CORE	CORE	CORE	CORE
SiO_2	36.8326	36.7328	35.5282	35.6659	37.0796
TiO_2	0.1730	0.1791	0.1301	0.2620	0.0093
Al_2O_3	33.4316	33.9563	33.7814	33.5237	33.5908
Cr_2O_3	0.0202	0.2198	0.0107	0.0119	0.0060
Fe_2O					
FeO	9.3001	9.0709	8.6057	8.7861	8.0786
MnO	0.0320	0.0114	0.0000	0.0124	0.0031
MgO	4.1778	3.4451	4.7465	4.6564	5.0410
CaO	0.3539	0.2132	0.7704	0.9083	0.3989
Na_2O	1.6781	1.4588	1.7598	1.6733	1.8478
K_2O	0.0579	0.0328	0.0456	0.0610	0.0431
Total	86.0572	85.3202	85.3784	85.5610	86.0983
Normalised to 24.5 Oxygen					
Si	6.0512	6.0635	5.8886	5.9066	6.0529
Ti	0.0214	0.0222	0.0162	0.0326	0.0011
Al	6.4732	6.6061	6.5989	6.5432	6.4626
Cr	0.0026	0.0287	0.0014	0.0016	0.0008
Fe+3					
Fe+2	1.2778	1.2522	1.1929	1.2169	1.1029
Mn	0.0045	0.0016	0.0000	0.0017	0.0004
Mg	1.0232	0.8478	1.1728	1.1496	1.2268
Ca	0.0623	0.0377	0.1368	0.1612	0.0698
Na	0.5345	0.4669	0.5655	0.5373	0.5848
K	0.0121	0.0069	0.0096	0.0129	0.0090
H					
Total	15.4628	15.3337	15.5827	15.5635	15.5111

X Site	Ca	0.0623	0.0377	0.1368	0.1612	0.0698
	Na + K	0.5467	0.4738	0.5752	0.5502	0.5938
	Vacancy	0.3910	0.4885	0.2880	0.2887	0.3364

ST1106A - Thin Section Tourmaline EMP Mineral Chemistry (wt%)

DataSet/Point	1 / 1 .	2 / 1 .	3 / 1 .	4 / 1 .	5 / 1 .	6 / 1 .	8 / 1 .	10 / 1 .
Comment	1106A c1 1	1106A c1 1rim	1106A c2 1	1106A c2 2	1106A c3 1	1106A c3 2	1106A c3 4	1106A c3 6
Comment 2	CORE	RIM	RIM	CORE	CORE	CORE	CORE	CORE
SiO_2	35.8480	36.1798	35.5590	35.1919	34.4809	35.5438	35.2864	35.4059
TiO_2	0.1249	0.1546	0.1961	0.3547	0.2625	0.2911	0.7041	0.6088
Al_2O_3	33.6172	33.2163	39.9216	33.0349	33.7287	33.0390	33.7165	33.0103
Cr_2O_3	0.0000	0.0178	0.0251	0.0000	0.3707	0.4333	0.0296	0.0106
Fe_2O								
FeO	8.5706	8.4857	6.7848	9.3234	8.8949	8.7828	9.5000	9.3888
MnO	0.0227	0.0062	0.0000	0.0134	0.0134	0.0196	0.0268	0.0287
MgO	5.0250	5.2911	3.0709	4.8175	4.5558	4.7414	3.9651	4.5835
CaO	0.7385	0.7319	0.5260	1.0312	1.0328	0.7834	0.8607	0.9374
Na_2O	1.7588	1.8094	1.2435	1.6639	1.7441	1.7442	1.7001	1.6787
K_2O	0.0477	0.0431	0.0388	0.0588	0.0551	0.0570	0.0453	0.0511
Total	85.8071	85.9358	87.3658	85.4896	85.1390	85.4356	85.8345	85.7040
Normalised to 24.5 Oxygen								
Si	5.9136	5.9534	5.6548	5.8628	5.7665	5.9061	5.8512	5.8821
Ti	0.0155	0.0191	0.0235	0.0445	0.0330	0.0364	0.0878	0.0761
Al	6.5358	6.4418	7.4822	6.4862	6.6480	6.4702	6.5892	6.4634
Cr	0.0000	0.0023	0.0032	0.0000	0.0490	0.0569	0.0039	0.0014
Fe+3								
Fe+2	1.1824	1.1678	0.9023	1.2990	1.2441	1.2205	1.3174	1.3045
Mn	0.0032	0.0009	0.0000	0.0019	0.0019	0.0028	0.0038	0.0040
Mg	1.2358	1.2979	0.7280	1.1964	1.1358	1.1745	0.9802	1.1352
Ca	0.1305	0.1290	0.0896	0.1841	0.1851	0.1395	0.1529	0.1669
Na	0.5625	0.5773	0.3834	0.5374	0.5655	0.5619	0.5466	0.5407
K	0.0100	0.0090	0.0079	0.0125	0.0118	0.0121	0.0096	0.0108
H								
Total	15.5893	15.5986	15.2748	15.6247	15.6406	15.5809	15.5425	15.5852
X Site Ca	0.1305	0.1290	0.0896	0.1841	0.1851	0.1395	0.1529	0.1669
Na + K	0.5726	0.5863	0.3913	0.5499	0.5773	0.5740	0.5562	0.5516
Vacancy	0.2969	0.2846	0.5191	0.2660	0.2377	0.2865	0.2909	0.2816

ST1106D - Thin Section Tourmaline EMP Mineral Chemistry (wt%)

DataSet/Point	13 / 1 .	14 / 1 .	16 / 1 .	17 / 1 .	18 / 1 .	21 / 1 .	22 / 1 .	24 / 1 .	25 / 1 .	26 / 1 .	27 / 1 .	28 / 1 .	29 / 1 .
Comment	1106D c1 3	1106D c1 4	1106D c3 1	1106D c3 2	1106D c3 3	1106D c5 2	1106D c5 3	1106D c5 5	1106D c6 1	1106D c6 2	1106D c6 3	1106D c6 4	1106D c6 5
Comment 2	CORE	CORE	CORE	CORE	CORE	CORE	CORE	CORE	CORE	CORE	RIM	CORE	RIM
SiO_2	35.5489	34.9749	35.0808	35.3237	35.6759	35.2975	34.6099	35.1676	35.4636	35.1901	34.5608	34.4890	34.5624
TiO_2	0.5591	0.4848	1.0624	0.9335	0.4985	0.4783	0.6815	0.4721	0.1955	0.5512	0.4555	0.4243	0.5316
Al_2O_3	35.1206	34.6480	33.2820	33.2156	34.3601	34.3604	34.3200	33.1118	33.7110	33.4911	35.1454	35.5714	34.5138
Cr_2O_3	0.0024	0.0000	0.1583	0.2716	0.0774	0.0012	0.0321	0.0261	0.0012	0.0047	0.0000	0.0119	0.0298
Fe_2O													
FeO	8.7003	8.8621	8.5711	8.5446	8.5493	8.9743	9.2917	9.5769	9.7532	9.6826	9.4863	9.1597	9.1713
MnO	0.0093	0.0052	0.0072	0.0000	0.0300	0.0093	0.0000	0.0114	0.0072	0.0475	0.0000	0.0579	0.0238
MgO	3.7915	3.9511	4.7204	4.7434	4.3100	4.0620	3.8308	4.5006	4.1335	3.9703	3.3354	3.4672	3.4868
CaO	0.8019	0.8758	0.9093	0.8329	0.5511	0.9247	0.9500	0.9551	0.8524	0.8708	1.1114	0.9103	1.0964
Na_2O	1.6713	1.6634	1.7945	1.7778	1.8448	1.6429	1.6911	1.6717	1.6256	1.5897	1.5323	1.5520	1.5279
K_2O	0.0630	0.0570	0.0416	0.0473	0.0590	0.0571	0.0417	0.0526	0.0316	0.0409	0.0282	0.0233	0.0361
Total	86.2683	85.5223	85.6276	85.6904	85.9561	85.8077	85.4488	85.5458	85.7748	85.4390	85.6551	85.6670	84.9798
Normalised to 24.5 Oxygen													
Si	5.8263	5.7966	5.8176	5.8492	5.8680	5.8334	5.7636	5.8605	5.8845	5.8658	5.7391	5.7136	5.7784
Ti	0.0689	0.0604	0.1325	0.1163	0.0617	0.0595	0.0854	0.0592	0.0244	0.0691	0.0569	0.0529	0.0669
Al	6.7840	6.7678	6.5049	6.4822	6.6607	6.6925	6.7358	6.5032	6.5925	6.5795	6.8783	6.9452	6.8006
Cr	0.0003	0.0000	0.0208	0.0356	0.0101	0.0002	0.0042	0.0034	0.0002	0.0006	0.0000	0.0016	0.0039
Fe+3													
Fe+2	1.1925	1.2284	1.1887	1.1833	1.1760	1.2403	1.2941	1.3347	1.3534	1.3498	1.3174	1.2691	1.2823
Mn	0.0013	0.0007	0.0010	0.0000	0.0042	0.0013	0.0000	0.0016	0.0010	0.0067	0.0000	0.0081	0.0034
Mg	0.9264	0.9762	1.1670	1.1709	1.0568	1.0008	0.9510	1.1181	1.0225	0.9866	0.8257	0.8563	0.8690
Ca	0.1408	0.1555	0.1616	0.1478	0.0971	0.1637	0.1695	0.1705	0.1515	0.1555	0.1977	0.1616	0.1964
Na	0.5311	0.5345	0.5770	0.5708	0.5883	0.5264	0.5460	0.5401	0.5230	0.5138	0.4933	0.4985	0.4953
K	0.0132	0.0121	0.0088	0.0100	0.0124	0.0120	0.0089	0.0112	0.0067	0.0087	0.0060	0.0049	0.0077
H													
Total	15.4848	15.5323	15.5799	15.5660	15.5353	15.5301	15.5585	15.6026	15.5596	15.5362	15.5145	15.5118	15.5039
X Site Ca	0.1408	0.1555	0.1616	0.1478	0.0971	0.1637	0.1695	0.1705	0.1515	0.1555	0.1977	0.1616	0.1964
Na + K	0.5443	0.5466	0.5858	0.5808	0.6007	0.5385	0.5549	0.5513	0.5297	0.5225	0.4993	0.5034	0.5030
Vacancy	0.3149	0.2979	0.2526	0.2715	0.3022	0.2978	0.2756	0.2782	0.3188	0.3220	0.3029	0.3350	0.3006

(No Tourmaline data for ST1118A)

ST1118B Thin Section Tourmaline EMP Mineral Chemistry (wt%)

DataSet/Point	59 / 1.	60 / 1.	61 / 1.
Comment	1118B C1 1	1118B C2 1	1118B C3 1
Comment 2	CORE	CORE	CORE
SiO_2	36.1715	36.0809	37.4022
TiO_2	0.0361	0.3363	0.0141
Al_2O_3	32.0641	31.6698	32.4152
Cr_2O_3	0.0048	0.0047	0.0191
Fe_2O			
FeO	8.4925	9.0642	8.2952
MnO	0.0072	0.0216	0.0320
MgO	5.9022	5.4520	6.0230
CaO	1.1643	0.9920	0.9793
Na_2O	1.8324	1.9491	1.9954
K_2O	0.0555	0.0726	0.0413
Total	85.7305	85.6434	87.2169

Normalised to 24.5 Oxygen

Si	5.9857	5.9977	6.0643
Ti	0.0045	0.0421	0.0017
Al	6.2534	6.2045	6.1942
Cr	0.0006	0.0006	0.0024
Fe+3			
Fe+2	1.1753	1.2601	1.1248
Mn	0.0010	0.0030	0.0044
Mg	1.4560	1.3511	1.4558
Ca	0.2064	0.1767	0.1701
Na	0.5879	0.6282	0.6273
K	0.0117	0.0154	0.0085
H	0.0000	0.0000	0.0000
Total	15.6826	15.6794	15.6536

X Site	Ca	0.2064	0.1767	0.1701
	Na + K	0.5996	0.6436	0.6358
	Vacancy	0.1939	0.1797	0.1941

Appendix 14 : Mount Stafford Tourmaline EMP Transect Analysis

ST1119A C3 - Tourmaline EMP Mineral Chemistry (wt%)

Transect Point	5	6	7	9	8	10	4	3	2	1
DataSet/Point	1 / 1.	2 / 1.	3 / 1.	5 / 1.	6 / 1.	7 / 1.	10 / 1.	11 / 1.	12 / 1.	13 / 1.
Comment	ST1119A C3 1	ST1119A C3 2	ST1119A C3 3	ST1119A C3 5	ST1119A C3 4-repe	ST1119A C3 6	ST1119A C3 1.3	ST1119A C3 1	ST1119A C3 1.5	ST1119A C3 1.6
	core	core	core	rim	rim	rim	not used	not used	not used	rim
SiO_2	34.30	34.34	34.37	36.02	35.63	34.37	33.82	33.67	33.89	35.40
TiO_2	0.42	0.42	0.41	0.90	1.02	0.97	0.36	0.48	0.48	1.00
Al_2O_3	0.00	0.02	0.02	0.04	0.03	0.32	0.01	0.00	0.00	0.05
Cr_2O_3	0.05	0.06	0.04	0.02	0.02	0.07	0.07	0.06	0.05	0.03
Fe_2O										
FeO	35.39	35.29	35.41	33.52	32.16	34.12	35.80	35.53	35.15	33.44
MnO	0.0524	0.0327	0.0205	0.0577	0.0124	0.0124	0.0593	0.0460	0.0410	0.0258
MgO	2.22	2.22	2.33	5.15	5.36	4.80	2.08	2.15	2.19	5.21
CaO	1.96	1.89	1.69	1.59	1.68	1.60	1.92	1.89	1.90	1.61
Na_2O	12.07	12.10	11.73	8.81	9.81	8.84	11.97	12.10	12.15	8.44
K_2O	0.44	0.46	0.45	0.64	0.90	1.13	0.48	0.48	0.47	0.89
NiO	0.00	0.01	0.00	0.02	0.05	0.11	0.00	0.00	0.00	0.04
Total	86.91	86.84	86.48	86.77	86.67	86.35	86.57	86.41	86.33	86.15

ST1119A C2 - Tourmaline EMP Mineral Chemistry (wt%)

Transect Point	1	2	3	4	5	6
DataSet/Point	15 / 1.	16 / 1.	17 / 1.	19 / 1.	20 / 1.	21 / 1.
Comment	ST1119A C2 1	ST1119A C2 2	ST1119A C2 3	ST1119A C2 4	ST1119A C2 5	ST1119A C2 6
	rim	core	core	core	core	rim
SiO_2	34.55	35.77	35.61	36.02	35.65	35.21
TiO_2	1.11	0.78	0.87	0.89	0.85	0.93
Al_2O_3	0.44	0.00	0.01	0.00	0.02	0.02
Cr_2O_3	0.07	0.03	0.03	0.06	0.03	0.06
Fe_2O						
FeO	33.75	34.07	34.17	33.81	33.85	34.04
MnO	0.0000	0.0816	0.0330	0.0453	0.0795	0.0617
MgO	4.76	4.28	4.48	4.33	4.32	4.20
CaO	1.57	1.96	1.98	1.93	1.96	1.95
Na_2O	9.15	9.57	9.14	9.31	9.49	9.84
K_2O	1.35	0.31	0.43	0.39	0.38	0.48
NiO	0.06	0.02	0.02	0.00	0.00	0.03
Total	86.79	86.86	86.78	86.77	86.62	86.83

ST1119B C1 - Tourmaline EMP Mineral Chemistry (wt%)

Transect Point	1	2	3	4	5
DataSet/Point	23 / 1.	24 / 1.	25 / 1.	26 / 1.	27 / 1.
Comment	ST1119B C1 1	ST1119B C1 2	ST1119B C1 3	ST1119B C1 4	ST1119B C1 5
	rim	core	core	core	rim
SiO_2	36.41	36.01	35.90	35.63	35.61
TiO_2	1.05	0.92	0.89	0.95	1.13
Al_2O_3	0.05	0.15	0.08	0.05	0.07
Cr_2O_3	0.04	0.09	0.06	0.08	0.07
Fe_2O					
FeO	33.04	30.96	31.23	30.72	33.53
MnO	0.0342	0.0342	0.0477	0.0456	0.0082
MgO	5.13	8.43	8.39	8.40	4.74
CaO	1.60	1.32	1.31	1.26	1.68
Na_2O	8.69	6.41	6.32	6.29	8.71
K_2O	0.75	2.79	2.83	2.85	0.92
NiO	0.00	0.03	0.00	0.00	0.02
Total	86.77	87.14	87.08	86.29	86.50

ST1005A C1 - Tourmaline EMP Mineral Chemistry (wt%)

Transect Point	1	2	3	4	7	5	6	8
DataSet/Point	28 / 1.	29 / 1.	30 / 1.	31 / 1.	32 / 1.	33 / 1.	34 / 1.	35 / 1.
Comment	ST1005A C1 1	ST1005A C1 2	ST1005A C1 3	ST1005A C1 4	ST1005A C1 5	ST1005A C1 6	ST1005A C1 7	ST1005A C1 8
	core - c-axis	core - c-axis	core - c-axis	core - c-axis	core - c-axis	core - c-axis	core - c-axis	core - c-axis
SiO_2	35.21	34.97	34.83	36.35	35.62	35.56	35.85	35.79
TiO_2	1.12	1.15	1.15	0.45	1.01	1.07	1.00	1.03
Al_2O_3	0.18	0.36	0.34	0.30	0.12	0.12	0.04	0.02
Cr_2O_3	0.06	0.06	0.03	0.05	0.05	0.06	0.05	0.05
Fe_2O								
FeO	34.16	33.89	34.10	34.92	33.14	33.88	33.39	33.37
MnO	0.0124	0.0247	0.0000	0.0475	0.0000	0.0072	0.0247	0.0103
MgO	4.58	4.53	4.55	3.72	4.82	4.58	4.86	4.92
CaO	1.71	1.73	1.70	1.50	1.73	1.66	1.73	1.67
Na_2O	9.17	9.35	9.05	9.08	9.52	9.18	9.76	9.43
K_2O	1.01	1.06	1.12	0.40	1.14	1.04	1.17	1.18
NiO	0.07	0.05	0.02	0.06	0.00	0.00	0.02	0.02
Total	87.29	87.19	86.89	86.87	87.15	87.16	87.89	87.50

ST1005B C2 - Tourmaline EMP Mineral Chemistry (wt%)

Transect Point	1	2	4
DataSet/Point	36 / 1 .	37 / 1 .	39 / 1 .
Comment	ST1005B C2 1	ST1005B C2 2	ST1005B C2 4
SiO_2	35.62	35.66	35.75
TiO_2	0.26	0.14	0.14
Al_2O_3	0.02	0.00	0.00
Cr_2O_3	0.06	0.06	0.05
Fe_2O			
FeO	34.76	34.36	34.64
MnO	0.0000	0.0093	0.0010
MgO	4.68	4.75	4.81
CaO	1.73	1.78	1.75
Na_2O	8.85	9.06	9.01
K_2O	0.90	0.80	0.75
NiO	0.02	0.05	0.04
Total	86.90	86.67	86.93

ST1005B C1 - Tourmaline EMP Mineral Chemistry (wt%)

Transect Point	1	2	3
DataSet/Point	43 / 1 .	44 / 1 .	45 / 1 .
Comment	ST1005B C5 1	ST1005B C5 2	ST1005B C5 3
SiO_2	36.72	36.85	36.67
TiO_2	0.04	0.02	0.13
Al_2O_3	0.01	0.04	0.02
Cr_2O_3	0.05	0.05	0.04
Fe_2O			
FeO	34.26	34.46	34.54
MnO	0.0000	0.0000	0.0010
MgO	4.96	5.00	5.05
CaO	1.96	1.89	1.91
Na_2O	8.42	8.21	8.03
K_2O	0.30	0.38	0.45
NiO	0.06	0.00	0.02
Total	86.77	86.89	86.86

Appendix 15: Rejected EMP Data

18/3/2013

DataSet/Point		1 / 1 .	19 / 1 .	20 / 1 .	23 / 1 .	31/1	32/1	35 / 1 .	54 / 1 .
Comment		1106A c1 1	1106D c4 1	1106D c5 1	1106D c5 4	FAIL	FAIL	1119B c2 2	1118A C1 1
Comment 2		??TUR	"PIN"	"PIN"	??TUR			??	?TUR
SiO2		35.8480	37.1829	40.5244	41.7592			36.6200	40.1427
TiO2		0.1249	0.0000	0.0000	0.0000			0.4397	0.0067
Al2O3		33.6172	33.8236	33.8299	33.8217			32.2827	29.3662
Cr2O3		0.0000	0.0000	0.0036	0.0327			0.0440	0.0000
Fe2O									
FeO		8.5706	8.4667	6.6685	5.5592			9.3134	10.8483
MnO		0.0227	0.0135	0.1517	0.0938			0.0414	0.0636
MgO		5.0250	4.5301	2.6015	1.4609			4.5882	5.3022
CaO		0.7385	0.0874	0.9944	1.0208			0.4398	0.4908
Na2O		1.7588	1.5896	0.1273	0.1216			1.4263	0.0463
K2O		0.0477	0.0170	0.2782	0.6338			0.0241	1.1507
NiO		~~0.0382~~							
P2O5		~~0.0154~~							
Total		85.8071	85.7107	85.1795	84.5038			85.2197	87.4175

8/4/2013

DataSet/Point	4 / 1 .	8 / 1 .	9 / 1 .	14 / 1 .	18 / 1 .	22 / 1 .	38 / 1 .	40 / 1 .	41 / 1 .	42 / 1 .
Comment	ST1119A C3 4	ST1119A C3 1.1	ST1119A C3 1.2	ST1119A C3 6-1 r	ST1119A C2 3	ST1119A C2 1.1	ST1005B C2 3	ST1005B C2 5	ST1005B C2	ST1005B C2 7
Comment 2	remove	remove	remove	not used	not used	not used	Qtz	not Tur	not tur	not used
SiO_2	0.00	34.00	33.85	34.44	35.77	35.16	99.72	69.84	57.59	43.82
TiO_2	0.00	0.33	0.39	0.98	0.87	0.99	0.00	0.00	0.00	0.00
Al_2O_3	0.00	0.05	0.01	0.29	0.00	0.00	0.00	0.00	0.03	0.00
Cr_2O_3	0.00	0.05	0.07	0.06	0.05	0.06	0.02	13.07	0.02	0.09
Fe_2O										
FeO	0.00	35.73	35.85	34.10	33.67	34.28	0.40	16.14	16.26	34.04
MnO	0.00	0.02	0.08	0.02	0.05	0.09	0.02	0.00	0.36	0.13
MgO	0.00	2.04	2.09	4.79	4.31	3.71	0.04	0.03	6.63	3.50
CaO	0.00	1.90	1.97	1.64	1.90	2.02	0.01	0.91	0.02	0.06
Na_2O	0.00	11.94	12.04	8.71	9.40	10.42	0.29	0.51	14.23	5.15
K_2O	0.00	0.45	0.47	1.08	0.37	0.48	0.01	0.01	0.03	0.13
NiO	0.00	0.00	0.00	0.05	0.00	0.01	0.00	0.01	0.08	0.01
Total	0.00	86.51	86.81	86.14	86.38	87.20	100.52	100.53	95.27	86.92